



**Politecnico  
di Torino**

**Politecnico di Torino**

**Master's Degree in Electronic Engineering**

**October 2024**

**In-Memory Sensing: a Novel Biosensing  
Platform Combining Silicon Nanowires  
and Microfluidics**

**Supervisors**

**Prof. Danilo DEMARCHI**

**Prof. Sandro CARRARA**

**Dr. Junrui CHEN**

**Candidate**

**Silvia CAPOZZOLI**



## Abstract

This Master's Thesis presents the development of a biosensing platform that leverages the memristive properties of silicon nanowires for detecting Prostate-Specific Antigen (PSA), a critical biomarker for early-stage prostate cancer diagnosis. The platform integrates three key components: silicon nanowires with nickel silicide (NiSi) pads as the core biosensors, gold electrodes for electrical measurements, and a PDMS-based microfluidic platform, which guides the sample to the active sensing area, optimizing reagent usage, and ensuring the necessary humidity conditions for biological reactions.

The core of the biosensing device consists of two-terminal, vertically stacked Schottky barrier silicon nanowire structures, fabricated through electron beam lithography and Bosch etching processes. These nanowires are anchored between NiSi pads, and when a potential difference is applied, exhibit memory-like behavior characteristic of memristors, with electrical contact established through two Schottky barriers. This memristive behavior is essential to the platform's sensing capabilities, as it manifests in a hysteresis loop in the current-voltage (I-V) characteristics. Upon surface activation and functionalization of the nanowires for antigen-antibody interactions, antigen binding results in a measurable shift in the voltage gap of the I-V curve, allowing for label-free detection.

The microfluidic platform, fabricated from PDMS using the SU-8 molding technique, incorporates finely designed channels that control the delivery of reagents, such as antibodies, antigens, and washing solutions. This approach offers several advantages over traditional drop-casting methods, including precise reagent concentration within the active sensing area, minimized reagents waste, and optimal humidity control for biological reactions. Furthermore, it simplifies reagent transport and storage. Different bonding techniques were explored and tested to ensure stable, leak-free integrations between the microfluidic platform and silicon chip with nanowires and electrodes.

The metal electrodes, patterned using photolithography and the lift-off method, extend from the NiSi pads to enable reliable electrical measurements without damaging the sensitive biosensor surfaces and pads. Additionally, the electrodes are fundamental for integrating the microfluidic system; without them, the NiSi pads would be covered by the PDMS structure, making it impossible to access the nanowires for electrical measurements. Electrode characterization and performance testing confirmed reliable conductivity and stable integration in most cases,

without introducing significant series resistance that could mask the memristive behavior.

Design requirements and decisions are critically discussed, along with microfabrication processes carried out in the cleanroom facilities at the Center of MicroNanoTechnology (CMi) of École Polytechnique Fédérale de Lausanne (EPFL), which led to the successful realization of the entire device. Comprehensive experimental results demonstrated successful PSA detection in most cases, though challenges and potential areas for improvements are also critically analyzed. Finally, potential future developments are explored, particularly in enhancing multiplexing capabilities, which would broaden the platform's applications in biomedical diagnostics. For instance, the integration of rotary valves could lead to more advanced fluidic control mechanisms, optimizing the microfluidic system's efficiency and adaptability.



# Acknowledgements

*“To my parents and my grandparents, Lina, Palma, Alberto, and Rosario”*

Reaching the conclusion of this Thesis has been a journey filled with challenges, but also extraordinary encounters, collaborations, and invaluable support, for which I wish to express my deepest gratitude.

First and foremost, I would like to thank Prof. Danilo Demarchi from the Politecnico di Torino for his availability and for helping me secure the opportunity to carry out my Thesis at the research laboratory I aspired to join.

An equally special thank you goes to Prof. Sandro Carrara from the École Polytechnique Fédérale de Lausanne (EPFL), at the BCI LAB. During my thesis work, Prof. Carrara demonstrated exceptional dedication, guiding me with patience and offering invaluable methodological advice, applicable even beyond the scope of this thesis. His insights enriched my research and allowed me to face challenges with greater confidence and preparation.

I would particularly like to thank Dr. Junrui Chen, with whom I had the opportunity to collaborate closely during the experimental activities in both the cleanroom and the laboratory. Thank you for sharing your knowledge and expertise with me,

for assisting me during technical training, and for guiding the production of the biosensors, a fundamental part of this work.

A sincere thank you also goes to the Centre of MicroNanoTechnology (CMi) at EPFL and all the center's staff for their continuous technical support and the numerous training sessions I received throughout the various phases of my research. Without their assistance and availability, the technical challenges faced in the laboratory would not have been solved so effectively.

A special thought goes to my parents, for their unconditional love and for always supporting me throughout every stage of my life. Thank you for always believing in me, giving me the space to explore, and for providing me with the confidence that allowed me to face all challenges with such determination.

A particularly heartfelt thank you goes to my grandparents, Lina, Palma, Alberto, and Rosario, whose love, wisdom, and unwavering support have always been a guiding light in my life. Even though some of you cannot be physically present anymore, you always knew that this milestone would be reached. From afar, I have shared every success with you, and I am deeply grateful for all the moments spent together. You have been, and always will be, my greatest fortune.

I would also like to extend my thanks to my friends, whose presence, affection, and moments of lightheartedness were an indispensable support. A special thank you to those who shared the months in Lausanne with me, making them unforgettable. Without you, this experience would not have had the same significance.

I conclude these acknowledgements with the awareness that every contribution, every piece of advice, and every moment shared during this journey has left a lasting impact, representing a crucial step toward future goals, challenges, and successes. For this, I will always be grateful.



# Table of Contents

<b>List of Tables</b>	VIII
<b>List of Figures</b>	IX
<b>1 Introduction</b>	1
1.1 Project Overview: Objective and Motivation . . . . .	1
<b>2 Memristors as Biosensors</b>	4
2.1 Introduction to Memristors . . . . .	4
2.2 Silicon Nanowires in Biosensing Applications . . . . .	7
2.2.1 Modeling of Silicon Nanowire . . . . .	11
<b>3 Microfluidic Systems for Biosensing</b>	14
3.1 Fundamentals of Microfluidics . . . . .	14
3.1.1 The Correlation Between Microfluidics and Electronics . . . . .	16
3.2 Microfluidic Applications: State of the Art . . . . .	18
3.3 Overview of the Final Device Design . . . . .	19
<b>4 Fundamentals of Microfabrication</b>	21

4.1	Introduction to Microfabrication . . . . .	21
4.1.1	Cleanroom Environment and Protocols . . . . .	22
4.2	Photolithography . . . . .	24
<b>5</b>	<b>Silicon Nanowires</b>	<b>29</b>
5.1	Methods and Processes in Silicon Nanowire Fabrication . . . . .	29
<b>6</b>	<b>Electrode Design and Fabrication for Memristor Integration</b>	<b>37</b>
6.1	Electrode Integration: Requirements and Motivation . . . . .	37
6.2	Electrode Layout and Design Specifications . . . . .	38
6.2.1	Computation of Electrical Resistance . . . . .	39
6.3	Electrode Fabrication Process: Lift-Off Method . . . . .	42
6.3.1	Mask Fabrication . . . . .	43
6.3.2	Photolithographic Process for Electrode Patterning . . . . .	44
6.3.3	Metal Selection and Deposition Process . . . . .	47
6.3.4	Final Fabricated Chip with Integrated Electrodes . . . . .	48
6.4	Electrode Characterization and Measurements . . . . .	50
6.4.1	Measurement Setup and Instrumentation . . . . .	50
6.4.2	Electrode Performance Characteristics . . . . .	51
<b>7</b>	<b>Microfluidic Platform Development</b>	<b>54</b>
7.1	Design and Requirements of the Microfluidic Platform . . . . .	54
7.2	Methods for Microfluidic Fabrication . . . . .	57
7.2.1	SU-8-Based Channel Fabrication . . . . .	57
7.2.2	SU-8 Molding for PDMS . . . . .	59

7.2.3	Reactivity Testing of SU-8 with Aminolabeled DNA . . . . .	62
7.2.4	Piranha Solution Reactivity Testing . . . . .	65
7.2.5	Final Fabrication Method Selection . . . . .	66
7.3	Detailed PDMS Fabrication Process with SU-8 Moulding . . . . .	67
<b>8</b>	<b>Bonding Techniques for Microfluidic Integration</b>	<b>75</b>
8.1	Oxygen Plasma . . . . .	75
8.1.1	Oxygen Plasma Bonding for PDMS . . . . .	76
8.1.2	Integration with Metallic Electrodes . . . . .	76
8.1.3	Plasma Activation Equipment . . . . .	78
8.1.4	Leakage Test Results . . . . .	79
8.2	Silanization Bonding with GPTMS/APTMS . . . . .	79
8.2.1	Leakage Test . . . . .	82
<b>9</b>	<b>Detection of Prostate Specific Antigen (PSA)</b>	<b>84</b>
9.1	Protocollo di rilevamento del PSA . . . . .	84
9.2	Analysis of Experimental Data . . . . .	87
<b>10</b>	<b>Conclusions and Future Perspectives</b>	<b>96</b>
	<b>Bibliography</b>	<b>99</b>

# List of Tables

7.1	Comparison of different fabrication methods for the microfluidic platform . . . . .	67
7.2	spin-coating recipe - Kayaku 3025 for 20 $\mu\text{m}$ . . . . .	70
7.3	spin-coating recipe - Kayaku 3050 for 40 $\mu\text{m}$ . . . . .	70
7.4	spin-coating recipe - Kayaku 3050 for 80 $\mu\text{m}$ . . . . .	71
7.5	soft-bake time - SU-8 (Kayaku) . . . . .	71

# List of Figures

2.1	Example of I-V characteristic of memristor (current is measured in ampere and voltage is measured in volt)[8] . . . . .	6
2.2	I-V characteristic of memristive biosensor considering 3.3fM (a) and 330 fM (b) concentration of PSA [21] . . . . .	10
2.3	General framework for illustrating the measurement process for silicon nanowire biosensors [22] . . . . .	11
2.4	Structures of SiNW (back-to-back Schottky diodes) [23] . . . . .	11
2.5	Electrical characteristic of a single-diode and band diagram for a p-type Schottky junction at equilibrium and in case of reverse bias [23] . . . . .	12
2.6	First equivalent circuit of memristive biosensors [24] . . . . .	13
2.7	Second equivalent circuit of memristive biosensors [24] . . . . .	13
3.1	Hydrodynamic Flow [27] . . . . .	15
3.2	Electrokinetic Flow [27] . . . . .	15
4.1	Cleanroom top view and classification at CMi, EPFL . . . . .	23
4.2	Main steps in a photolithographic process [46] . . . . .	25
4.3	Exposure methods in photolithography [47] . . . . .	27
4.4	Comparison of positive and negative photoresists [48] . . . . .	27

5.1	Spin-coating on SOI wafer . . . . .	30
5.2	Cross-section of fabricated structure after e-beam lithography and etching process . . . . .	30
5.3	Second stage of e-beam lithography for silicon nanowires fabrication	31
5.4	E-beam evaporation of 50 nm of nickel . . . . .	31
5.5	Final result after lift-off . . . . .	31
5.6	Nichel silicide formation after annealing step . . . . .	32
5.7	Third step of e-beam lithography for silicon nanowires fabrication .	32
5.8	Final result after the Bosh process . . . . .	33
5.9	Resist stripping . . . . .	33
5.10	Fourth step of photolithography for silicon nanowires fabrication . .	34
5.11	Isolator evaporation . . . . .	34
5.12	Final result after lift-off . . . . .	34
5.13	Fifth step of photolithography . . . . .	35
5.14	Final process flow step for the fabrication of silicon nanowires . . .	35
5.15	SEM image of silicon nanowires and NiSi pads . . . . .	36
6.1	Design of electrodes (KLayout) . . . . .	39
6.2	Process flow for electrodes fabrication (lift-off) . . . . .	43
6.3	AZnLOF spin curve [51] . . . . .	45
6.4	Representation of the device after photolithography . . . . .	45
6.5	Graphical representation of the device after metal deposition . . . .	47
6.6	Graphical representation of the device after lift-off . . . . .	48
6.7	Chips with silicon nanowires and integrated electrodes . . . . .	49

6.8	SEM image of NiSi pad and gold electrode . . . . .	49
6.9	Silicon-nanowires and NiSi pads with good electrode connection . . .	52
6.10	Good I-V characteristic of bare silicon-nanowire (integration of electrodes) . . . . .	52
6.11	Effect of parasitic capacitance on I-V characteristic (integration of electrodes) . . . . .	53
7.1	The chemical structure of PDMS [56] . . . . .	60
7.2	SU-moulding technique for PDMS [48] . . . . .	61
7.3	Fluorescence microscope analysis of the DNA sample on SU8 treated with 5% aminoethanol. . . . .	63
7.4	Fluorescence microscope analysis of the DNA sample on SU8 treated with 100% aminoethanol. . . . .	64
7.5	Fluorescence microscope analysis of the DNA sample on untreated SU-8. . . . .	65
7.6	Effect of piranha solution on SU-8 . . . . .	66
7.7	Process flow for SU-8 moulding and PDMS . . . . .	69
7.8	.GDS file for <i>MLA150</i> exposure (SU-8 mould) . . . . .	72
7.9	SU-8 mould details . . . . .	73
8.1	O <sub>2</sub> plasma treatment for PDMS-glass bonding [64] . . . . .	77
8.2	Leakage test for PDMS integrated with gold electrodes [65] . . . . .	78
8.3	Final biosensing device (silicon nanowire chip, NiSi pads, gold electrodes, microfluidic platform). There is no leakage, as all components are perfectly integrated. . . . .	80
8.4	PDMS-glass bonding . . . . .	81
8.5	Leakage test . . . . .	82

9.1	Voltage gap after antibody incubation and after antigen incubation for six nanowires in the first device (mean value and standard deviation)	88
9.2	Repeated measurements of the voltage gap for six nanowires in the first device . . . . .	89
9.3	Voltage gap after antibody incubation and after antigen incubation for three nanowires in the second device (mean value and standard deviation) . . . . .	90
9.5	I-V characteristic of NW1 (first device) before and after antigen incubation . . . . .	90
9.4	Repeated measurements of the voltage gap for three nanowires in the second device . . . . .	91
9.6	I-V characteristic of NW2 (first device) before and after antigen incubation . . . . .	91
9.7	I-V characteristic of NW3 (first device) before and after antigen incubation . . . . .	92
9.8	I-V characteristic of NW4 (first device) before and after antigen incubation . . . . .	92
9.9	I-V characteristic of NW5 (first device) before and after antigen incubation . . . . .	93
9.10	I-V characteristic of NW6 (first device) before and after antigen incubation . . . . .	93
9.11	I-V characteristic of NW1 (second device) before and after antigen incubation . . . . .	94
9.12	I-V characteristic of NW2 (second device) before and after antigen incubation . . . . .	94
9.13	I-V characteristic of NW3 (second device) before and after antigen incubation . . . . .	95



# Chapter 1

## Introduction

### 1.1 Project Overview: Objective and Motivation

The project developed in this Thesis is part of two ambitious projects carried out at the Bio-CMOS Interface Laboratory (BCI Lab) of the École Polytechnique Fédérale de Lausanne (EPFL), namely *In-Memory Sensing* and *Onco-PoK*. Both projects aim to go beyond traditional technologies in the fields of computing and biomedicine by leveraging the potential of the fourth fundamental component of electronics: the memristor.

*In-Memory Sensing*, a project funded by the Swiss National Science Foundation (SNSF), aims to overcome the bottleneck of the traditional Von Neumann computer architecture, which has enabled the diffusion of computing power on a global scale but presents structural limitations [1]. The Von Neumann architecture establishes a clear physical separation between the data processing unit (Central Processing Unit, CPU) and the memory unit. The continuous flow of data exchanged between the two units via the BUS, coupled with the inherent slowness of memory compared to the CPU, creates a bottleneck that limits both energy efficiency and computing speed.

In this scenario, memristors are an optimal solution as they allow both the memory and computing functions to be combined in a single device. Memristors can perform computational operations directly in memory, eliminating the need to move data between separate units. Their ability to simulate the behaviour of biological neurons makes them ideal for applications inspired by neural networks and artificial intelligence, where data can be processed in a more dynamic and integrated way.

At the same time, it is shown that memristors can also function as biosensors, hence the project's desire to create an architecture that implements the concept of *in-memory sensing*, i.e. allowing data processing and storage to be integrated directly into the sensors themselves, overcoming the concept of *edge computing*, which involves processing close to the data source [2].

In parallel, the *Onco-PoK* project, supported by Innosuisse and developed in collaboration with the CHUV Hospital (Centre Hospitalier Universitaire Vaudois) in Lausanne, focuses on the development of an innovative point-of-care nanobiosensor for measuring the concentration of anti-cancer molecules in the blood. Specifically, the device uses microelectromechanical systems (MEMS) and nanotechnology for therapeutic drug monitoring (TDM), such as monitoring the levels of imatinib in a patient's body, a targeted therapy drug used in certain cancer treatment [3]. Similarly, the memristive behaviour of silicon nanowires is chosen as the key element of the biosensing platform, with the goal of succeeding in detecting increasingly lower concentration of the target molecule.

Furthermore, developing an intuitive interface will enable clear visualisation of the results, allowing faster and more informed clinical decisions, maximising therapeutic efficacy and minimising side effects [3][4].

In this context, the Thesis focuses on the study of nanowires and their memristive behaviour, as well as their potential as biosensors, as required by both projects. To this end, an innovative biosensor platform has been developed, consisting of a chip with silicon nanowires as biosensors and integrated metal electrodes, which are essential to facilitate the measurement process and to create an efficient interface between the device and the biological sample. In addition, the integration of a microfluidic platform on the same chip was investigated to control the flow of samples over the active sensing area, ensuring uniform distribution and improving the sensing conditions, thereby enhancing the device efficiency. The microfluidics plays a key role in making the system adaptable to point-of-care applications, where the amount of sample available is often limited and the accuracy in the handling of very small volumes is essential in order to optimise the responsiveness and specificity of the sensor. Moreover, it helps ensure optimal conditions for specific biochemical reactions to occur, as will be discussed in more detail in the next chapters.

The integration of nanowires with memristive behaviour, metal electrodes and a microfluidic platform is a technological solution that combines sophisticated sensing capabilities with data visualisation and processing directly on the device. It is a concrete realisation of the concept of *in-memory sensing* and a solution that can also be applied to the research underlying the Onco-PoK project.

The work involved not only the design of the device and the study of its essential

physical characteristics, but also the development of the complete manufacturing process, carried out in the cleanroom with the fundamental support of the Centre of MicroNanoTechnology (CMi) in Lausanne.

In this Thesis, the physics of nanowires as biosensors and their memristive behaviour are studied, and their integration with electrodes and a microfluidic component is described in detail. The design choices made and the associated challenges faced and solutions proposed are critically discussed, along with all the microfabrication processes developed in the cleanroom. The Thesis goes on to describe how the nanowires can be functionalized for the accurate detection of target molecules, and the experimental procedures used to evaluate the sensor performance are illustrated. Finally, it outlines possible future developments aimed at improving the performance of the device and integrating new functionalities.

## Chapter 2

# Memristors as Biosensors

### 2.1 Introduction to Memristors

The memristor is known to be the fourth fundamental element in electronics, after the resistor, capacitor, and inductor.

Each of the elements, resistor, capacitor, and inductor, is defined in terms of relationships between two of the four fundamental quantities in circuit theory: electric current  $I$ , voltage  $V$ , electric charge  $q$ , and magnetic flux linkage  $\varphi$ . However, among the six possible combinations of these variables, only five had been fully defined until 1971. In that year, Professor Leon Chua postulated the existence of a fourth circuit element, the memristor, which completed the symmetry of circuit theory by defining a direct relationship between the magnetic flux linkage  $\varphi$  and the electric charge  $q$  [5].

Chua proposed that the memristor, a fusion of the terms *memory* and *resistor*, was a device that stored the history of the electric current passing through it in the form of variable resistance. This behavior was not reproduced by the resistor, capacitor, or inductor. However, for 37 years, the memristor remained a theoretical concept until, in 2008, Stanley Williams' team at HP Labs successfully realized a physical memristor based on solid-state materials [6].

The memristor is a passive device that provides a functional relationship between the magnetic flux linkage  $\varphi$  and the electric charge  $q$ . Formally, a memristor is defined as a two-terminal device where the magnetic flux linkage between its terminals is a function of the amount of charge that has passed through the device. There are two main types of memristors:

- Charge-controlled memristor: in this case, the relationship between the magnetic flux linkage  $\varphi$  and the charge  $q$  is expressed as a function of charge.
- Flux-controlled memristor: in this case, the relationship between the magnetic flux linkage  $\varphi$  and the charge  $q$  is expressed as a function of the magnetic flux linkage.

For charge-controlled memristors,

$$\varphi = f(q)$$

By differentiating this equation with respect to time, and considering that  $V(t) = \frac{d\varphi}{dt}$  and  $I(t) = \frac{dq}{dt}$ , the following relationship is obtained:

$$V(t) = M(q(t)) \cdot I(t) \tag{2.1}$$

where  $M(q(t))$  is the memristance, a quantity that varies over time depending on the amount of charge accumulated in the device. Memristance has the same unit of measurement as resistance (ohm), but its variability makes it a unique and fundamental concept in memristor theory [5].

For flux-controlled memristors, the relationship is expressed as:

$$q = f(\varphi)$$

By differentiating this equation with respect to time, we obtain:

$$I(t) = W(\varphi(t)) \cdot V(t) \tag{2.2}$$

where  $W(\varphi(t))$  is the memductance, a concept similar to conductance, which varies depending on the magnetic flux linkage. Again, the past history of flux and current through the device determines the current behavior of the memristor, justifying the term *memory* in the device's name [7].

From the above explanation, it is evident that the fundamental characteristic of the memristor is its ability to "remember" its resistive state even in the absence of power. This property is due to the fact that the memristor's resistance is not only a function of instantaneous current and voltage, but also depends on the history of

the charges that have passed through the device. This behavior is described by the I-V curve with hysteresis: as the current and voltage cyclically pass through zero, the area enclosed by the hysteresis loop represents the energy dissipated by the device (Fig. 2.1). At low excitation frequencies, the hysteresis is more pronounced because the device has time to accumulate charge and vary its resistance. When the voltage frequency increases, the device does not have enough time to respond to the current variation, and the hysteresis reduces until it disappears, leading the memristor's behavior to a linear resistance.

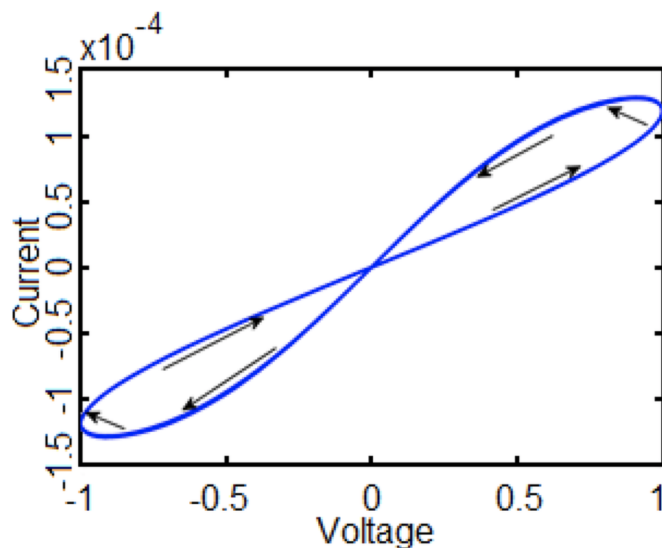


**Figure 2.1:** Example of I-V characteristic of memristor (current is measured in ampere and voltage is measured in volt)[8]

The discovery of the memristor by Leon Chua in 1971 was not entirely unexpected. In fact, as early as the 1960s, the concept of a resistor with memory had been discussed in the context of some primitive devices, such as the memristor developed by Bernard Widrow in 1960 [9]. The memristor, although having three terminals instead of two, was a pioneering idea where the device's resistance was controlled by the time integral of the current on a third terminal.

Later, in 1976, Leon Chua and S.M. Kang published a paper that further expanded the theory of memristive devices, generalizing the concept to include a wide class of electronic devices exhibiting memristive behavior [7]. This paper, *Memristive Devices and Systems*, laid the theoretical groundwork for the development of new types of electronic systems, including future solid-state memristors.

For decades, the memristor remained a theoretical curiosity without a physical

realization. It was not until 2008 that a research group at HP Labs, led by Stanley Williams, succeeded in building the first physical memristor using thin films of titanium dioxide ( $\text{TiO}_2$ ). This device clearly demonstrated the behavior predicted by Chua and paved the way for a new generation of memory and non-volatile logic systems [6].

The device developed by Williams and his team was based on an ionic drift mechanism within the  $\text{TiO}_2$ , which altered the device's resistance depending on the current passing through it. This discovery opened the door to the development of resistive memories (ReRAM) and other emerging applications, such as neuromorphic systems and reconfigurable logic circuits [10].

The memristor holds enormous potential in various areas of electronics. In particular, its unique properties make it especially suitable for:

- Non-volatile memory: thanks to the memristor's ability to retain its resistive state even when the power is off, it can be used as a memory element in ReRAM systems, which promise to replace flash and DRAM memories in future devices [10].
- Neuromorphic systems: memristors can be used to build artificial synapses in neuromorphic systems that mimic the functioning of the human brain. This could revolutionize the field of artificial intelligence by improving the efficiency of learning and memory processes [11].
- Reconfigurable logic circuits: memristors can be used in combination with transistors to create reconfigurable logic circuits, offering new possibilities for programmable electronics [12].

The concept of the memristor can be extended to memristive systems, which generalize the idea to include devices whose behavior can be described in terms of differential equations that depend on state variables. Although more complex, these devices offer innovative possibilities in the design of advanced electronic circuits [7]. In particular, this Thesis explores the memristive behavior of silicon nanowires, which can be exploited in innovative biosensing applications.

## 2.2 Silicon Nanowires in Biosensing Applications

Silicon nanowires (SiNWs) represent one of the most promising technologies in the field of biosensors due to their nanometric size, which offers a high surface-to-volume ratio, and their unique electronic properties. Silicon nanowires are one-dimensional structures with diameters ranging from a few nanometers to tens

of nanometers and lengths that can reach several micrometers. Due to their reduced size, SiNWs provide a larger surface area for interaction with target biomolecules, making them particularly suitable as platforms for highly sensitive biosensors. The biofunctionalization of the nanowire surface allows for the anchoring of specific biological molecules, such as antibodies or aptamers, that selectively recognize and bind to target molecules present in the sample [13][14]. These nanomaterials can be designed to precisely and sensitively detect a wide range of biomolecules, including DNA, proteins, and other biomarkers.

In recent years, SiNWs have been used to develop label-free biosensors, devices that do not require the use of chemical markers for signal detection. These biosensors offer an innovative solution for clinical diagnostics, reducing costs and analysis times while improving detection accuracy [13][15].

Moreover, the sensitivity of SiNWs allows for the detection of very low concentrations, significantly improving diagnostic precision and reliability, reaching femtomolar levels.

In addition, SiNW-based biosensors are particularly suitable for integration into point-of-care (PoC) devices, which enable rapid and portable diagnostics without the need for complex equipment [16][17].

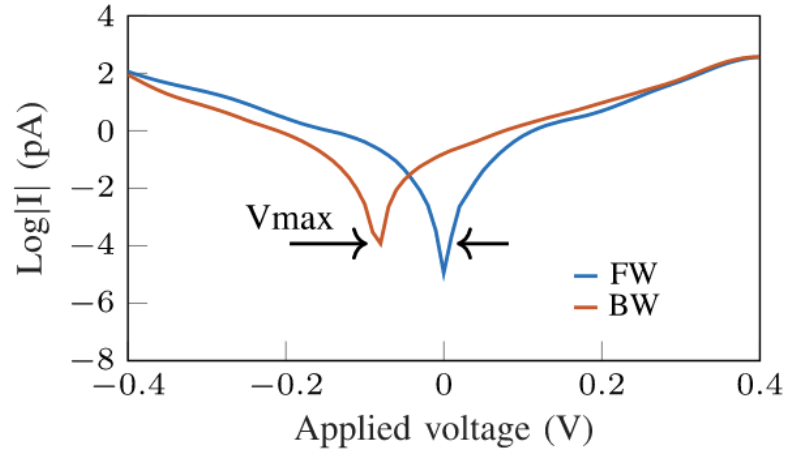
One of the applications that will be explored in this Thesis involves the detection of Prostate-Specific Antigen (PSA) using this technology.

PSA is a protein produced primarily by the prostate, and elevated levels of PSA in the blood are often associated with prostate cancer. PSA is commonly used as a biomarker for the diagnosis and monitoring of prostate cancer progression [14]. Prostate cancer is one of the most common malignancies among men, and PSA testing is one of the main tools used for early diagnosis. However, traditional methods, such as enzyme-linked immunosorbent assays (ELISA), have some limitations in terms of sensitivity and response times. For this reason, SiNW-based biosensors offer a valid alternative, thanks to their ability to detect extremely low concentrations of PSA, down to femtomolar levels, with greater speed and accuracy [13][14].

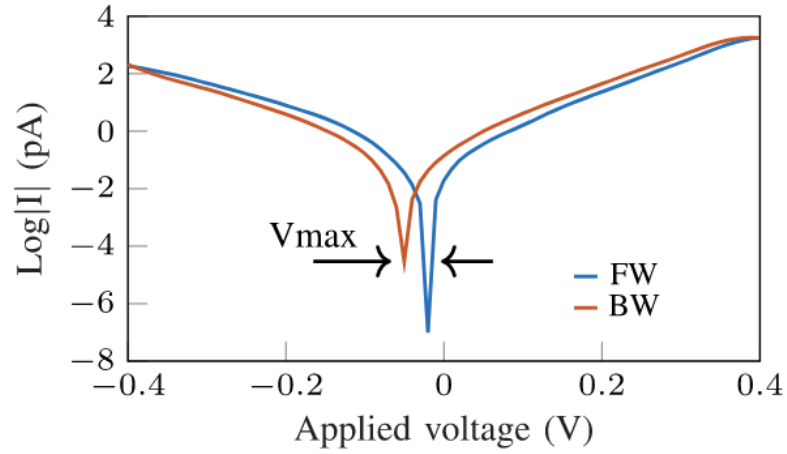
In PSA detection biosensors, the surface of the nanowires is functionalized with anti-PSA antibodies, after being treated with oxygen plasma or piranha solution [18]. These antibodies selectively bind to PSA present in biological samples, triggering a variation in the device's conductivity. This phenomenon allows for the monitoring of biomolecular binding through the measurement of variations in the current-voltage (I-V) curve, providing information on the concentration of PSA in the sample [15][19]. Specifically, if antigen-antibody binding has occurred, it causes a change in the surface charge distribution on the nanowire. This alters the memristance of the biosensor, as the device's resistance is no longer determined solely by the intrinsic

properties of the nanowire but also by the charges induced by the biomolecular binding.

Specifically, in non-functionalized nanowires, the current-voltage relationship shows a pinched hysteresis loop at zero voltage, except for parasitic effects. However, when biological substances are applied to the device surface, the hysteresis shifts from zero to different voltage values. This shift is not uniform between the forward and backward branches of the curve, creating an offset. In particular, after biofunctionalization of the nanowire, a voltage gap appears in the semilogarithmic current-voltage curve, reflecting an additional memory effect during the voltage sweep in the memristive biosensor. The biological substances around the nanowire generate additional charges that create an electric field around the memristive device channel, producing an effect similar to that observed in non-functionalized nanostructures but with a surrounding silicon gate. This all-around gate contributes to the particular conductivity of such structures, including the voltage shift in their electrical characteristics [20], as illustrated in Fig. 2.2.



(a)



(b)

**Figure 2.2:** I-V characteristic of memristive biosensor considering 3.3fM (a) and 330 fM (b) concentration of PSA [21]

In summary, a voltage sweep is applied through probes placed on the nanowire pads, and the I-V characteristic is measured. The results obtained before and after biofunctionalization are compared to detect the presence of biomolecules from an electrical measurement. This is schematized in Fig. 2.3.

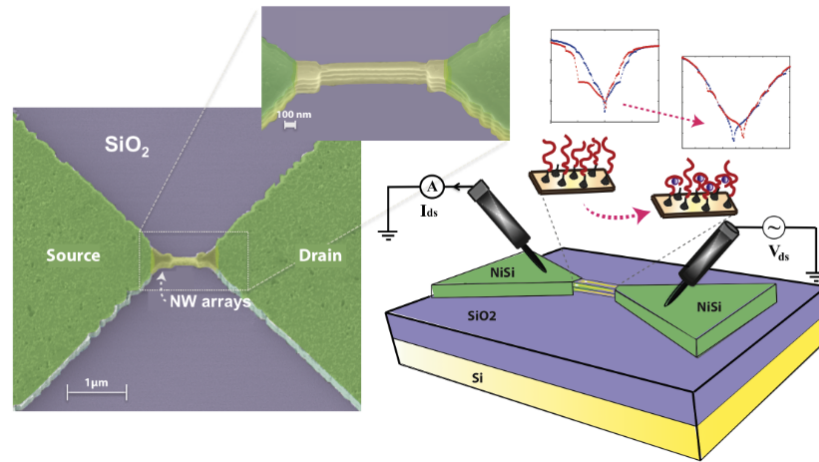


**Figure 2.3:** General framework for illustrating the measurement process for silicon nanowire biosensors [22]

### 2.2.1 Modeling of Silicon Nanowire

The structure of silicon nanowires can be modeled as a back-to-back diode structure, with two Schottky diodes [23], which in Fig. 2.4 are indicated as *dl* and *dr*. See Fig. 2.5 for the I-V characteristic of a diode and the band diagram of a p-type Schottky junction.

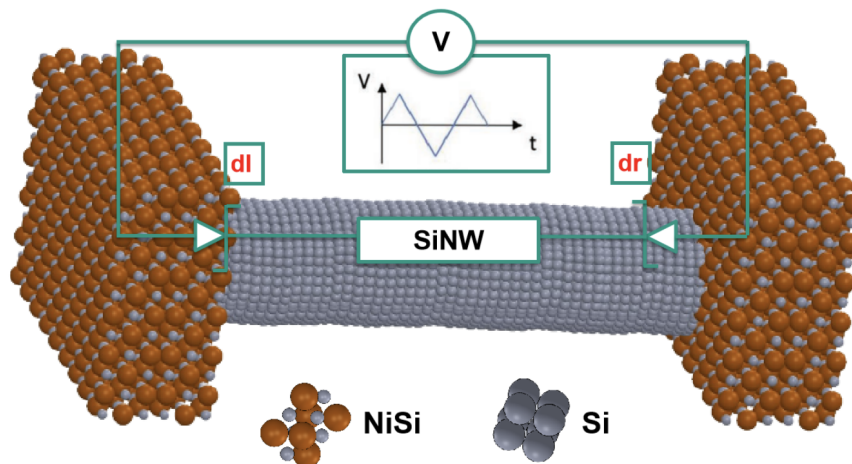


**Figure 2.4:** Structures of SiNW (back-to-back Schottky diodes) [23]

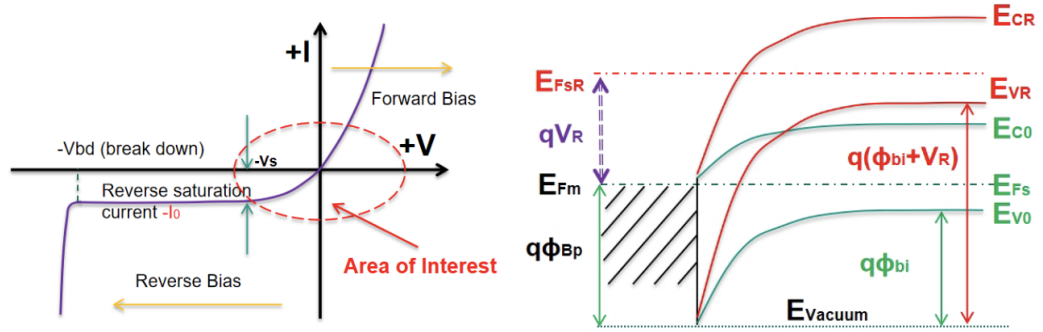


**Figure 2.5:** Electrical characteristic of a single-diode and band diagram for a p-type Schottky junction at equilibrium and in case of reverse bias [23]

From a circuitual perspective, models have been developed to simulate the electrical behavior of the memristive biosensor. In particular, the equivalent circuit shown in Fig. 2.6 and Fig. 2.7 was developed to model the behavior of the nanowire before and after biofunctionalization [24]. The models include the following elements:

- Memristor: the core of the model is represented by the memristor, which reproduces the characteristic hysteresis behavior observed in silicon nanowire biosensors.
- Schottky barriers: in silicon nanowire-based devices, the Schottky junctions formed between the metal and the semiconductor at the ends of the nanowire are modeled using a combination of diodes and resistances.
- Nonlinear capacitances: after biofunctionalization of the biosensor, the biological molecules bound to the surface of the nanowire introduce additional effects, modeled through nonlinear capacitances. These capacitances represent the accumulation of charges due to the presence of biomolecules, which generates an electric field around the nanowire. This effect leads to the formation of a voltage gap in the I-V curve, indicative of biofunctionalization and biomolecular interaction.
- Additional resistances and capacitances: to accurately model the electrical properties of the device, additional resistances and capacitances are included in the equivalent circuit. These elements help describe the overall behaviour of the biosensor, including capacitive and resistive effects due to the nanowire structure and its interaction with the surrounding environment.

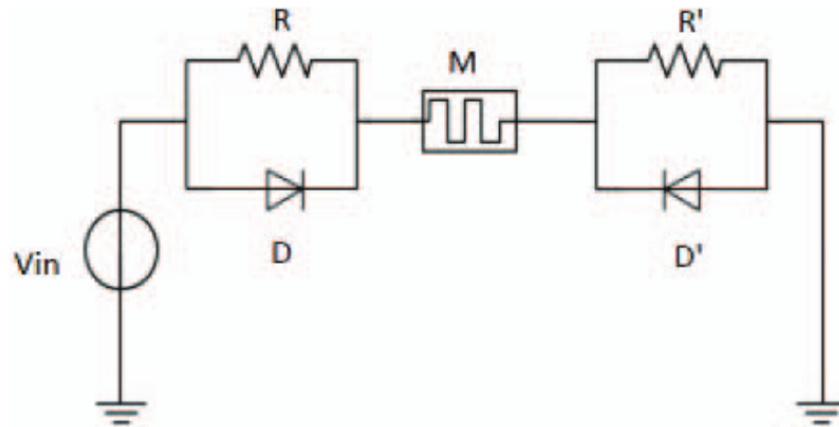


**Figure 2.6:** First equivalent circuit of memristive biosensors [24]

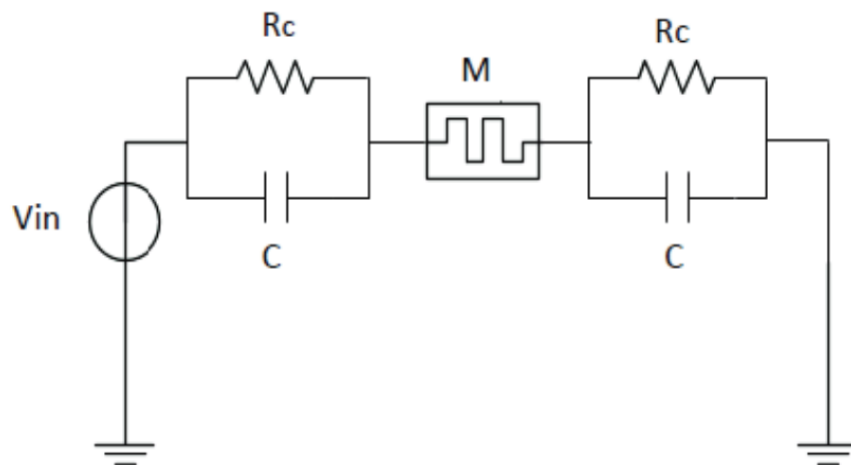


**Figure 2.7:** Second equivalent circuit of memristive biosensors [24]

## Chapter 3

# Microfluidic Systems for Biosensing

This chapter explains the key concepts of microfluidics and describes its main applications as reported in the literature. Its advantages are explored, which motivated integrating a microfluidic platform into the biosensing device described in this Thesis.

Finally, after introducing the physics of nanowires used as biosensors in Chapter 2 and the basics of microfluidics in this chapter, a general overview of the entire device will be provided. Each of its components will be examined in detail in the following chapters, looking at both designing and manufacturing aspects.

### 3.1 Fundamentals of Microfluidics

Microfluidics is the branch of science that deals with the study of fluids that flow in a network of tiny channels with a width of tens to hundreds of micrometres, and a volume ranging from femtoliters to microliters [25].

The physics of fluids at the micron scale differs from that observed at the macroscopic scale. This section describes the fundamental characteristics of the former in order to elucidate the differences between the two.

Two distinct types of flow can be identified:

- Hydrodynamic flow
- Electrokinetic flow

In the former, the fluid profile inside the microchannel is parabolic. The fluid velocity is maximum at the centre of the channel, the point corresponding to the vertex of the parabola, and decreases towards the edges. For hydrodynamic flow, there is no slip at the walls, where the fluid velocity is ideally null.

In the latter, the fluid profile is almost flat, with a constant velocity along the entire channel section, leading to the concept of "moving walls" [26].

This is illustrated in Fig. 3.1 and in Fig. 3.2

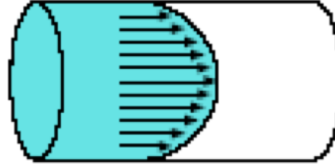


**Figure 3.1:** Hydrodynamic Flow [27]

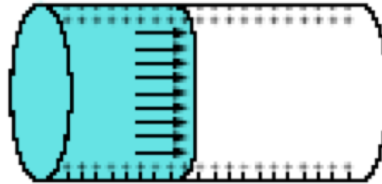


**Figure 3.2:** Electrokinetic Flow [27]

The behavior of fluid in channels is significantly influenced by its flow regime, which is characterized by the Reynolds number ( $R_e$ ) [28]. It is the dividing line between laminar and turbulent flow.

The Reynolds number is calculated as shown in Eq. (3.1).

$$R_e = \frac{\rho U L}{\eta} \quad (3.1)$$

- $\rho$  is the density of the fluid
- $U$  is the velocity of the fluid
- $\eta$  is the viscosity of the fluid
- $L$  is the characteristic length of the duct, which coincides with the hydraulic diameter, equal to  $D_h = \frac{4A}{P}$ , where  $A$  is the cross-sectional area and  $P$  is the wet perimeter of the duct.

In particular,

- if  $R_e < 2300$  the flow is laminar
- if  $R_e > 4000$  turbulence (mixing) occurs

In microfluidics, given the size of the channel and the dependence of  $R_e$  on  $L$ , the Reynolds number is always close to unity, thus the flow is completely laminar [29]. This has several physical implications. For example, the presence of laminar motion implies that two fluids injected into the same microchannel will not mix, but will continue to flow in parallel. The only phenomenon responsible for the mixing of the two fluids is diffusion: over time, the fluids mix due to the concentration gradient within the channel. For this reason, microfluidic mixers are nothing more than serpentine channels whose shape increases the length of the fluid's path and thus its time remaining in the channel, favouring the diffusion phenomenon. An alternative is to introduce external perturbations, for example by injecting a fluid from a channel perpendicular to the main one, to alter the laminar motion.

Another fundamental number in the context of microfluidics is the Péclet number ( $P_e$ ), which is a dimensionless quantity expressed by Eq. (3.2). The Péclet number is defined as the ratio of the diffusion and convection rate of a substance within a fluid [28].

Microfluidics is distinguished by a relatively low value of  $P_e$  ( $P_e \ll 1$ ), which aligns with the prevalence of laminar motion as previously discussed. Indeed, in the case of a substance immersed in a fluid, the phenomenon of diffusion will prevail. This property facilitates the manipulation of minute volumes of fluid with precision [30].

$$P_e = \frac{1}{2} \frac{t_{convection}}{t_{diffusion}} = \frac{\mu \cdot L}{D} \quad (3.2)$$

- $D$  is the diffusion coefficient of the material mixed in the fluid
- $\nu$  is the fluid velocity
- $L$  is the characteristic length of the system

### 3.1.1 The Correlation Between Microfluidics and Electronics

It is not uncommon to seek analogies and parallels between disparate physical domains. The objective is to develop equivalent models of a complex system in order

to facilitate the study of this system using a well-established set of analytical tools. It can be demonstrated that the analogy between different physical domains is an accurate representation of the underlying energy principles, as the fundamental laws that govern energy in a system are often consistent across various domains. This enables the identification of corresponding laws in disparate fields of physics, thus facilitating the utilisation of established equations and tools, which are characteristic of a domain that has already been subjected to investigation.

This principle also applies to microfluidics. It is feasible to correlate each microfluidic system with an equivalent electronic circuit. Indeed, there are analogies that permit the establishment of a parallelism between microfluidics and electronics, thereby enabling the study of the former with equations and physical laws that are already known, as they are specific to electronics. It is indeed possible to define fluidic resistance, capacitance and inductance in microfluidics by analogy with the electrical counterparts.

Fluidic resistance may be defined as the proportional constant between the pressure difference in a microfluidic channel and its flow rate. In this context, fluidic resistance is analogous to electrical resistance in ohmic conductors, which is the proportional constant between voltage and current. To understand this statement, the starting point is the Poiseuille's Law (Eq. (3.3)), which relates the flow rate  $Q$  to the pressure variation  $\Delta P$  in a channel [31].

$$\frac{dV}{dt} = Q = \frac{\pi r^2 \Delta P}{8\eta l} \quad (3.3)$$

- $V$  is the volume of the fluid
- $t$  stands for time
- $Q$  is the flow rate
- $r$  is the "radius" of the channel
- $\Delta P$  is the pressure variation along the channel
- $\eta$  is the viscosity of the fluid
- $l$  is the length of the channel

Note that given the channel geometry and the type of fluid injected,  $\frac{\pi r^2}{8\eta l}$  is a constant. Therefore, the relationship between  $Q$  and  $\Delta P$  is the one shown in Eq. (3.4).

$$\Delta P = R \cdot Q \quad (3.4)$$

where  $R$  is the fluidic resistance.

$$R = \frac{8\eta l}{\pi r^2} \quad (3.5)$$

The parallel with Ohm's law,  $V = R \cdot I$ , where  $V$  is the voltage,  $R$  is the electrical resistance and  $I$  is the current, is obvious.

In addition to fluidic resistance, capacitance can also be defined as the storage of pressure by the fluid and the surrounding geometry [27]. For example, the concept of capacitance is associated with elastic walls and membranes.

Finally, inductance can be defined as the flow inertia of the fluid and surrounding geometry [27]. In microfluidics, inductance values are often negligible.

Once the correlation between microfluidic and electronic quantities has been established, it is possible to construct an equivalent electronic circuit for a microchannel system. To this end, it is sufficient to associate each channel element with a resistor and a voltage generator where pressure differences exist.

## 3.2 Microfluidic Applications: State of the Art

On the foundations of the fundamental principles of physics, it is possible to investigate the principal applications of microfluidics. Initially, microfluidics was only exploited for proof-of-concept studies, whereas today it becomes a valuable tool for biotechnological applications, including screening and analytical tools [25]. In particular, it is often employed for drug delivery, biosensing devices [32], biofuels [33] and material synthesis [34].

One application often associated with microfluidics is lab-on-a-chip (LOC). These devices arise from the desire to transfer all the workflow tasks traditionally performed in an entire laboratory onto a single chip. In a LOC, for example, there may be areas dedicated to mixing or separating multiple samples, areas where specific reactions take place, and other zones dedicated to sensing [35][36].

Microfluidics also enables the development of point-of-care (PoC) diagnostic devices [37], which are portable and compact tools designed to quickly analyse biological samples without the need to send the sample to external laboratories.

Other applications that exploit microfluidics are agarose gel electrophoresis and capillary electrophoresis. The former is aimed at separating and visualising DNA or RNA fragments according to their size; the latter is a technique in which an

electrophoretic separation takes place in a narrow-bore fused silica capillary. An example is provided in [38].

Another widely used approach is droplet microfluidics [39]. This involves the separation of fluid droplets with precise control of their volume and velocity. This technique is used, for example, in droplet digital PCR [40].

Microfluidics is also widely adopted for cell culture and processing platforms. Advances in this field are reflected in related fields, including genomics [41], proteomics [42], transcriptomics [43] and metabolomics [42] of individual cells. These are often referred to as *Omic*s [25].

In general, microfluidics is valued for its ability to optimise the amount of reagents and samples used, whereby small volumes are channelled into the area of interest of the instrument. This frequently leads to a reduction in costs, lower consumption levels and shorter analysis times. This is particularly advantageous when only a restricted quantity of reagents is available.

Moreover, by confining the sample within the active region, the risk of cross-contamination can be mitigated.

Ultimately, microfluidics facilitates the fabrication of compact devices that can be incorporated with other instruments as sensors, as exemplified by the device developed in this Thesis.

Moreover, in the context of silicon nanowires as memristive sensors, the integration of microfluidics guarantees the maintenance of optimal humidity conditions essential for the optimal functioning of biosensors, particularly during the biofunctionalisation and incubation phases of antigen and antibody [44].

### 3.3 Overview of the Final Device Design

After explaining the basic pillars of the device, such as the physical characteristics of the nanowires used as biosensors (Chapter 2) and the fundamentals of microfluidics (Chapter 3), the final form of the device is sketched out.

The silicon chip will comprise 24 nanowires, arranged in four arrays of six, and fabricated in accordance with the process flow outlined in Chapter 5. Each nanowire will be anchored to nickel silicide (NiSi) pads, from which a pair of metal electrodes will emerge. Their function will be to preserve the integrity of the pads throughout the measurement process and to facilitate integration with microfluidic channels, as described in Chapter 6. The electrodes will extend to the periphery of the chip, with their extremities remaining uncovered by the microfluidic channels. This configuration will facilitate access to the probes utilized for the measurement

process, which is essential for detecting device signals and analyzing the sensed data.

The microfluidic platform will adhere to the chip, whose structure is detailed in Chapter 7. All the nanowires that make up the active region of the device will be covered by the microfluidic channels. They will transport the sample to the nanowires' surface and maintain the proper humidity conditions during the antigen and antibody incubation phases.

## Chapter 4

# Fundamentals of Microfabrication

### 4.1 Introduction to Microfabrication

The term *microfabrication* refers to the set of processes used to create structures and devices on a micrometer and nanometer scale. Microfabrication is a cornerstone of modern technology, underlying the development of integrated circuits (ICs), microelectromechanical systems (MEMS), biosensors, and a wide range of devices used in fields such as electronics, biomedicine, and telecommunications. Its role is crucial in enabling technological advances, as it allows for the production of complex devices on scales that are unattainable with traditional manufacturing methods.

Microfabrication employs a series of advanced techniques that can be classified into two main categories:

- *Top-down* techniques, where a larger substrate is initially sculpted or etched until the desired structure is achieved, such as in photolithography and etching.
- *Bottom-up* techniques, in which the desired structure is assembled layer by layer, such as deposition techniques and additive manufacturing.

Microfabrication includes additive processes, where material is deposited onto the substrate, and subtractive processes, where material is removed. Some of the fundamental processes used are photolithography, etching, thin-film deposition, and

doping. These processes allow for the creation of intricate patterns and functional components on substrates, such as silicon wafers, to build micro- and nanoscale devices.

### **4.1.1 Cleanroom Environment and Protocols**

All microfabrication processes described in this Thesis were conducted inside a cleanroom at the Center of Micro and Nanotechnology (CMi) of the École Polytechnique Fédérale de Lausanne (EPFL), following appropriate training for the correct use of the facilities and equipment.

The cleanroom is a controlled contamination environment where particulate concentrations are reduced and maintained below predefined levels, with temperature and humidity strictly regulated. The use of a cleanroom is crucial in microfabrication processes to prevent contamination that could compromise the quality and reliability of the produced devices. Contamination can affect the proper functioning of devices, reducing the yield of functional chips per wafer and increasing production costs, thus negatively impacting profits. Furthermore, contamination can damage equipment and, in some cases, pose a health risk.

The main types of contamination include particulate contamination, thin films, and atomic contamination. Contaminating particles can be either organic or inorganic, such as metallic dust, silicon, glass, quartz, as well as biological residues like skin, hair, textile fibers, makeup, and bacteria. Contaminating thin films include solvent residues such as acetone, isopropyl alcohol (IPA), propylene glycol monomethyl ether acetate (PGMEA), and traces left by insufficient rinsing or water stains. Finally, atomic contamination is the most difficult to control and is caused by the adsorption of unwanted atoms, ions, or compounds.

To minimize contamination, operators must wear cleanroom suits, gloves, shoe covers, face masks, head covers, and protective glasses, not only to protect themselves but, more importantly, to safeguard the integrity of the working environment and the devices being produced. Humans represent one of the main sources of contamination, as they release particles into the environment in the form of dirt and oils carried by shoes and clothing, as well as shed skin, hair, and perfume residues. The use of mechanical tools, such as tweezers, can also cause scratches on wafers or chips, further increasing the risk of contamination. Other sources of contamination include machinery in the cleanroom, materials used (chemicals, water, gases, and targets), and the environment itself.

Contamination can lead to significant problems. For example, impurities in silicon can act as recombination centers for electron-hole pairs, affecting the concentration

and distribution of charge carriers. Moreover, the presence of particles on the surface or in the reagents used during etching processes can interfere with photolithography, causing defects such as breaks or protrusions that generate shadowing effects, preventing the correct exposure of the underlying areas.

To reduce contamination risks, cleanrooms are equipped with HEPA and ULPA filters that purify the air. The laminar airflow, which flows from top to bottom, is crucial for keeping the environment particle-free. The layout of the equipment inside the cleanroom is also optimized to reduce air turbulence, using, for instance, perforated workbenches that promote continuous airflow.

International standards for the classification of cleanrooms has been established, dividing them into classes based on the concentration and size of particles present. Contamination measurements are performed using filtering and counting techniques or instruments that exploit optical scattering. There are two main cleanroom classification systems: the Federal Standard 209E (based on classes like 1, 10, 100, 1000, etc.) and the ISO 14644-1 standard. The Federal Standard 209E classifies cleanrooms by the maximum number of particles per cubic foot of air, with different particle sizes. The ISO 14644-1 standard, more widely used internationally, classifies cleanrooms from ISO Class 1 (the cleanest) to ISO Class 9 based on the number of particles per cubic meter of air.

At the CMi, on the BM-1 floor, there are ISO 5 zones, while ISO 6 areas are located on the BM+1 floor, as shown in Fig. 4.1.



Figure 4.1: Cleanroom top view and classification at CMi, EPFL

## 4.2 Photolithography

Photolithography is one of the main microfabrication techniques used to transfer patterns onto a substrate through the use of light. The term *photolithography* comes from the Greek words *photo* (light), *litho* (stone), and *graphein* (to write), literally translating to *writing with light on stone*. In this context, *stone* refers to the substrate being processed, which can be silicon, glass, or other semiconductor materials [45].

Photolithography is the most widely used microfabrication technique in the process designed for the realization of the bio-sensing device, the focus of this research project. Therefore, this section is dedicated to explaining its key elements.

The main components needed to carry out the photolithography process are:

- Substrate: the material on which the pattern is to be transferred, typically a silicon wafer.
- Photoresist: a light-sensitive polymer whose solubility changes after exposure to light.
- Mask: an opaque structure with defined openings according to the desired pattern, allowing light to selectively illuminate areas of the photoresist.
- Light source: generally an ultraviolet (UV) lamp, chosen based on the sensitivity of the photoresist.

Photoresist is one of the key elements of photolithography. It is a polymer provided in liquid solution, whose solubility changes after exposure to light of a specific wavelength. Photoresists are made up of a matrix, a solvent, and a photoinitiator. Photoresists are divided into two main categories:

- Positive photoresists: solubility increases in areas exposed to light, making them easier to remove during the development phase.
- Negative photoresists: solubility decreases in areas exposed to light, creating a pattern where only the unexposed parts are removed during development.

These properties of photoresists are exploited to transfer patterns onto the substrate, allowing precise selection of areas to undergo further treatments and masking those to be protected.

The photolithography process can be divided into the following main steps (see

Fig. 4.2):

- Coating: the photoresist is uniformly applied to the substrate using techniques like *spin coating*.
- Soft-baking: the photoresist is heated to evaporate the excess solvent and consolidate the film.
- Exposure: the substrate is exposed to UV light through a mask that defines the areas to be illuminated.
- Post-exposure baking (not always necessary): heating after exposure to stabilize the chemical reaction.
- Development: the more soluble parts of the photoresist are removed with a specific solvent.
- Hard baking (optional): additional heating to increase the chemical and mechanical resistance of the pattern.

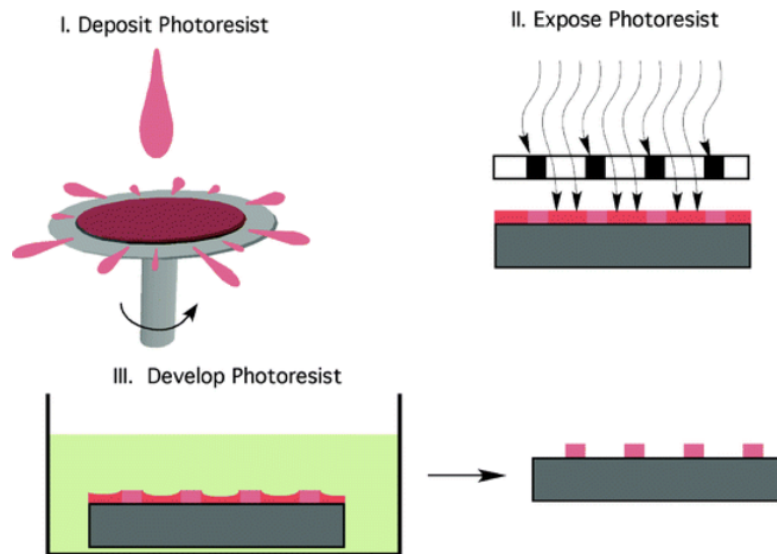


**Figure 4.2:** Main steps in a photolithographic process [46]

The first step of the process is coating the substrate with photoresist. A common technique for doing this is spin coating. The substrate, typically a silicon wafer, is placed on a rotating plate called a *chuck*. Vacuum is applied to hold the substrate in place, and then the photoresist is poured onto it. The plate is rotated at high

speed, distributing the photoresist evenly across the substrate through centrifugal force. The final thickness of the film depends on various parameters such as the viscosity of the photoresist, the rotation speed, and the duration of the process. It is important to develop specific recipes to achieve the desired thickness.

Soft-baking is a critical phase in which the substrate is heated for a specific time and temperature, defined by the characteristics of the photoresist. This step allows the solvent in the photoresist to evaporate, solidifying the photoresist film and preparing it for the subsequent exposure.

During the exposure phase, certain regions of the photoresist are illuminated according to the desired pattern. The light source is generally a UV lamp, as most photoresists are sensitive to this spectrum. The choice of UV wavelength affects the resolution of the pattern: shorter wavelengths, such as those used in deep UV (DUV) or extreme ultraviolet (EUV) lithography, allow for finer details.

To select the areas to be illuminated, a mask is used. It is an opaque structure with openings that allow light to pass through and hit only specific regions of the photoresist. In prototyping, to reduce the costs associated with mask fabrication, a laser source can be used to selectively illuminate the photoresist without the need for a physical mask.

There are various exposure methods (Fig. 4.3):

- Contact exposure: the mask is in direct contact with the substrate, ensuring high resolution but risking damage to the mask and substrate.
- Proximity exposure: there is a small gap between the mask and the substrate, reducing the risk of damage but introducing diffraction effects.
- Projection exposure: light is projected onto the substrate through a lens system, avoiding direct contact between the mask and substrate and improving resolution.

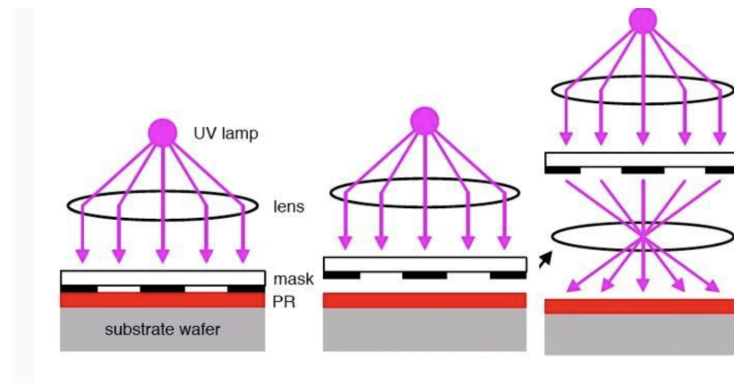


**Figure 4.3:** Exposure methods in photolithography [47]

After exposure, the photoresist is developed. This step uses specific solvents to remove the soluble parts of the photoresist. In positive photoresists, the areas exposed to light become soluble and are removed, while in negative photoresists, the unexposed part is removed, as shown in Fig. 4.4. The type of solvent varies depending on the photoresist and is specified by the manufacturer.

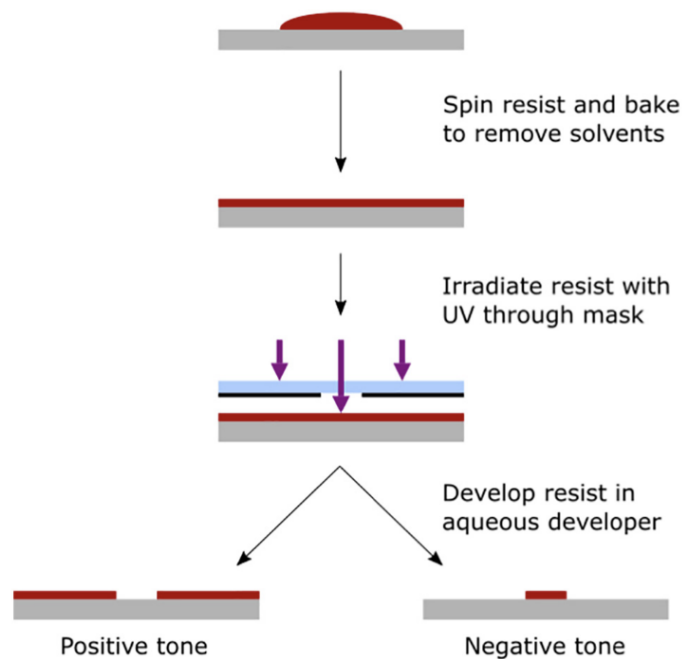


**Figure 4.4:** Comparison of positive and negative photoresists [48]

The final, optional step is hard baking. In this phase, the substrate is heated again to higher temperatures to increase the mechanical and chemical resistance of the photoresist pattern.

## Chapter 5

# Silicon Nanowires

### 5.1 Methods and Processes in Silicon Nanowire Fabrication

The physics of nanowires, along with their circuit models, is outlined in Chapter 2. The fabrication process, which was conducted by Dr. Junrui Chen, is now presented for detailed examination.

The aim is to produce suspended silicon-based nanowires that, after appropriate functionalisation, will serve as memristive biosensors for molecular sensing. This capability is achieved by forming a Schottky barrier between the nanowire and the nickel silicide (NiSi) pads. They act as electrical contacts, as described in Chapter 2. The main steps of the process are described below.

The substrate employed is a silicon-on-insulator (SOI) wafer, specifically a p-type SOI-725(625)-2-0.34  $\langle 100 \rangle$  with a resistivity ranging from 8.5 to 11.5  $\Omega\text{cm}$ .

The first step consists in substrate preparation: the wafer is cleaned to remove impurities and contaminants to ensure good adhesion of the materials to be deposited.

Subsequently, ZEP 520A photoresist is deposited via spin coating. The material is suitable for electron beam (e-beam) lithography, which is one of the principal techniques employed in this process. After that, a soft-bake step is undertaken with the objective of enhancing the adhesion of the resist to the substrate and facilitating the evaporation of the solvent (see Fig. 5.1).



**Figure 5.1:** Spin-coating on SOI wafer

This is followed by e-beam exposure to delineate the intended structures. As ZEP 520A is a positive photoresist, the selectively exposed areas are those that reduce its solubility and are then removed following the development stage.

The selected developer is an amyl-acetate solution, which is used to immerse the wafer for a period of between 1 and 2 minutes after the post-exposure bake (PEB), with the objective of removing the areas that have been exposed to the electron beam.

The substrate is bonded to a dummy wafer using glue, which remains stable throughout the subsequent steps.

The following step is the etching of both the silicon and silicon oxide ( $\text{SiO}_2$ ) of the substrate. It is then followed by an oxygen plasma treatment, which serves to remove the resist and clean the structure that has been fabricated. Its cross-section is shown in Fig. 5.2



**Figure 5.2:** Cross-section of fabricated structure after e-beam lithography and etching process

150 nm of methyl methacrylate (MMA) and 150 nm of poly-methyl methacrylate (PMMA) are spin-coated, exposed and developed (e-beam lithography). The developer used is a solution of methyl isobutyl ketone (MiBK) and isopropyl alcohol (IPA) in a 1:3 ratio (see Fig. 5.3).



**Figure 5.3:** Second stage of e-beam lithography for silicon nanowires fabrication

At this stage, a 50 nm layer of nickel (Ni) is deposited by e-beam evaporation, which is essential for producing the electrical contacts pads. The nickel is deposited uniformly on the wafer (Fig. 5.4), but after lift-off with acetone it remains only where the photoresist has been removed (Fig. 5.5).

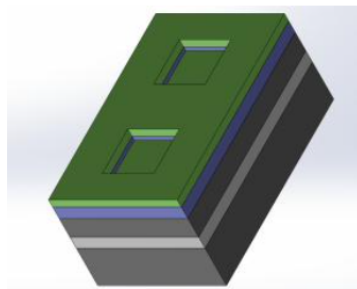


**Figure 5.4:** E-beam evaporation of 50 nm of nickel

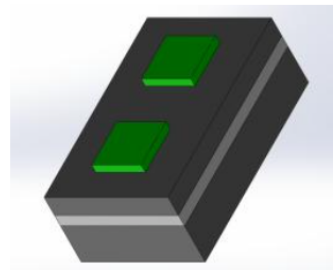


**Figure 5.5:** Final result after lift-off

Annealing at 400 °C for 20 min is required to form the nickel silicide, as depicted in Fig. 5.6.

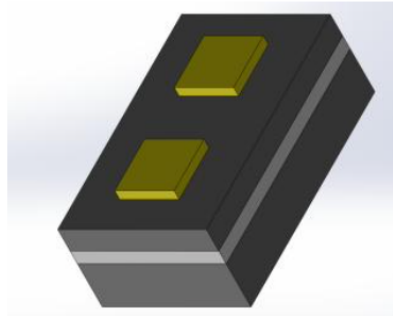


**Figure 5.6:** Nichel silicide formation after annealing step

In preparation for the next steps, a new oxygen plasma treatment follows for surface dehydration and activation.

The process continues with a new spin-coating cycle, using HSQ XR1541 002 resist, with a thickness of 50 nm. After soft-bake, e-beam exposure, and development (MF CD 26), the Bosch process is implemented to etch the silicon and define the final structure of the nanowires. These intermediate results are shown in Fig. 5.7 and Fig. 5.8.

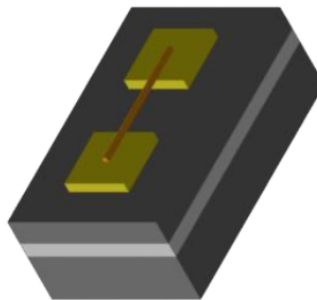


**Figure 5.7:** Third step of e-beam lithography for silicon nanowires fabrication

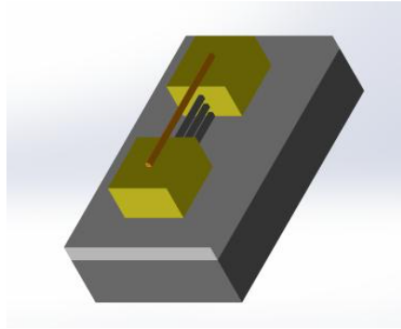


**Figure 5.8:** Final result after the Bosh process

Resist is stripped, as illustrated in Fig. 5.9.

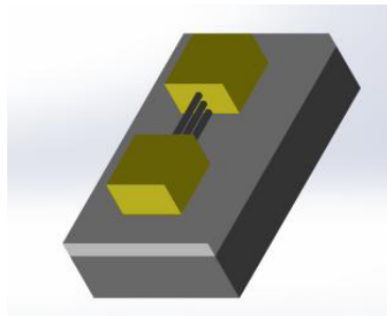


**Figure 5.9:** Resist stripping

Then, the negative photoresist AZnLOF2020 is spin-coated. Following the soft-bake, exposure and development with AZ 726 MIF (Fig. 5.10), the isolation evaporation is performed (Fig. 5.11), which is then followed by lift-off with acetone (Fig. 5.12).

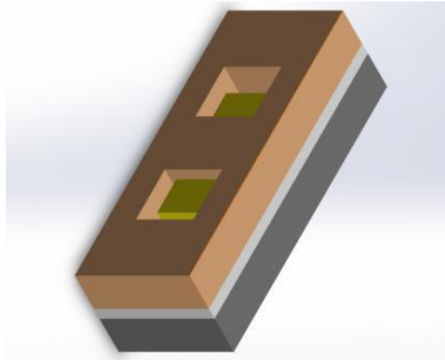


**Figure 5.10:** Fourth step of photolithography for silicon nanowires fabrication

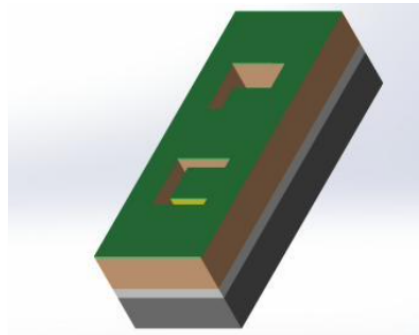


**Figure 5.11:** Isolator evaporation

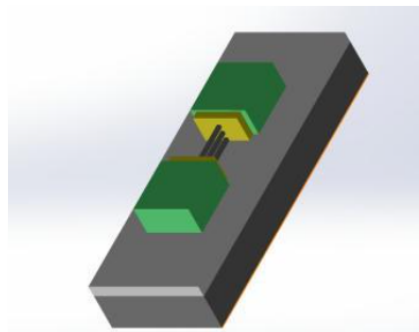


**Figure 5.12:** Final result after lift-off

Subsequently, a final cycle of photolithography is conducted, as depicted in Fig. 5.13. In this instance, the selected photoresist is AZ10XT-60.

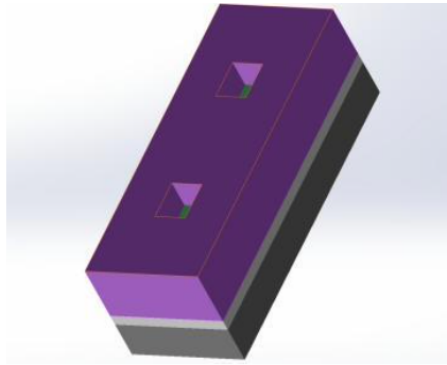


**Figure 5.13:** Fifth step of photolithography

The entire structure is then attached to a dummy wafer, after which ion beam etching ( $\text{SiO}_2$  etching) and resist stripping are conducted. The final result is shown in Fig. 5.14.

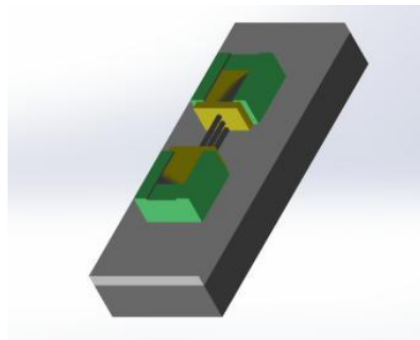


**Figure 5.14:** Final process flow step for the fabrication of silicon nanowires

Fig. 5.15 depicts SEM (Scanning-Electron Microscope) image of silicon nanowires anchored to NiSi pads.

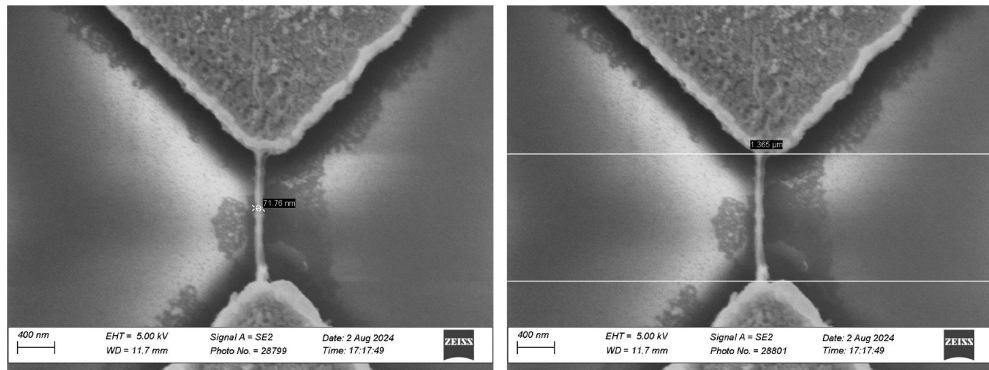


**Figure 5.15:** SEM image of silicon nanowires and NiSi pads

## Chapter 6

# Electrode Design and Fabrication for Memristor Integration

### 6.1 Electrode Integration: Requirements and Motivation

The integration of electrodes is a crucial yet non-straightforward process. Integrating a pair of electrodes for each nanowire is essential for several reasons.

On the one hand, considering the integration of a microfluidic platform, without electrodes extending the pads, once the channel is created over the nanowires array, the pads would be covered and it would no longer be possible to take measurements. Without electrodes, the device would be unusable.

Furthermore, the addition of electrodes also presents the advantage of preserving the pads themselves. The probe station used to apply a voltage sweep and measure current, as described in Sec. 6.4.1, has probes that are relatively large compared to the pads. Even when handling the instrument delicately, they tend to scratch the surface after each measurement, which over time would damage the device.

Finally, electrode integration simplifies the connection of the chip to other systems, such as a printed circuit board (PCB), thus speeding up the measurement process.

However, the integration of electrodes is not straightforward. Connecting the pads to the metal traces of the electrodes introduces a series resistance. Since the device is based on the memristive behavior of the nanowires, it is necessary to ensure that this added resistance does not mask the memristive behavior [49].

When designing the electrodes, reducing the introduced resistance is essential. Furthermore, it is important to ensure that each current path has the same resistance. In this way, it is possible to perform operations such as calculating the average and standard deviation of the voltage and current values obtained from repeated measurements.

## **6.2 Electrode Layout and Design Specifications**

Each nanowire has a pair of electrodes (source and drain). As mentioned in Sec. 6.1, the main objective is to minimize the resistance of the electrodes, which can be achieved by adjusting the cross-sectional area rather than the length, that is determined by design constraints. The length of the electrodes must be sufficient to avoid being covered by the microfluidic platform while leaving a margin from the edge of the chip to prevent issues during fabrication, such as edge effects.

Thanks to the thickness of the pads, about  $1\ \mu\text{m}$ , it is possible to achieve a sufficiently large cross-sectional area to significantly reduce the resistance. The goal is to maximize the width of the traces to increase the cross-sectional area, while considering space limitations.

The final design, created using KLayout, satisfies all the described requirements. The design is illustrated in Fig. 6.1. The nanowires and their respective pads are shown in red, while the electrodes are represented in blue. It can be seen that each nanowire is connected to its own electrode and a reference electrode.

The electrodes have an initial section with a non-constant width, which varies linearly, connecting to a section with a constant width. The initial section has a width of  $100\ \mu\text{m}$ , and the final section width is  $200\ \mu\text{m}$  for the thinner electrodes and  $300\ \mu\text{m}$  for the wider ones. This design allows for a practical and effective connection between the pads and the electrodes.

The reference electrode was designed with an even larger width,  $600\ \mu\text{m}$ , to ensure minimal resistance and greater signal stability, which is crucial for the proper functioning of the device.

Finally, when choosing the width, it is important to leave a minimum spacing between the traces, depending on the resolution of the photolithography machine

used for exposure; otherwise, the traces may overlap.

When selecting the final width of the electrodes, it is important to balance this with the length of the current path to achieve equal resistance. This was easily done using the Python code mentioned in Sec. 6.2.1.

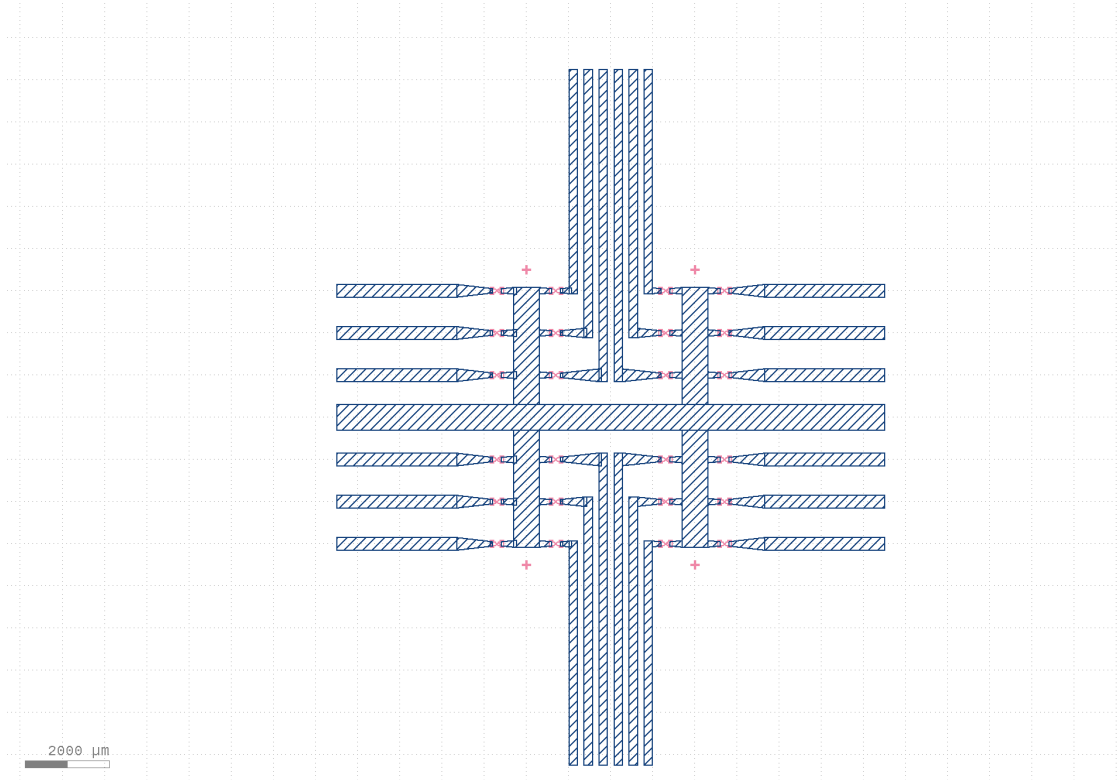


**Figure 6.1:** Design of electrodes (KLayout)

### 6.2.1 Computation of Electrical Resistance

The electrical resistance of a conductor depends on its resistivity  $\rho$ , the geometry of the conductor, and the material it is made of. In this section, two cases are examined: the first, where the trace width is constant along its length, and the second, where the width varies linearly along the length of the conductor. Specifically, the resistance will be expressed as a function of the trace width  $W(x)$  and thickness  $h$ .

In the case of a trace with a constant cross-sectional area, the resistance can be expressed as a function of the trace width  $W_0$  and thickness  $h$ . Since the cross-sectional area is  $A_0 = W_0h$ , the resistance can be calculated as:

$$R = \int_0^L \frac{\rho}{A_0} dx = \frac{\rho}{W_0 h} \int_0^L 1 dx = \frac{\rho}{W_0 h} \cdot L$$

Thus, the resistance for a trace with a constant cross-section is:

$$R = \frac{\rho L}{W_0 h}$$

In this case, the resistance  $R$  is inversely proportional to the trace width  $W_0$  and thickness  $h$  and directly proportional to the length  $L$ . This means that increasing the width or thickness of the trace decreases the resistance. This is intuitive because a larger cross-sectional area allows for easier electron flow, reducing resistance.

In contrast, increasing the length  $L$  results in a linear increase in resistance, as the electrons must travel a longer distance through the material.

In the case of a trace with a linearly varying width, the width can be expressed as a function of position  $x$  along the conductor. If the width  $W(x)$  varies from  $W_0$  to  $W_L$ , we can write:

$$W(x) = W_0 + \frac{(W_L - W_0)}{L} \cdot x$$

Since the cross-sectional area is  $A(x) = W(x)h$ , the resistance is given by:

$$R = \int_0^L \frac{\rho}{A(x)} dx = \int_0^L \frac{\rho}{W(x)h} dx$$

Substituting the expression for  $W(x)$ :

$$R = \frac{\rho}{h} \int_0^L \frac{1}{W_0 + \frac{(W_L - W_0)}{L} \cdot x} dx$$

To simplify the integral, we define:

$$b = \frac{W_L - W_0}{L}$$

so that  $W(x) = W_0 + b \cdot x$ , and the integral becomes:

$$R = \frac{\rho}{hb} [\ln(W_0 + b \cdot x)]_0^L$$

Substituting the integration limits  $x = 0$  and  $x = L$ :

$$R = \frac{\rho}{hb} (\ln(W_0 + b \cdot L) - \ln(W_0))$$

Simplifying further:

$$R = \frac{\rho}{hb} \ln \left( \frac{W_0 + b \cdot L}{W_0} \right)$$

Since  $b = \frac{W_L - W_0}{L}$ , substituting yields:

$$R = \frac{\rho}{h \frac{W_L - W_0}{L}} \ln \left( \frac{W_L}{W_0} \right)$$

Finally, the resistance for a trace with a linearly varying width is:

$$R = \frac{\rho L}{h(W_L - W_0)} \ln \left( \frac{W_L}{W_0} \right) \tag{6.1}$$

In this case, the resistance  $R$  depends on the width variation along the conductor. When  $W_L > W_0$ , the width increases along the conductor's length, progressively reducing the local resistance along  $x$ . The use of a logarithmic dependence reflects that the effect of the width variation is not linear, but depends on the ratio between the final width  $W_L$  and the initial width  $W_0$ .

As in the case of a constant cross-section, the resistance is inversely proportional to the trace thickness  $h$  and directly proportional to the resistivity  $\rho$  and the total length  $L$ .

These formulas are implemented in a Python code. This code significantly simplified the design process. By inputting a table containing the dimensions of the electrodes, the code outputs the resistance for each current path. The code's implementation is facilitated by the symmetry of the layout, and it can also be used to optimize

the electrode dimensions. Given the geometric constraints and inputting a desired resistance value with a certain tolerance, the code returns a table with the best combination of geometric parameters to meet the set requirements.

In the design used (Fig. 6.1), the resistance for each current path does not exceed  $1.7\ \Omega$  for any path, ensuring that the memristive behavior of the nanowires is not masked [49].

### **6.3 Electrode Fabrication Process: Lift-Off Method**

The fabrication process for the electrodes is based on the lift-off method.

The lift-off technique is widely used in micro and nano-fabrication to create metal patterns on substrates and is particularly appreciated for its versatility and precision. The lift-off process stands out for its simplicity and ability to avoid the use of chemical or physical etching techniques, which can be damaging to the underlying material or delicate structures.

The lift-off process involves several steps. First, the surface of the substrate is coated with a photosensitive resist via spin-coating. This resist layer is then exposed to ultraviolet (UV) light through a mask that defines the desired pattern. The exposure alters the chemical properties of the resist, allowing selective removal of the material in the exposed areas (for positive resist) or in the unexposed areas (for negative resist) during the development phase. The result is a resist pattern that acts as a "negative mold" for metal deposition.

A key feature of the lift-off process is that, once the resist has been developed, metal is deposited across the entire surface, but only the portion directly adhering to the substrate (and not on top of the resist) remains after the lift-off process.

One critical aspect of lift-off is managing the thickness of the resist: if the resist is too thin relative to the thickness of the deposited metal, the solvent may not effectively remove the resist and the metal on top, compromising the definition of the pattern. Therefore, selecting the appropriate resist thickness and accurately calibrating the exposure and development parameters are essential for the success of the process.

Fig. 6.2 shows the entire process flow developed for electrode fabrication. It will be discussed in more detail in the following sections.

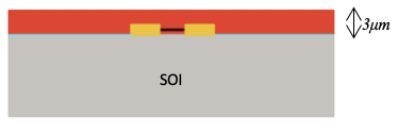
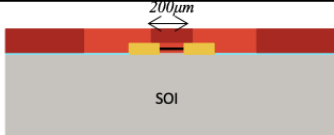
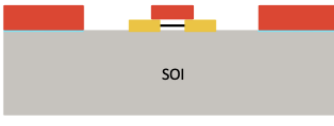
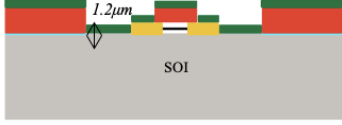
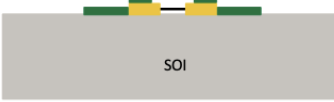
Step	Process description	Cross-section after process
01	<i>Wafer substrate preparation (optional)</i> Substrate: SOI wafer with Si-nanowires anchored between the NiSi pads located on the SiO <sub>2</sub> surface from SOI wafer Machine : YES 310TA(Z01) Material: HMDS	
02	<i>Photolith PR coat</i> Machine : Sawatec SM-200 (Z13) PR : AZ nLOF 2020 – 3 μm	
03	<i>Softbake</i> Hot-plate Temp. : 105°C	
04	<i>Photolith exposure</i> Machine : MLA150-2 (375nm) (Z16) Critical Dimension = 200 μm	
05	<i>Post exposure bake + development</i> Hot-plate Developer: AZ 726 MIF	
06	<i>Metal Evaporation</i> Machine : EVA760 (Z11) Metal : Ti (adhesion layer) / Au Thickness : 1.2 μm	
07	<i>Resist strip</i> Material : Acetone (overnight) or Technistrip P1316 Machine : Arias Base wet bench (Z13)	

Figure 6.2: Process flow for electrodes fabrication (lift-off)

### 6.3.1 Mask Fabrication

Once the electrode design is finalized, a mask can be fabricated to speed up the exposure process. This is particularly useful when working on a wafer rather than individual chips, as the exposure phase with a maskless aligner (MLA) machine

takes nearly an hour or more depending on the dose, compared to a few minutes with a mask.

Since mask fabrication is expensive, it is advisable to create one only when the electrode design is finalized and it is no more subjected to frequent changes and modifications. For the mask fabrication, the process flow from the CMi portal was followed [50], using the *Heidelberg Instruments VPG200* and *Hamatech HMR900* machines.

### **6.3.2 Photolithographic Process for Electrode Patterning**

The photolithography steps required to create the electrodes are detailed below.

The process begins with a substrate containing silicon nanowires and NiSi pads (see Chapter 5), followed by a thorough cleaning to remove any traces of dirt and residues through immersion in acetone for 3 min. This step is essential to ensure optimal adhesion of the photoresist and to avoid contamination that could compromise subsequent processing.

After cleaning, the negative photoresist AZnLOF2020 is uniformly applied to the substrate to achieve a thickness of approximately 3  $\mu\text{m}$ , using the *Sawatec SM-200* spin coater. According to the spin-coating curve in Fig. 6.3, a recipe corresponding to a chuck speed of 1,500 rpm is set. The resist thickness is crucial for ensuring the correct pattern definition and electrode formation during the exposure and development stages. This step is followed by soft-baking at a temperature of 105  $^{\circ}\text{C}$ , which aims to remove residual solvents and stabilize the photoresist film.

The exposure is performed using a light source with a wavelength of 375 nm and a dose of 105  $\text{mJ}/\text{cm}^2$ . These parameters have been selected based on preliminary tests and the photoresist datasheet. The *MLA150* machine was used for this step. This method was preferred over using a mask, as most of the work was done on individual chips rather than entire wafers.

After exposure, the post-exposure bake (PEB) is performed to complete the chemical reactions induced by the light in the AZnLOF2020 photoresist. Since it is a negative resist, it hardens in the exposed areas. This step improves the resolution of the patterns and the stability of the film during development.

The photoresist is developed using the AZ 726 MIF developer, which, in combination with deionised water, selectively removes the unexposed areas of the resist, revealing the desired pattern. The quality of the development process is verified through

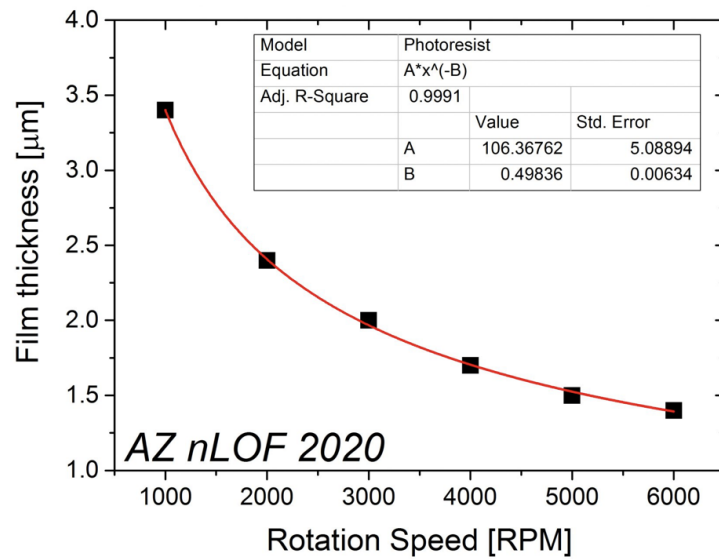


**Figure 6.3:** AZnLOF spin curve [51]

optical microscope inspection to ensure that the electrodes have been correctly formed with the required precision. The result is shown in Fig. 6.4.

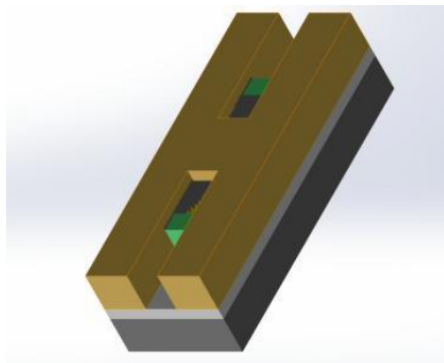


**Figure 6.4:** Representation of the device after photolithography

Achieving the optimal parameters for this process is the result of numerous experimental trials. Initially, the recommended values from material datasheets are used and progressively adapted based on the obtained results. Indeed, factors such as the specific machine used, the geometry of the pattern, and environmental conditions can significantly influence the final outcome. Therefore, the optimization process requires continuous iteration to obtain stable and reproducible results, ensuring that the electrode patterning is performed according to design specifications.

## **Photoresist Selection**

Several resists were tested before selecting AZnLOF2020 as the optimal choice for our needs. The decision to use AZnLOF2020 was the result of a thorough evaluation based on several fundamental parameters, particularly relevant when working on small chips.

The main parameters considered in the resist selection were:

1. Achievable thickness: The ability to achieve sufficient thickness is critical. AZnLOF2020 was selected in part because it can provide the required thickness without compromising other important properties, such as edge definition and substrate adhesion.
2. Viscosity of the photoresist: Viscosity is particularly critical, especially when working on very small chips, as in the initial prototyping phase on 8 mm x 8 mm chips. Highly viscous resists tend not to spread uniformly, creating uneven thicknesses, particularly at the chip edges. This is a significant problem because, in small devices, the edges represent an important area for patterning. If there are coating irregularities, the uniformity of the exposure dose is compromised, leading to incomplete or defective patterning. Lack of uniform coating can result in insufficient exposure dose in certain areas and, consequently, incomplete development or damage to the structures. AZnLOF2020, with its appropriate viscosity, demonstrated the ability to distribute uniformly even on the edges, ensuring a regular coating.
3. Ability to achieve a quality undercut: The ability to achieve an effective undercut is a fundamental requirement for the lift-off process, which requires that the deposited material separates cleanly from the resist to obtain well-defined electrodes. To achieve a good undercut, a bi-layer process is often used, with the application of a Lift-Off Resist (LOR). LOR is a sacrificial resist applied as a lower layer beneath the main photoresist. During development, the LOR is selectively dissolved compared to the overlying photoresist, creating an undercut, a recess beneath the photoresist. This space allows for the resist to be lifted off after metal deposition, separating the metal deposited on the surface from the metal deposited in the openings, facilitating resist removal and leaving intact electrodes. However, in our case, the available LOR at CMi did not achieve the desired thickness for the process. This led us to seek an alternative solution. AZnLOF2020 proved to be an excellent choice, as it can form an adequate undercut without the need for an additional LOR layer. This simplified the lift-off process, and improving the quality of electrode patterning.

### 6.3.3 Metal Selection and Deposition Process

Once the pattern with the photoresist is developed, metal deposition is the next step.

The metal evaporation technique is a physical process used to deposit thin metal films on a substrate. This method relies on the controlled vaporization of metal in a vacuum environment, allowing the metal vapor to condense and deposit uniformly on the surface of the substrate.

Physically, the process occurs inside a vacuum chamber, which significantly reduces the presence of gas molecules that could interfere with the trajectory of the evaporated metal atoms. The high vacuum ensures that the evaporated atoms can ideally travel in a straight line from the evaporation point to the substrate without significant collisions.

For the metal evaporation, the *EVA760* machine was used. A 500 nm layer of titanium (Ti), acting as an adhesion layer, was evaporated, followed by a 700 nm layer of gold (Au). The resulting structure is shown in Fig. 6.5.

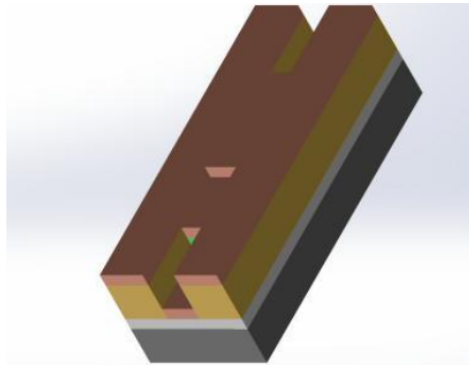


**Figure 6.5:** Graphical representation of the device after metal deposition

Among the various available conductive metals, gold was chosen due to its excellent electrical and chemical properties. Gold has one of the lowest electrical resistivities (about  $24 \text{ n}\Omega \cdot \text{m}$ ) and outstanding chemical stability, making it virtually immune to corrosion and oxidation, ensuring reliable long-term performance. However, if gold were directly deposited onto the substrate, delamination or peeling of the metal film, particularly along the edges, might occur, compromising the electrical contact quality and device integrity. To overcome this limitation, an adhesion layer is introduced.

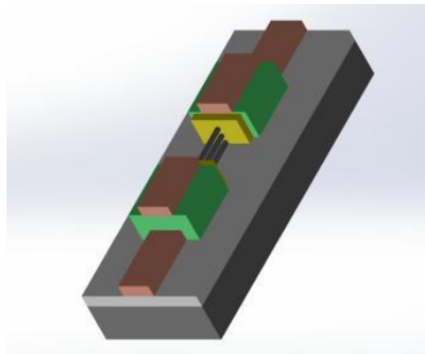
In practice, the most commonly used materials for the adhesion layer are titanium (Ti) and chromium (Cr). Titanium, in particular, slightly oxidizes on the surface, forming a titanium oxide layer that helps create a stable interface with the substrate, improving mechanical adhesion. Additionally, titanium is compatible with gold, allowing a strong bond between the two metal layers without compromising the conductive properties of the electrode.

The decision to prefer titanium as an adhesion layer over chromium was driven by two main factors. Firstly, previous experiments with a Cr+Au system under similar conditions to those used in this work had yielded less satisfactory results, particularly showing lifting and curling of the metal film edges.

Secondly, a practical consideration influenced the choice of titanium: some of the machines used later in the process, such as the *Tepla300* for oxygen plasma surface activation at CMI, prohibit the use of chromium. Titanium, on the other hand, does not have these limitations, making the process simpler and more versatile without requiring adjustments to the workflow.

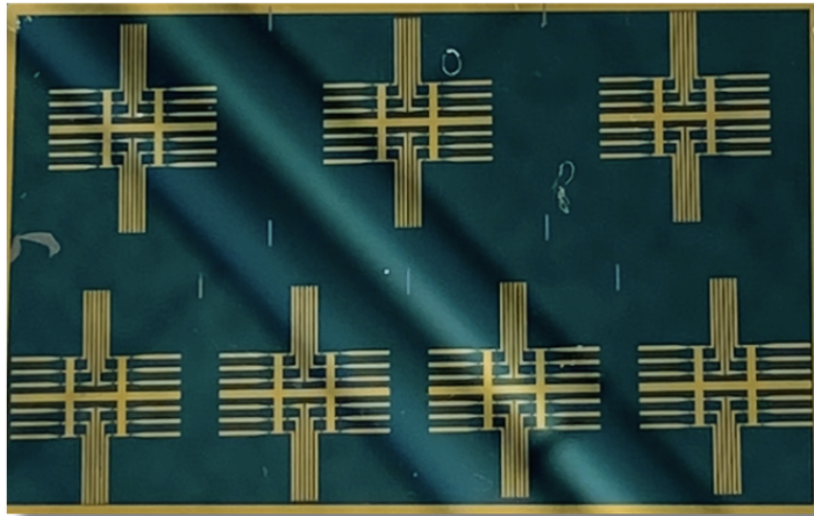
### 6.3.4 Final Fabricated Chip with Integrated Electrodes

After the metal evaporation (Ti+Au), the chip is immersed in acetone for 4 h or overnight, initiating the lift-off phase. The photoresist dissolves, consequently lifting off the over-deposited metal layer (see Fig. 6.6). At this stage, the importance of the photoresist undercut becomes evident.



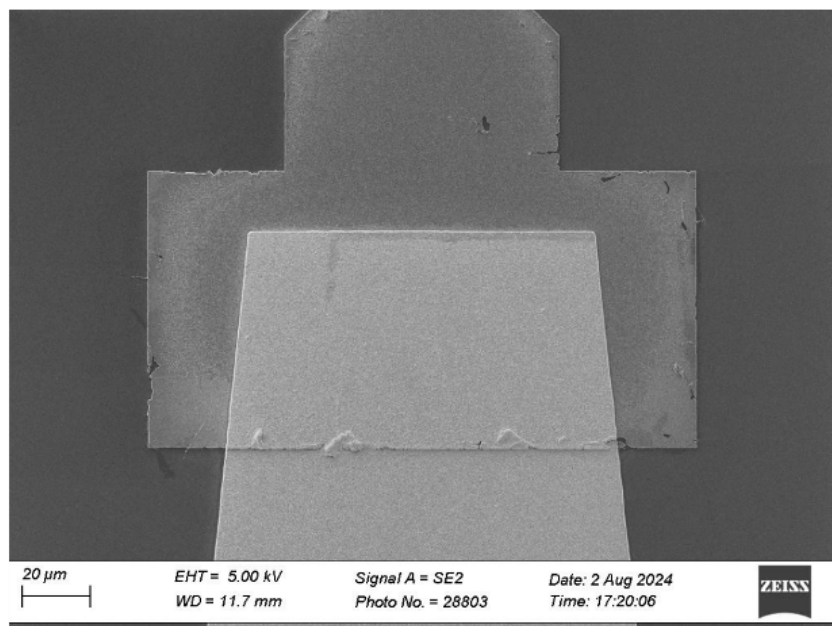
**Figure 6.6:** Graphical representation of the device after lift-off

Fig. 6.7 shows a portion of the wafer with chips and the fabricated electrodes.



**Figure 6.7:** Chips with silicon nanowires and integrated electrodes

Fig. 6.8 shows an SEM image displaying the contact between a portion of the gold electrode and the pad of a nanowire.



**Figure 6.8:** SEM image of NiSi pad and gold electrode

## 6.4 Electrode Characterization and Measurements

In this section, the measurement process used to characterize the electrodes is described. After detailing the measurement setup, a review of the possible outcomes after electrode integration is provided.

### 6.4.1 Measurement Setup and Instrumentation

The key elements of the measurement setup are as follows:

- Probe station
- Keithley 2602B SourceMeter
- PC with MATLAB code

The chip is placed on a probe station, which consists of a platform, called a *chuck*, that securely holds the wafer, chip, or other microelectronic components. It often includes a vacuum system to ensure that the device under test (DUT) remains stationary during the measurement phase. The primary function of a probe station is to allow fine manipulation of the probes, which are sharp metal contacts connected to high-precision instruments like the Keithley 2602B SourceMeter. These can be moved with micrometer-scale precision using micromanipulators.

The probe station is equipped with an electronic or optical microscope, allowing the operator to visualize the exact placement of the probes on the DUT. This visual feedback is crucial to ensure that the probes make proper contact without damaging the delicate structures of the device.

The Keithley 2602B is designed for highly accurate electrical measurements, often required in sensitive experiments involving low currents and voltages. For example, in bio-sensing or nanoscale electronics, where current levels can drop into the picoampere range, this instrument provides the precision needed for accurate data collection. It supports various measurement modes, including both single-point measurements and voltage sweeps. Furthermore, the SourceMeter's ability to both source and measure in the same device makes it particularly useful for experiments involving devices like the one designed in this Thesis.

The measurements are performed using a MATLAB script specifically written for this type of measurement. The MATLAB script automates the process of controlling the Keithley 2602B to perform voltage sweeps and measure the corresponding current.

The protocol used in the MATLAB script is based on the VISA-GPIB (Virtual

Instrument Software Architecture-General Purpose Interface Bus) communication standard. VISA (Virtual Instrument Software Architecture) serves as an abstraction layer that facilitates communication with instruments across multiple hardware interfaces, including GPIB. In this case, the VISA-GPIB combination allows the MATLAB software to issue commands to the Keithley 2602B, request data, and control the flow of measurements through a standardized communication interface. The GPIB interface enables the MATLAB script to communicate with the SourceMeter by sending SCPI (Standard Commands for Programmable Instruments) commands. SCPI commands are textual instructions that allow precise control of instrument settings, such as setting the voltage range, configuring measurement parameters, and requesting measured data.

The script begins by defining a voltage range for the sweep (e.g., from -4V to 4V, with a step size of 0.01V). Voltage is incrementally adjusted, and the SourceMeter measures the current at each voltage point. This is done iteratively, with the results stored in arrays for later use.

The script handles both forward and backward sweeps, essential for analyzing memristive components.

Once the data is collected, it is saved in a text file in ASCII format, making it easy to import into other software for further analysis or comparison with results from other experiments. The current data is plotted against the voltage, with the forward sweep shown in red and the backward sweep in blue. In addition to linear plotting, the script generates a semi-logarithmic plot, particularly useful for visualizing the voltage gap.

An important feature of the script is the calculation of the voltage gap ( $V_g$ ), which measures the difference in voltage between the forward and backward sweeps at the point of minimum current. This gap is indicative of hysteresis in the device and is crucial for characterizing the biosensor. The script calculates this voltage gap by finding the indices of the minimum current values in both the forward and backward sweeps and then subtracting the corresponding voltages. This gap is displayed and saved along with the rest of the data, enabling a quantitative analysis of the device's hysteretic behavior. This ensures the user has a complete record of the experiment, including both raw data and visualizations.

## **6.4.2 Electrode Performance Characteristics**

Two distinct scenarios may arise when measuring the electrode characteristics.

The first scenario is illustrated in Fig. 6.9. In this case, the metal (in yellow)

adheres well to the pads, creating a good contact without parasitic effects. The resulting characteristic curve is shown in Fig. 6.10, with a voltage gap close to 0 V.

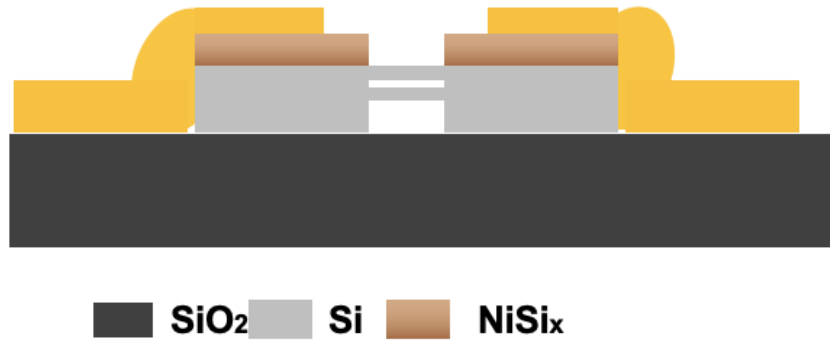


**Figure 6.9:** Silicon-nanowires and NiSi pads with good electrode connection

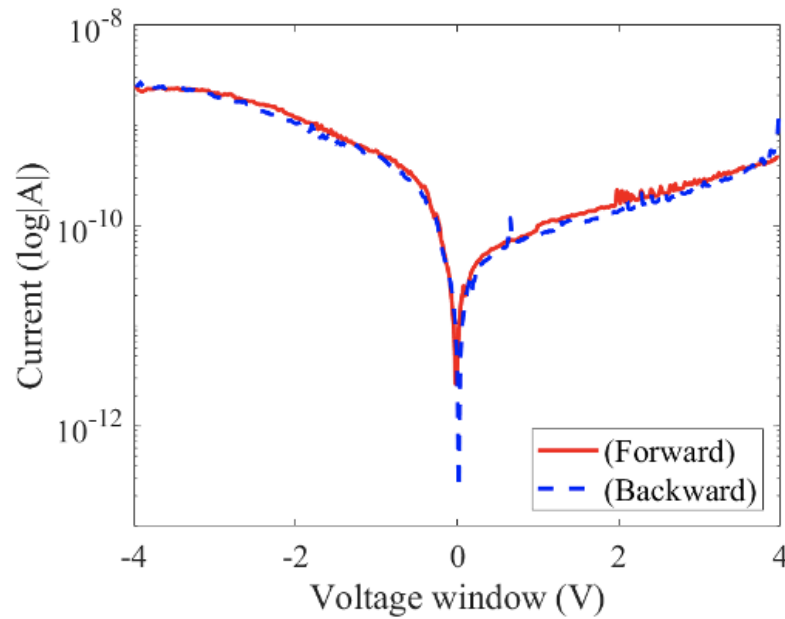


**Figure 6.10:** Good I-V characteristic of bare silicon-nanowire (integration of electrodes)

Fig. 6.11 shows an I-V characteristic where a non-zero voltage gap is observed, even though a bare nanowire was measured. This is due to parasitic effects. Evidently,

during the evaporation phase, the metal did not fully adhere to the side of the pad. The gap left between the NiSi surface and the gold surface forms a parasitic capacitance.

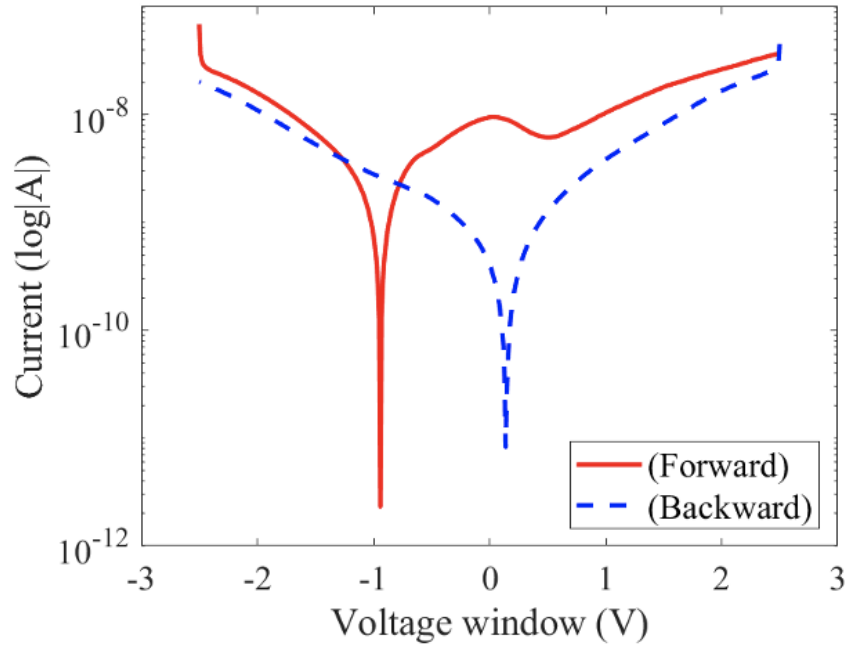


**Figure 6.11:** Effect of parasitic capacitance on I-V characteristic (integration of electrodes)

## Chapter 7

# Microfluidic Platform Development

This chapter sets out the requirements for integrating the microfluidic platform into the device described earlier, providing a justification for each design choice. Furthermore, it reviews the common manufacturing processes for fabricating microfluidic devices, concluding with the selection of the optimal process for this application.

### 7.1 Design and Requirements of the Microfluidic Platform

In the design of the microfluidic platform and the development of its fabrication process, a number of requirements must be taken into account. For the design, the following key points must be satisfied:

- The configuration of the channels must be aligned with the positioning of the nanowires on the chip surface. It is, in fact, the function of the microfluidic platform to concentrate the sample solution in the active area of the device, maintain optimal humidity conditions to favour chemical or biological reactions, and prevent evaporation after liquid samples have been incubated. Accordingly, the arrangement and configuration of the channels must encompass the entire active sensing zone of the device and then align with the arrangement of the nanowires on the chip.

- The width and length of the channels are of critical importance in the design of the microfluidic platform. In addition to the aforementioned considerations, two further factors require attention: the alignment procedure and the presence of electrodes. The alignment between the channels and the chip with nanowires and electrodes is conducted manually, facilitated by an optical microscope. It is therefore essential to allow for a margin of a few tens of microns in the width and length of the microfluidic channels, in comparison to the actual width and length of the nanowire array. Furthermore, it is of paramount importance to include a margin between the channel wall and the edge of the platform. It is essential that the platform be sized to leave a portion of each electrode uncovered, thereby ensuring the efficacy of the measurement process. The requisite margin enables the bonding of the microfluidic platform to the chip, thereby ensuring the availability of sufficient material for effective adhesion between the two surfaces and the prevention of leakage.
- The height, length and width of the channels must also be adjusted to stay within the volume limits. In this application, the maximum available volume of solution is 20  $\mu\text{L}$ , so the total volume of the channels must not exceed this limit. For  $N$  straight channels with rectangular cross section, length  $L$ , width  $w$  and thickness  $t$ , with circular inlets and outlets of radius  $r$ , the condition can be approximated as

$$N \cdot (L \cdot w + \pi r^2) \cdot t < 20\mu\text{L} \quad (7.1)$$

- An additional parameter that merits attention is the fluidic resistance, which is dependent on the dimensions of the channel, specifically its height, width, and length. In the case of a channel with a rectangular cross-section, the fluidic resistance can be approximated by the Eq. (7.2) [31].

$$R_f = \frac{12\eta L}{wt^3} \quad (7.2)$$

It has been demonstrated that the resistance is inversely proportional to the cube of the channel height,  $t$ . An increase in channel thickness can result in a notable reduction in fluidic resistance, provided that the length and width remain constant. However, any increase in height must be balanced against other requirements, such as the total volume of the channels and their mechanical stability, which is influenced by their aspect ratio. Furthermore, the maximum achievable aspect ratio is subject to the constraints of the manufacturing process and the selected material.

In this specific instance, each chip comprises nanowires arranged in four parallel arrays, which allows for the implementation of multiple channel designs. One of the

most straightforward solutions is to create four parallel channels, with one dedicated to each array of nanowires. All the channels are equipped with a separate inlet and outlet. Alternatively, a common outlet for all channels may be designed. An alternative methodology is to create two larger parallel channels, each encompassing two adjacent arrays of nanowires. This design permits the creation of larger inlets and outlets, thereby enabling the available tubes to be inserted directly, obviating the necessity for additional needles.

In addition to the conventional straight channels, more intricate configurations have been investigated, including the incorporation of Y or T junctions, which facilitate the distribution of flow from a single inlet to multiple channels. However, these solutions necessitate the use of a larger platform, introduce longer channels, and therefore require higher fluid volumes for a given thickness. Furthermore, these more complex configurations are associated with higher fluidic resistance, which may compromise system efficiency.

The following points should be taken into account when selecting a manufacturing technique:

- It is recommended that a transparent material be used for the channels, allowing for direct observation of the interior of the channels with the naked eye, for instance during the sample injection phase, or with an optical microscope for subsequent analysis.
- A material that does not interact with the biological samples introduced into the channels is recommended in order to avoid any alteration in the sensing performance of the device.
- It is of great importance that the microfluidic platform is effectively integrated into the silicon chip that houses the nanowires, pads and electrodes. This implies that the material must adhere perfectly to the surface of the chip, with no leakage either at the lateral edges or between adjacent channels. The absence of this requirement would have an impact on the overall performance of the device.
- For the manufacturing process, solutions that add excessive complexity to the device should be avoided. Therefore, for the same performance and suitability for our application, microfabrication techniques that are fast, easily reproducible, less sensitive to process variations and cost-effective are preferred. The ultimate goal is to minimise the risk of process failure during prototyping and to facilitate replicability.

For a detailed description of process selection, see Sec. 7.2 and Sec. 7.3.

## 7.2 Methods for Microfluidic Fabrication

A variety of fabrication methods have been explored in the literature for the realisation of microfluidic devices. Some of the most popular techniques are listed below [48].

- Polydimethylsiloxane (PDMS) platforms made using the SU-8 moulding technique (Soft-lithography)
- Polymethyl methacrylate (PMMA) platforms, e.g. produced by hot embossing
- Platforms with microfluidic channels in SU-8 with glass covers
- Paper-based microfluidics [52]
- Embedded SCAffold RemovinG Open Technology (ESCARGOT) method [53]
- Microfluidic platforms made by 3D printing

The aforementioned techniques were subjected to an in-depth analysis with the objective of identifying the most suitable one in accordance with the requirements listed in Sec. 7.1. Specific consideration was given to the SU-8 technique for the fabrication of microchannels and the SU-8 moulding technique for the fabrication of PDMS structures, as these techniques were identified as the most promising for the application under study. This analysis is further explored in the following sections (Sec. 7.2.1, Sec. 7.2.2).

Finally, SU-8 moulding has been identified as the optimal technique for the specified purposes, with PDMS identified as the preferred material.

### 7.2.1 SU-8-Based Channel Fabrication

This section sets out the principal stages of the process by which microchannels are fabricated using a particular photoresist, designated SU-8.

This process flow has been developed based on the detailed explanations and comprehensive training provided by the staff of the Center of MicroNanoTechnology (CMi).

SU-8 is a negative epoxy photoresist that is widely employed in microfabrication, particularly for the fabrication of 3D structures such as microfluidic channels, due to its exceptional mechanical and chemical properties. The main chemical composition

of SU-8 is based on a novolac epoxy resin, specifically an oligohemer with eight epoxy units, which is the origin of the resin's name. This resin is combined with a solvent, such as cyclohexanone or gamma-butyrolactone, to facilitate deposition by techniques such as spin-coating, and a photoactive sensitiser, typically a cationic photoinitiator [54].

Following exposure to ultraviolet (UV) radiation, the photoinitiator initiates a photopolymerisation reaction that activates the cross-linking process of the epoxy chains in the irradiated regions, as illustrated in Chapter 4. As a negative photoresist, the areas exposed to UV light become insoluble in the developer, while the unexposed areas remain soluble and are removed during development.

One of the most distinctive features of SU-8 is its capacity to form thick films, with a thickness ranging from a few microns up to several hundred microns, while maintaining high resolution and vertical walls. This characteristic makes it a photoresist suitable for applications where well-defined 3D structures, with a thickness of tens or hundreds of microns, are required [55].

In this context, the initial stage of the process is the preparation of the substrate, which must be cleaned in order to facilitate the adhesion of the photoresist that is to be deposited. In the case of a chip comprising nanowires and metal electrodes, the cleaning process may be conducted by immersing the chip in acetone for a period of 2-3 minutes. The substrate is then prepared for the deposition of the SU-8 photoresist, which is performed by spin-coating. A recipe is selected that adjusts the speed of the chuck rotation in accordance with the desired thickness, which in turn determines the height of the microfluidic channels.

After spin-coating, a soft-bake is performed to evaporate the solvent. The chip is placed on a hot plate for a time specified by the manufacturer, depending on the type of photoresist and the thickness achieved. In general, recommended temperature is approximately 95 °C.

Once the exposure to the heat source has been completed, the subsequent step is to proceed with the UV exposure. As is standard practice, the operator may utilise a mask or alternatively, perform the exposure process utilising a laser source. It is crucial to recall that SU-8 is a negative photoresist, which implies that the regions subjected to exposure will retain their integrity following development. Accordingly, the portion of the chip subjected to light exposure should be the one that corresponds to the complementary part of the actual channel design.

Following exposure, an additional heat treatment, known as the post-exposure bake (PEB), is performed to promote cross-linking of SU-8 in the exposed areas.

The PEB conditions, such as time and temperature, must be set according to the manufacturer's recommendations.

The subsequent phase is the relaxation period, which is followed by the development phase. This latter phase is carried out in two separate baths, one containing propylene glycol monomethyl ether acetate (PGMEA) and the other isopropanol (IPA). Following immersion in PGMEA, the contact between the chip and IPA results in the formation of a whitish residue, which is indicative of the removal of SU-8. The process continues with alternating immersion in PGMEA and IPA until no white residue is observed, indicating that the development process is complete. A multi-stage development process enables greater control and reduces the risk of overdevelopment. The walls of the microfluidic channels are formed.

The channels must be sealed by the incorporation of a glass substrate, which, through its transparency, permits observation of the internal processes occurring within the channel. A variety of techniques may be employed to facilitate the bonding of glass to SU-8. These include oxygen plasma treatment, which modifies the surface of the two materials to enhance bonding, and the utilisation of silanising agents.

Once the structure is complete, a laser is employed to create holes in the glass at the entrance and exit points of the channels.

## 7.2.2 SU-8 Molding for PDMS

A popular alternative in microfluidics is the use of PDMS for channel fabrication. PDMS is a silicon-based organic polymer characterised by a chemical structure consisting of repeating units of  $-\text{Si}(\text{CH}_3)_2-\text{O}-$ , i.e. a backbone of alternating silicon and oxygen atoms with two methyl groups attached to each silicon atom, as shown in Fig. 7.1. Its empirical formula is  $\text{C}_2\text{H}_6\text{OSi}_n$ , while its fragment formula is  $\text{CH}_3[\text{Si}(\text{CH}_3)_2\text{O}]_n\text{Si}(\text{CH}_3)_3$ . Depending on the number of monomer repeats, PDMS can occur in different forms: liquid for a low  $n$  value or semi-solid for a longer monomer chain [56].

The distinctive structure of PDMS confers a number of advantageous chemical properties, including flexibility, thermal stability and chemical inertness. Furthermore, PDMS exhibits thermal stability, retaining its mechanical integrity even when subjected to temperatures above 200 °C. The viscoelastic nature of PDMS is responsible for its remarkable flexibility and elastomeric properties, enabling it to withstand deformation and return to its original shape when released. Additionally, PDMS is transparent within the visible range, rendering it optimal for applications necessitating optical observation of flow or biological phenomena within channels.

PDMS is biocompatible, rendering it an optimal selection for biological and medical applications, including the fabrication of biochemical analysis chips and cell culture devices [48].

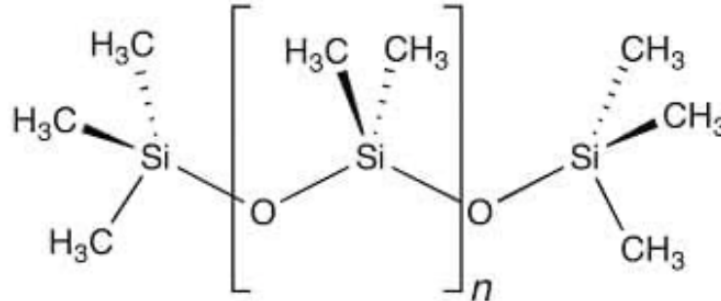


**Figure 7.1:** The chemical structure of PDMS [56]

One of the most prevalent techniques for creating channels in PDMS is SU-8 moulding. This process entails the creation of a mould from SU-8, which is then employed to produce replicas of the platform that contains the microchannels. In contrast to the methodology outlined in Sec. 7.2.1, SU-8 is employed for the fabrication of the mould, rather than the channel walls. Consequently, it will not be present in the final structure.

The process for creating the mould in SU-8 follows that described in Sec. 7.2.1, with the exception of two steps. In contrast to the aforementioned approach, the chip with the nanowires is not employed as the substrate. Instead, a silicon wafer is utilised, and the channel pattern is exposed to light instead of its complementary part, as was done previously.

Once the mould has been manufactured, the subsequent step is to prepare the PDMS, which is then poured over the mould. The initial stage of the process is to prepare the surface of the mould in order to facilitate superior adhesion to the PDMS. A layer of trimethylchlorosilane (TMCS) is deposited on the surface in order to facilitate adhesion. The liquid PDMS, comprising a base and a cross-linking agent in a typical ratio of 10:1, is then poured over the mould in SU-8 and distributed evenly. Subsequently, the PDMS is degassed in a vacuum chamber to remove any residual air bubbles that could potentially compromise the quality of the micro-moulding. After that, the degassed PDMS is cured in an oven at 80 °C for a minimum of 2 h. It should be noted that there is some variation in literature with regard to the temperature and time required for curing. In certain applications, liquid PDMS is permitted to solidify overnight at room temperature.

Following polymerisation, the solidified PDMS is carefully removed from the SU-8 mould, resulting in a precise replication of the micrometric structures it contains. The resulting channels have a rectangular cross-section and, in contrast to the previous technique, are already confined on their sides and at the top. The final step is to bond the base of the platform to a suitable substrate. Typically, glass substrates are employed; however, in this particular application, it will be necessary to bond the PDMS microfluidic platform to the chip containing the nanowires, pads, and metal electrodes, taking care to correctly align the channels with the nanowire arrays.

In order to achieve this, it is possible to modify the surface of the PDMS and the chip, for example by means of an oxygen plasma treatment, in order to render the two contact surfaces hydrophilic and thus ensure a bond and the creation of functional devices without leakages.

Fig. 7.2 schematises the process described. More details on this technique are provided in Sec. 7.3.

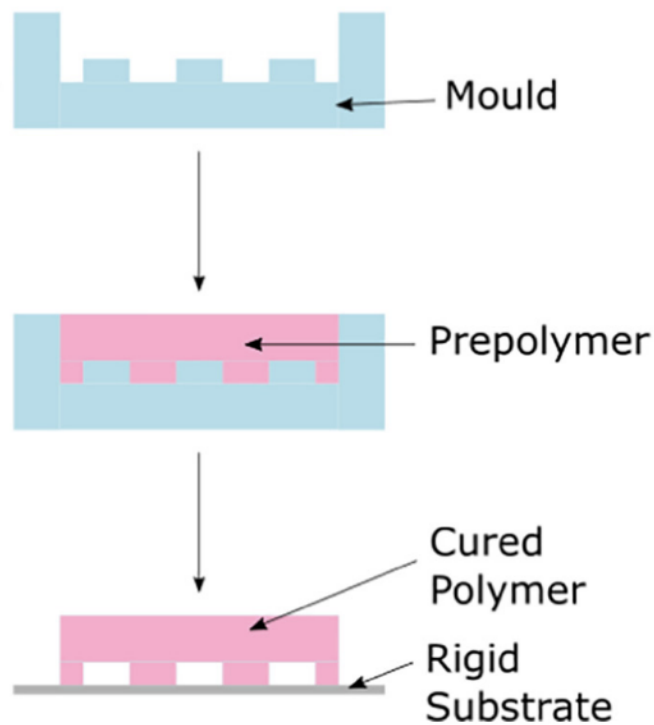


**Figure 7.2:** SU-moulding technique for PDMS [48]

### 7.2.3 Reactivity Testing of SU-8 with Aminolabeled DNA

The two principal techniques that have been identified as the most promising for the fabrication of microfluidic channels have been outlined. It is crucial to emphasise that one of the fundamental criteria for selecting an appropriate fabrication technique is that the selected material should not be reactive with the injected molecules. This is essential to prevent any alteration in the performance of the sensor.

An experiment has been designed with the objective of evaluating the reactivity of SU-8 with Prostate-Specific Antigen (PSA).

The SU-8 photopolymer has epoxy groups in its structure which are chemically very reactive. Epoxy groups, typically characterised by a three-membered ring with one oxygen and two carbon atoms, are known to react readily with nucleophiles such as amine ( $-\text{NH}_2$ ) and thiol ( $-\text{SH}$ ) groups, which are common in biomolecules. In the specific case of PSA, these reactions lead to the formation of covalent bonds with SU-8, which means that part of the PSA molecules are no longer available to bind to the nanowires, which represent the active zone of the device. This results in a loss of useful sample, reducing the amount of detectable PSA and compromising the accuracy of the sensor.

In order to address this issue, an experimental approach was undertaken utilising a technique known as *amino-labelling*. This involves a chemical treatment that is specifically designed to modify the SU-8 surface. This process entails the opening of the epoxy ring through a reaction with molecules containing amine groups, thereby transforming the epoxy groups into primary amines or secondary amines, which are less reactive with biomolecules such as PSA. The principle of this strategy is based on the concept that the introduction of amine groups through amine-labelling reduces the probability of PSA interacting with the SU-8 surface, thereby increasing the availability of PSA for binding to the nanowires.

To test this method, a sample of DNA was modified with a fluorescent marker (Cyanine 3), a common fluorophore for visualisation with a fluorescence microscope. The DNA was incubated on both the amino-labelled and the untreated SU-8 surfaces. SU-8 was subjected to treatment with 100% and 5% aminoethanol.

The data demonstrate a reduction in the reaction between the sample and the treated SU-8, though not a complete elimination. This indicates that although amino-labelling does reduce the number of reactive epoxy groups, their initial concentration is so high that the treatment is not sufficient to neutralise them completely.

The images captured by the fluorescent microscope are presented in Fig. 7.3-Fig. 7.5. In this experiment, amino-labelled SU-8 produced around 4000 counts (Fig. 7.3 and Fig. 7.4), while untreated SU-8 recorded around 6000 counts (Fig. 7.5). The counts represent the number of photons detected by the fluorescence microscope, indicating the intensity of the fluorescence emitted by the sample. This means that the treatment reduced the interaction between the DNA and the SU-8 surface, indicating less reactivity of the epoxy groups. However, SU-8 is still very reactive.

The confirmation of SU-8 reactivity despite the amino-labelling represents a first step towards favouring PDMS as a material for channel construction. This conclusion is confirmed by a second experiment performed, that is described in Sec. 7.2.4.

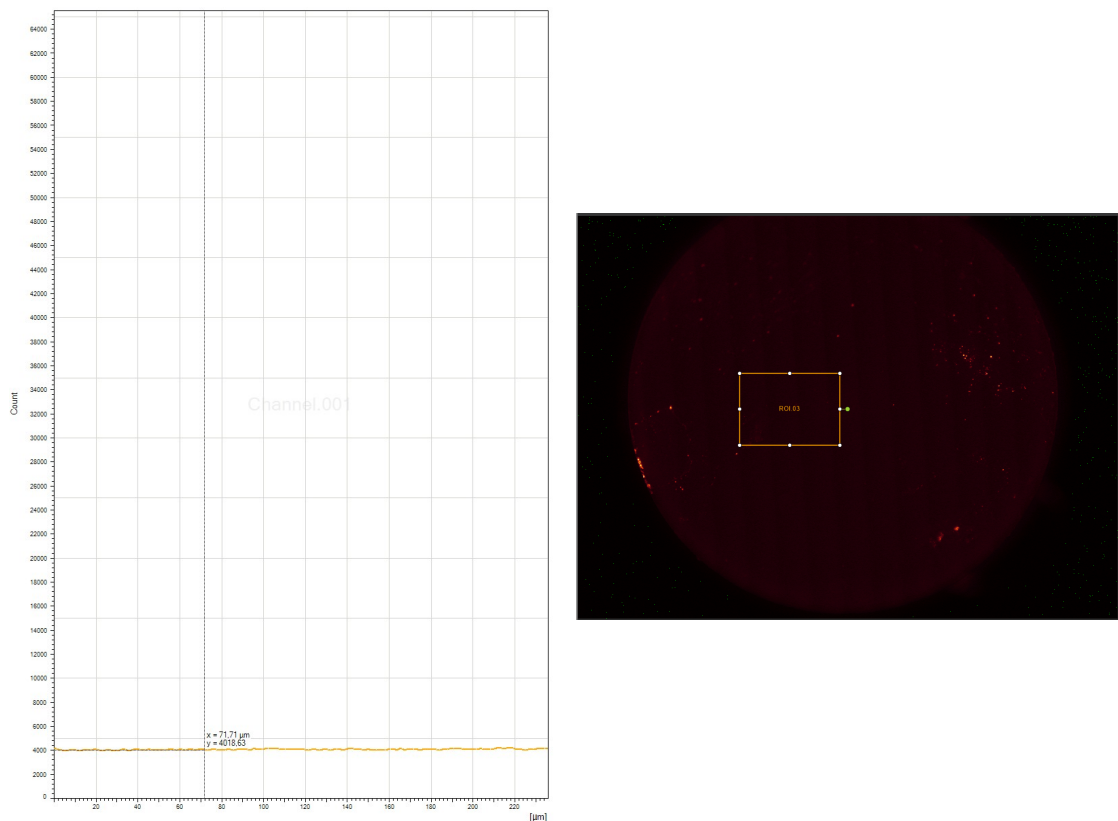


**Figure 7.3:** Fluorescence microscope analysis of the DNA sample on SU8 treated with 5% aminoethanol.

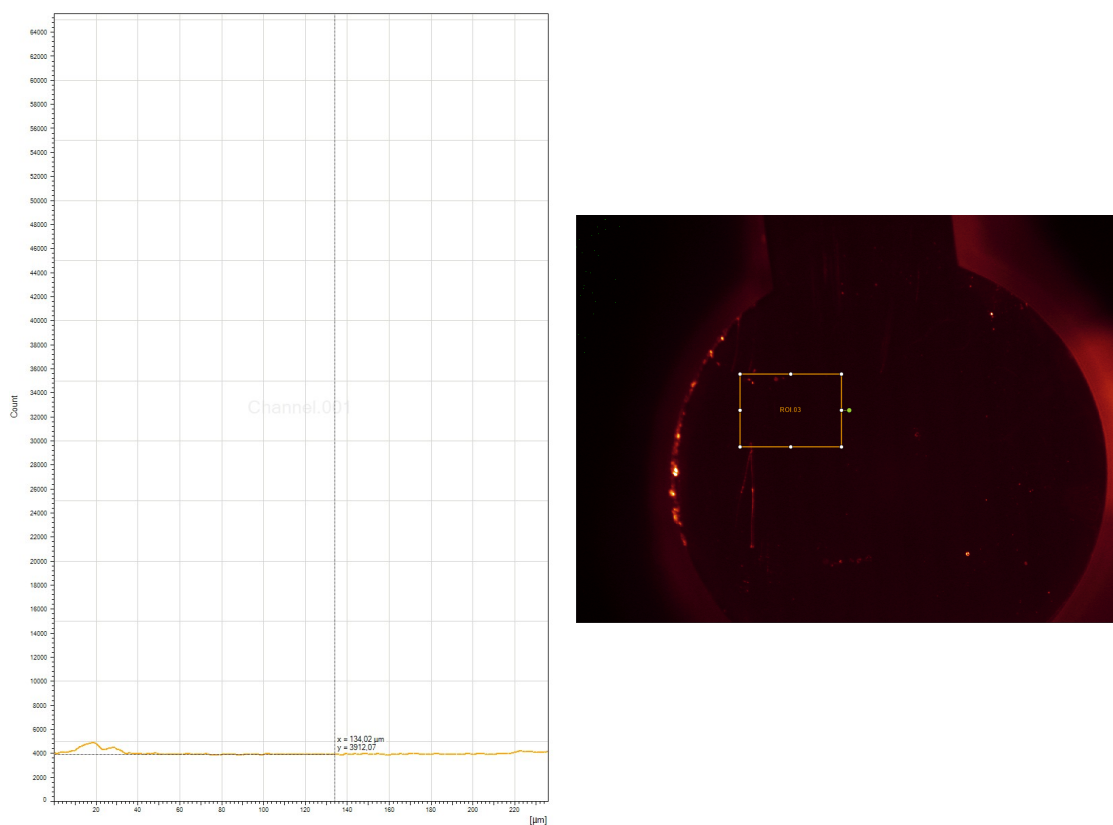


**Figure 7.4:** Fluorescence microscope analysis of the DNA sample on SU8 treated with 100% aminoethanol.

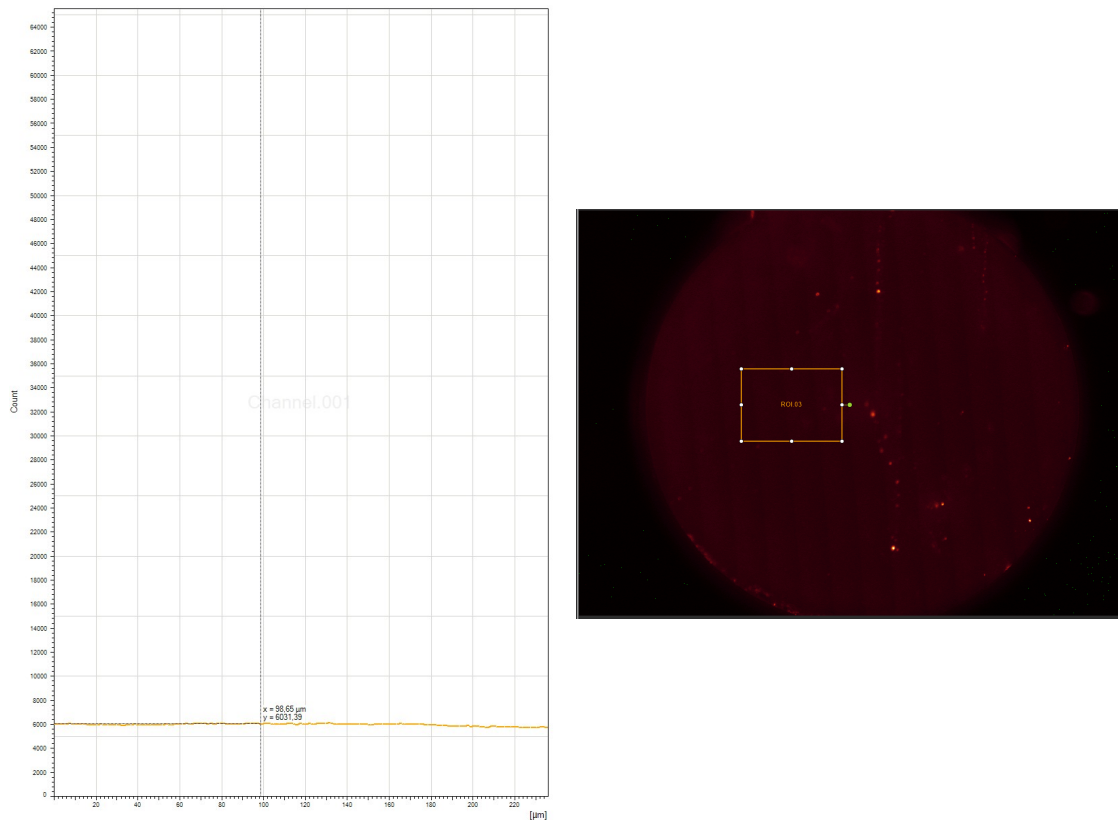


**Figure 7.5:** Fluorescence microscope analysis of the DNA sample on untreated SU-8.

### 7.2.4 Piranha Solution Reactivity Testing

One of the methods used to activate the surface of nanowires as biosensors is the use of piranha solution [57]. This is a highly corrosive and oxidising solution composed of sulphuric acid  $H_2SO_4$  and hydrogen peroxide  $H_2O_2$  in a 3:1 ratio. Once deposited on the surface of the silicon nanowires, it results in the formation of a substantial number of hydroxyl groups (-OH), rendering the surface highly hydrophilic and chemically active, thereby facilitating subsequent functionalisation. It should be noted that the Piranha solution is not the only method for activating nanowires. There are other viable alternatives, such as oxygen plasma treatment. Nevertheless, it is useful to establish whether this technique is compatible with the selected fabrication method.

To assess the stability of the materials used in the fabrication of the microchannels, a sample of PDMS and a silicon chip with an SU-8 mould were subjected to a

10-minute immersion in a Piranha solution. Furthermore, in order to guarantee the compatibility of any prospective microfluidic instrumentation, such as syringes and reagent injection tubes, with this treatment, these components were also subjected to the same immersion process. The beaker was positioned on a thermal stirrer, which provided a combined effect of stirring and high temperature throughout the duration of the test. Upon completion of the test, the samples were retrieved from the beaker and subjected to analysis. While the PDMS and instrumentation exhibited no visible damage and demonstrated stability in solution over the specified time interval, the SU-8 was found to have incurred corrosion, as illustrated in Fig. 7.6. It can be concluded that SU-8 is incompatible with the Piranha solution, as it will suffer degradation and loss of structural integrity. Therefore, if the Piranha solution is to be used to activate the surface of silicon nanowires, SU-8 should be avoided.



**Figure 7.6:** Effect of piranha solution on SU-8

### **7.2.5 Final Fabrication Method Selection**

Table 7.1 summarises the main manufacturing methods and comments on their eligibility for the designed device.

As evidenced by the analysis conducted, SU-8 moulding for PDMS is definitely the best technique for this application.

Method	Pros and Cons
3D printing	Although a valid technique, it introduces complications with regard to bonding to the chip containing the biosensors.
Paper-based microfluidics	It is not a suitable option for the purposes of the project, as it is challenging to integrate with the nanowire chip.
ESCARGOT	Integration with the nanowire chip is challenging due to the necessity of embedding the chip in the PDMS during the channeling process.
PMMA platforms	The methodology is applicable to the device under development; however, the necessary instrumentation, such as lasers to create the inlets and outlets of the channels, is not readily available in our laboratory.
SU-8 channels	The SU-8 reacts with the sample molecules, thereby affecting the final performance of the device. Furthermore, it has been demonstrated that the photoresist is not stable in the Piranha solution. The advantage of this approach is that the channels are constructed directly on the biosensor chip, thus simplifying both the alignment and bonding processes.
PDMS channels (SU-8 moulding)	This technique is particularly appreciated for its ease of use and the ability to achieve complex geometries with precision, due to the excellent resolution offered by SU-8 as a photoresist. Moreover, PDMS is transparent within the visible range, exhibits biocompatibility, and is stable in the Piranha solution. The process is optimised in that the same mould can be employed on multiple occasions to produce PDMS platforms. During the alignment and bonding phases, it is of the utmost importance to exercise caution and precision.

**Table 7.1:** Comparison of different fabrication methods for the microfluidic platform

### 7.3 Detailed PDMS Fabrication Process with SU-8 Moulding

Once the fabrication method has been selected, a detailed description of the process flow for the realisation of the microfluidic channels can be provided (Fig. 7.7).

Step	Process description	Cross-section after process
01	<b>Substrate: Si</b> <i>Substrate Pretreat</i> Machine : <i>Tepla300 (Z11)</i> Prog.05 – Time : 7'	
02	<i>Photolith PR coat</i> Machine : <i>Sawatec LSM250 (Z13)</i> PR : <i>SU-8 (Gersteltec – GM1075) - 75µm</i>	
03	<i>Relaxation + Softbake</i> Machine : <i>Sawatec HP200 (Z13)</i>	
04	<i>Photolith exposure</i> Machine : <i>MLA150-2 (Z16)</i>	
05	<i>Post exposure bake + Relaxation</i> Machine : <i>Sawatec HP200 (Z13)</i>	
06	<i>Development</i> <i>Solvent bench (Z13)</i> Product : <i>PGMA – two separate bath</i>	
07	<i>Rinse + dry</i> Product : <i>Isopropanol (for rinse)</i>	
08	<i>Hard bake (optional)</i> Machine : <i>Sawatec HP200 (Z13)</i>	
09	<i>Surface conditioning</i> Machine : <i>Fume hood + wet bench desiccator (Z12)</i> Product : <i>TMCS</i>	

<p><b>10</b></p>	<p><i>Mixing + Degassing</i>  Machine : Mixer THINKY (Z12) +  Desiccator (Z12)  Product : Sylgard 184 silicone base +  Sylgard curing agent (10:1)</p>	
<p><b>11</b></p>	<p><i>Pouring</i>  Material : PDMS</p>	
<p><b>12</b></p>	<p><i>Baking (curing)</i>  Machine : VWR - VENTI Line Oven  (Z12)  Temp : 80°C</p>	
<p><b>13</b></p>	<p><i>Alignment + Demolding + Access ports  by punching</i>  Machine : PDMS Hole Puncher (Z12)</p>	
<p><b>14</b></p>	<p><i>Surface activation + bonding</i>  Machine : Plasma HARRICK (Z12)  Substrate : SOI wafer with Si-nanowires  anchored between the NiSi pads and  metal contacts (Ti/Au) fabricated in  steps 01→08</p>	

**Figure 7.7:** Process flow for SU-8 moulding and PDMS

The initial step of the process is to clean the silicon wafer on which the SU-8 mould will be fabricated. This is done in order to remove any contaminants that could potentially impede the adhesion of the photoresist to the substrate. The wafer is subjected to a cleaning process involving the use of acetone, followed by a rinsing stage utilising deionised water. Subsequently, the wafer is dried using a nitrogen gun.

The photoresist is deposited by spin-coating. Two distinct types of photoresist are selected on the basis of their respective suitability to the desired SU-8 thicknesses. The selected photoresists are Kayaku 3050 and Kayaku 3025. The former is chosen

to produce ticker moulds, e.g. 40  $\mu\text{m}$  and 80  $\mu\text{m}$ , while the latter is suitable to test moulds with a smaller thickness, such as 20  $\mu\text{m}$ .

The Sawatec LSM-200 manual spin coater is used to apply the photoresist. Once the vacuum has been activated, the photoresist is poured directly from the bottle onto the wafer that has been placed on the chuck. The plate is then set to spin at a speed that has been pre-set according to the recipe that has been previously determined. The Table 7.2, Table 7.3 and Table 7.4 show the recipes for spin-coating in the case of Kayaku 3050 and Kayaku 3025, for the three thicknesses indicated.

Time (s)	Speed (rpm)
5	500
5	500
27	3160
40	3160
1	4160
1	3160
5	3160
32	0

**Table 7.2:** spin-coating recipe - Kayaku 3025 for 20  $\mu\text{m}$

Time (s)	Speed (rpm)
5	500
5	500
22	2680
40	2680
1	3680
1	2680
5	2680
27	0

**Table 7.3:** spin-coating recipe - Kayaku 3050 for 40  $\mu\text{m}$

Time (s)	Speed (rpm)
5	500
5	500
9	1400
40	1400
1	2400
1	1400
5	1400
14	0

**Table 7.4:** spin-coating recipe - Kayaku 3050 for 80  $\mu\text{m}$

After spin-coating, the wafer is placed on a hot plate (HP-401-Z) at 95 °C for soft-baking over a variable time period, that increases with the thickness, as described in the process specifications.

	20 $\mu\text{m}$	40 $\mu\text{m}$	80 $\mu\text{m}$
Time (s)	600	900	2100

**Table 7.5:** soft-bake time - SU-8 (Kayaku)

The next step is to expose with *MLA150* at a wavelength of 375 nm. The dose set varies according to the thickness: for example, for an SU-8 layer of 80  $\mu\text{m}$  the dose used is 800 mJ/cm<sup>2</sup>, for 40  $\mu\text{m}$  the dose used is 550 mJ/cm<sup>2</sup>, for 20 microm 450 mJ/cm<sup>2</sup>. It should be noted that the values indicated are merely indicative, as they are dependent on the specific machine utilised and are the result of a series of trials, starting from the dose recommended in the specifications. These trials have led to the adjustment of this value in order to achieve a satisfactory result. It can be observed that during the exposure phase, the exposed areas undergo a cross-linking process which renders the SU-8 insoluble in the developing solvents, thus creating the desired structure. In the process of creating a mould, the exposed areas serve to delineate the outline of the channels that are to be produced.

The Fig. 7.8 shows an example of a file given as input to *MLA150* to create repeated channel moulds on a wafer. They are 9 mm long and range in width from 800  $\mu\text{m}$  to 2,700  $\mu\text{m}$ .

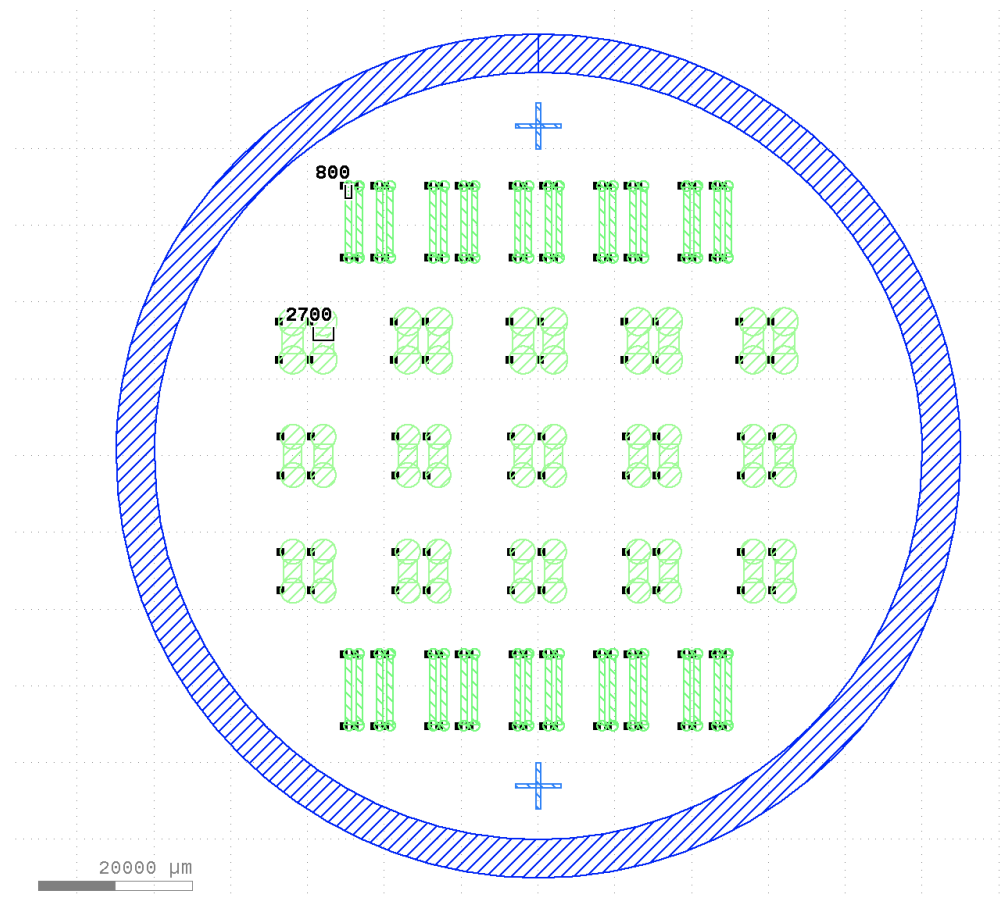


**Figure 7.8:** .GDS file for *MLA150* exposure (SU-8 mould)

Following exposure, a post-exposure bake is conducted to complete the cross-linking process and guarantee that the exposed areas are fully cross-linked. As with soft-bake, the *HP-401-Z* hot plate is used. Regardless of thickness, the wafer is heated to 65 °C for 60 s and 95 °C for 200 s.

Following a minimum of 10 minutes of relaxation in the wafer storage box to stabilise the photoresist, the development phase may then commence. As previously stated, SU-8 is developed by immersing the wafer in PGMEA, followed by rinsing with IPA until no residual whiteness is observed, indicating the complete development of the photoresist.

At this point, the SU-8 mould is prepared for the next stage of the process, which is the creation of the microfluidic channels. The Fig. 7.9 shows an electron microscope detail of the fabricated mould.

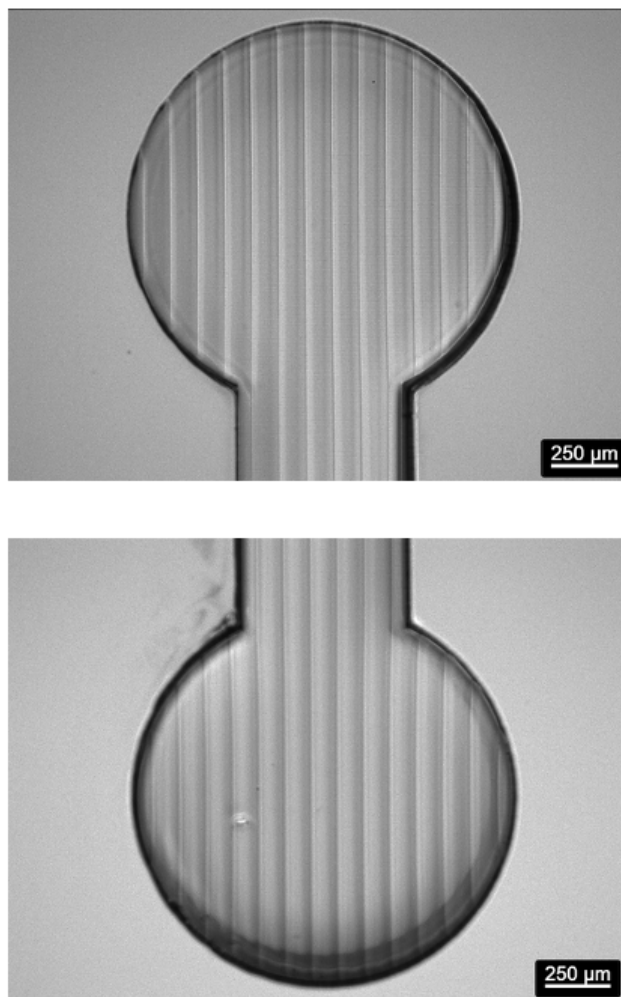


**Figure 7.9:** SU-8 mould details

Prior to the application of the PDMS, it is essential to ensure that the surface of the mould has been properly prepared. This is done by evaporating TMCS (chlorotrimethylsilane, 33014 from Sigma) for 20 min in a desiccator containing the wafer. TMCS is deposited on the surface of the mould, forming a passivation layer.

The initial stage of the process involves the mixing of PDMS with a suitable curing agent, with a ratio of 10:1 being optimal for this purpose. This ratio is commonly used in microfluidics and provides an optimal balance between the elasticity and mechanical strength of the PDMS, ensuring that the material is sufficiently malleable to facilitate handling and drilling for the creation of inlets

and outlets, while maintaining sufficient rigidity to ensure mechanical stability and the ability to retain the shape defined by the mould once cross-linked. To coat the entire wafer, 4 g crosslinker (Sylgard hardener) and 40 g PDMS (Sylgard 184 silicone base) are poured into a beaker. These two components are mixed using a mechanical mixer (THINKY Mixer) which operates a mixing phase at 2,000 rpm for 1 min and a defoaming phase at 2,200 rpm for 2 min. The mixture is then placed in a desiccator for 10-15 min to remove any air bubbles.

Once the preparation process is complete, the PDMS is transferred to the mould and placed within a Petri dish coated with aluminium foil. This serves to contain the polymer over the wafer. It is possible that air bubbles may form during this phase of the operation. These should be removed manually with a pipette or by using a nitrogen gun. The subsequent stage of the process is to place the Petri dish in an oven at 80 °C for at least 2 h. During this time, the PDMS undergoes a cross-linking process: the siloxane groups (-Si-O-Si-) within the PDMS react with the curing agent, forming a stable three-dimensional elastic network that solidifies the material. This cross-linking process makes the PDMS flexible but rigid enough to maintain the channels structure.

The cured PDMS is meticulously extracted from the mould using a cutting tool, taking care to avoid damaging the microfluidic structures or the wafer with the mould, thus ensuring its reuse. Once the individual platforms have been cut, the holes for the inlets and outlets of each channel are created. This is achieved through a punch pen with an appropriate diameter for the insertion of tubes or needles. In particular, the diameter of the punch should be slightly smaller than that of the component to be connected to the inlet and outlet, in order to prevent leakage from the two holes and to exploit the ability of PDMS to deform slightly in order to create an optimal seal. In this particular case, a punch of 1.2 mm has been chosen to fit correctly into a tube of 1.6 mm diameter.

Once these steps are completed, the platform is protected with tape to prevent dust or other contaminants from clogging the channels.

The chip with integrated nanowires and electrodes, along with the microfluidic platform, have been fabricated and are now ready for bonding. The next step is to join them together in order to achieve optimal integration. This step is not straightforward and will be discussed in the next chapter (Chapter 8).

## Chapter 8

# Bonding Techniques for Microfluidic Integration

### 8.1 Oxygen Plasma

Oxygen plasma treatment is a widely used technique to activate material surfaces, enhancing their chemical reactivity and promoting adhesion between different layers in various fabrication processes [58]. For example, this treatment is typically applied to silicon (Si), silicon oxide ( $\text{SiO}_2$ ), glass, and PDMS.

Chemically, oxygen plasma is an ionized gas containing various species such as oxygen atoms, positive ions, electrons, and free radicals.

The material to be treated is placed in a chamber where vacuum and plasma are created. The reactive oxygen species bombard the surface of the substrate, removing organic impurities and other contaminants present, such as solvent or photoresist residues. The oxygen radicals oxidize these organic materials, transforming them into volatile products like carbon dioxide ( $\text{CO}_2$ ) and water ( $\text{H}_2\text{O}$ ) [59], which are easily evacuated from the vacuum system. This process leaves the substrate surface clean, preparing it for subsequent deposition or bonding steps.

In addition to cleaning, plasma treatment chemically modifies the surface without affecting bulk properties. Oxygenated functional groups, such as hydroxyl groups (-OH), are introduced. Exposure of the material to oxygen plasma thus leads to the formation of a more oxidized surface layer, highly hydrophilic due to the presence of hydroxyl groups, increasing the wettability and reactivity of the surface.

These modifications are not permanent. In fact, after a certain period of time, the

surface energy starts to decrease: on one hand, the polar groups on the polymer surface tend to migrate toward the bulk, reducing their exposure on the surface; on the other hand, small polymer chain segments move and relocate within the polymer matrix [60]. For this reason, when plasma treatment is used to bond two surfaces, it is important to bring them into contact immediately after exposure. To maintain the modifications made by plasma treatment for a longer period, it is recommended to keep the surface in an aqueous environment. Additionally, it has been reported that the hydrophilicity of the treated surface lasts longer in dry air compared to humid air [61].

### **8.1.1 Oxygen Plasma Bonding for PDMS**

PDMS, like many polymers, is characterized by low surface energy and poor adhesive properties. It is a hydrophobic material, with a contact angle that varies approximately between  $100^\circ\text{C}$  and  $110^\circ\text{C}$  depending on its chemical composition [62].

When PDMS is exposed to oxygen plasma, its surface undergoes a significant transformation: the plasma breaks the  $\text{Si} - \text{CH}_3$  bonds in the PDMS structure, replacing the methyl groups ( $-\text{CH}_3$ ) with hydroxyl groups ( $-\text{OH}$ ), creating a surface similar to silica ( $-\text{SiO}_2$ ) [63] [64]. This transformation makes the PDMS surface hydrophilic and much more chemically reactive.

At the same time, the surface of the element to which the PDMS will be bonded must also be treated. In this case, the PDMS platform needs to adhere to a silicon chip.

Silicon substrate treated with oxygen plasma becomes rich in silanol groups ( $-\text{Si}-\text{OH}$ ). When the treated surfaces of silicon and PDMS are brought into contact, the  $-\text{Si}-\text{OH}$  groups present on both materials undergo a condensation reaction, forming strong siloxane covalent bonds ( $-\text{Si}-\text{O}-\text{Si}-$ ). This chemical reaction creates a robust and stable bond between silicon and PDMS.

The same mechanism occurs with other materials, such as glass surfaces, as illustrated in Fig. 8.1. During this research, a glass slide was often used as a substrate to perform pre-tests, to avoid wasting the chips containing the biosensors.

### **8.1.2 Integration with Metallic Electrodes**

Despite the effectiveness of oxygen plasma treatment for bonding PDMS to silicon, silicon oxide, and glass surfaces, which has been widely tested, the integration of PDMS with a substrate containing gold electrodes—like the designed device—is not straightforward. Gold is an inert metal that does not activate after plasma

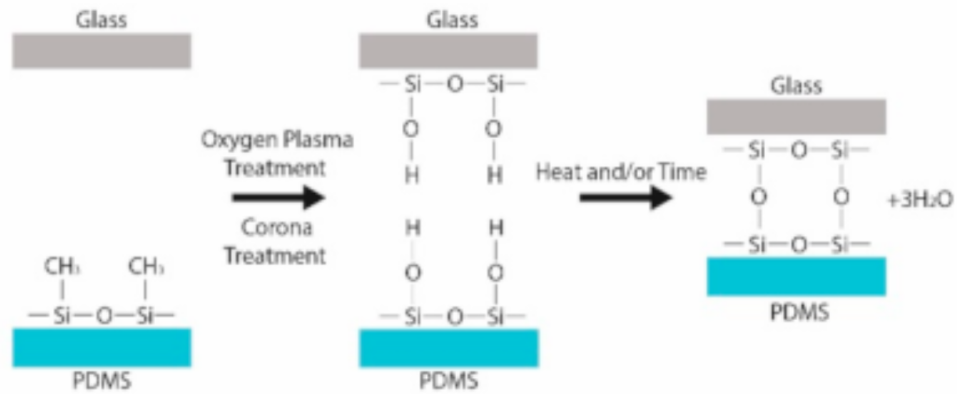


**Figure 8.1:**  $O_2$  plasma treatment for PDMS-glass bonding [64]

treatment. Therefore, in a device like the one designed and fabricated in this thesis, only the chip surface not covered by metal electrodes will be activated and form bonds with PDMS. This makes the bonding process more critical because, in general, the bond between the microfluidic platform and the chip with the biosensors will only form in the regions where gold has not been deposited. Consequently, much attention was paid to the bonding process, to research the best process parameters that would result in a leak-proof device despite the challenges posed by the presence of metal electrodes.

In [65], a study is conducted on the integration of PDMS to a substrate containing gold electrodes, just like the case at hand. The authors studied how the width of the gold electrodes affects the pressure leakage resistance.

As expected, the wider the electrodes, the lower the critical fluid pressure, beyond which leaks are recorded. The trend is shown in Fig. 8.2. This result is reasonable because, the wider the electrodes, the smaller the activated surface capable of forming strong bonds with PDMS.

In parallel, the researchers performed finite element simulations to understand the mechanism behind the leaks. The simulations suggested that the mechanical deformation of PDMS under pressure creates a gap between PDMS and gold, which increases with the electrode width. Devices with narrower gold connectors deform the PDMS less, reducing the gap and therefore the likelihood of leaks [65].

To address this issue, on one hand, research was conducted to optimize process parameters for traditional oxygen plasma treatment, as described in Sec. 8.1.3; on the other hand, a new bonding technique based on GPTMS and APTMS was

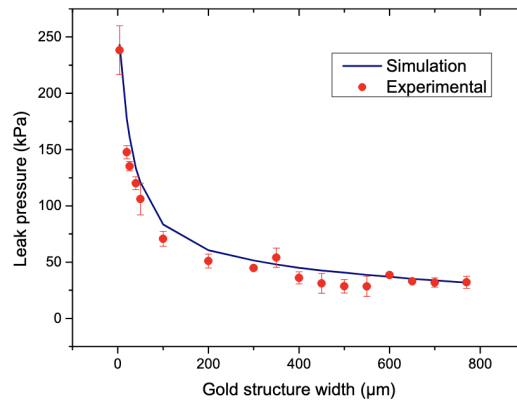


**Figure 8.2:** Leakage test for PDMS integrated with gold electrodes [65]

developed, as illustrated in Sec. 8.2.

### 8.1.3 Plasma Activation Equipment

The detailed process that allowed the use of traditional oxygen plasma treatment to bond PDMS and the chip with nanowires, plasma, and gold electrodes, ensuring the absence of leaks, is now illustrated.

Before proceeding with bonding between the chip with the biosensors and PDMS, it is necessary to activate the nanowire surface with oxygen plasma. This step is crucial because after bonding the channels to the chip, it will no longer be possible to expose the nanowires to subsequent treatments. Surface activation is carried out using the Tepla300 machine, following a predefined recipe with a plasma exposure time of 10 min. With the set recipe, a plasma is generated at a power of 500 W and a frequency of 2.45 GHz.

Immediately afterward, the PDMS is activated using the Plasma HARRICK system. This phase requires the optimization of parameters such as plasma power, internal chamber pressure, and exposure time to ensure a strong and durable bond. Several tests were conducted to identify the most effective parameter combination. After various attempts, an optimized recipe for PDMS was found, with the following parameters:

- Plasma power: 29 W
- Internal pressure: 550 mTorr-600 mTorr
- Exposure time: 50 s-60 s

Once both surfaces have been treated with plasma, the alignment and bonding phase is performed immediately. This phase requires great precision because the nanowires must be fully covered by the microfluidic channels. The alignment is done manually with the help of an optical microscope. It is important to proceed immediately after plasma treatment to prevent the surfaces from losing their hydrophilicity. A light manual pressure is applied to facilitate contact between the surfaces, without applying too much force to avoid collapsing the PDMS channels. After bonding, the system is placed in an oven at 80 °C for about 30 min. This step has an important chemical-physical function. Heating promotes the condensation reaction between the hydroxyl (-OH) groups present on the activated surfaces, leading to the formation of siloxane bonds (-Si-O-Si-), which create a stable and durable covalent connection between the two surfaces.

#### **8.1.4 Leakage Test Results**

Fig. 8.3 shows the correct integration of the microfluidic platform with the chip containing biosensors and electrodes. This represents a key result for the research developed.

## **8.2 Silanization Bonding with GPTMS/APTMS**

As mentioned earlier, another bonding method, based on silanization, was tested in parallel.

The silanization protocol with GPTMS and APTMS is a technique used to achieve durable and stable chemical bonds between different surfaces, especially in the field of microfabrication, where the quality of adhesion between materials is critical for the integrity of devices.

This method combines surface activation through oxygen plasma with subsequent chemical silanization to strengthen the bond between silicon, glass, or polymer surfaces, such as PDMS.

GPTMS and APTMS are bifunctional silane molecules, featuring specific functional groups at both ends of their chemical structures. GPTMS has an epoxide group on one end and three methoxysilane groups  $-\text{Si}(\text{OCH}_3)_3$  on the other. The methoxysilane groups are highly reactive toward surfaces rich in hydroxyl groups (-OH), such as those activated by oxygen plasma. The epoxide group is a reactive cyclic ring that can open to chemically react with other nucleophilic species, such as the amine groups present in APTMS.

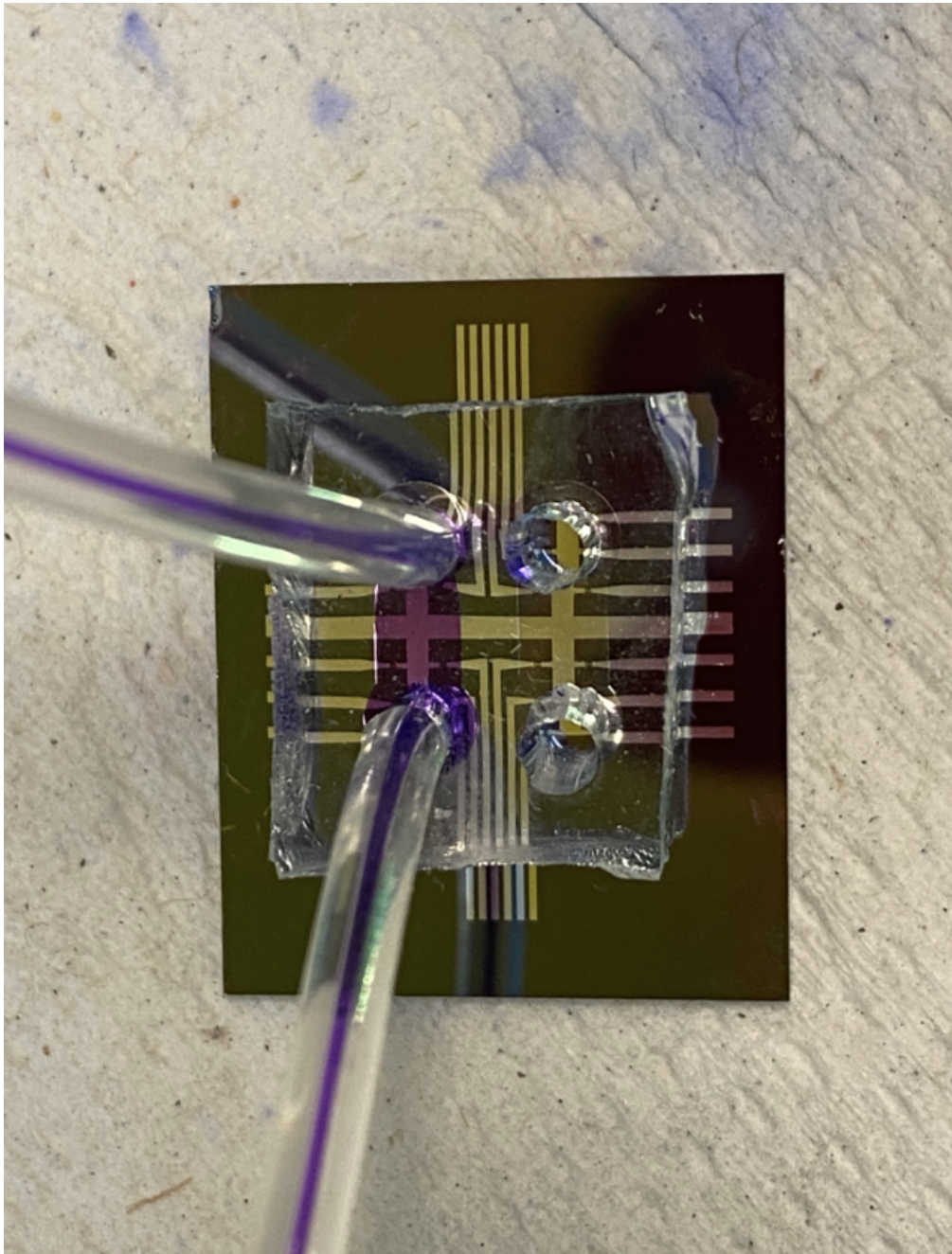


**Figure 8.3:** Final biosensing device (silicon nanowire chip, NiSi pads, gold electrodes, microfluidic platform). There is no leakage, as all components are perfectly integrated.

APTMS, on the other hand, has three methoxysilane groups similar to those of GPTMS but contains an amine group ( $-NH_2$ ) at the opposite end. This amine group is highly reactive towards electrophilic groups like the epoxide group in GPTMS, facilitating the formation of covalent chemical bonds between the two surfaces treated with the two silanes.

The bond that is desired to be formed is shown in Fig. 8.4.

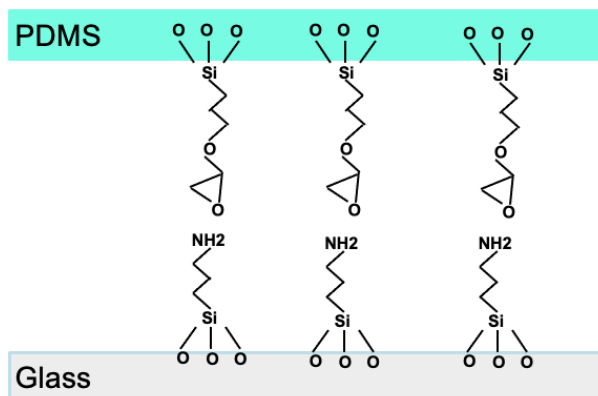


**Figure 8.4:** PDMS-glass bonding

Tests were conducted with PDMS and glass to verify the effectiveness of the method developed.

The process begins with the activation of the glass and PDMS surfaces, which are exposed to oxygen plasma. This step induces the formation of hydroxyl groups ( $-OH$ ). The Plasma HARRICK machine is used for PDMS, while Tepla300 is used for glass. Two PDMS samples and two glass slides are tested.

GPTMS is first applied to one of the two activated PDMS surfaces and one of the two activated glass surfaces. The process takes place in a desiccator, where a bottle with GPTMS and the two substrates to be tested are placed. At this stage, the methoxysilane groups of GPTMS undergo hydrolysis, transforming the methoxysilane groups into silanol groups ( $-Si-OH$ ). They react with the hydroxyl groups present on the plasma-activated surface, forming siloxane bonds ( $-Si-O-Si-$ ) that anchor the GPTMS molecule to the substrate surface. At this stage, the epoxide part of the GPTMS molecule remains intact, ready to chemically interact with the second surface treated with APTMS.

In parallel, the second glass and PDMS surfaces are treated with APTMS. Again, the components are placed in a desiccator, which is then placed in an oven at a temperature of about  $80^\circ C$ . The methoxysilane groups of APTMS undergo

a hydrolysis reaction, generating silanol groups that react with the hydroxyl groups present on the activated surface, forming siloxane bonds. The fundamental difference between GPTMS and APTMS is that in this case, the amine group of APTMS remains free.

Once both processes are completed, the two surfaces, one with GPTMS and the other with APTMS, are brought into contact. The amine group of APTMS reacts with the epoxide group of GPTMS through a nucleophilic addition reaction. In this process, the amine group attacks the epoxide group, opening the epoxide ring and forming a covalent bond between the two surfaces.

After applying GPTMS and APTMS, the surfaces can be placed in an oven at a high temperature, around 80 °C, for a controlled period of time. This step accelerates the condensation process of the bonds.

The process was then repeated for four additional components, comprising two glass and two PDMS samples. The temperature effect was also employed in the case of GPTMS.

### 8.2.1 Leakage Test

After the process described in Sec. 8.2, leakage tests were performed. As shown in Fig. 8.5, no leaks were detected in one case (Glass treated with APTMS-PDMS treated with GPTMS), while in the other case (PDMS treated with APTMS-Glass treated with GPTMS), leaks were observed from the channel.



**Figure 8.5:** Leakage test

The leakage test was also performed by injecting piranha solution. The bond remained stable even after injecting piranha solution and leaving it in the channel

for about 5 min, demonstrating the effectiveness of this bond. The same result was also obtained for a PDMS platform bonded to glass via oxygen plasma alone, thanks to the optimized parameters described in Sec. 8.1.3. Thus, the bonding process using GPTMS and APTMS can be considered valid.

Further tests can be performed to verify its effectiveness on the chip with metal electrodes. In this case, when bonding PDMS to the chip using only oxygen plasma, it is demonstrated that the bond is not strong enough to withstand piranha solution. Therefore, an additional test could be conducted to verify the effectiveness of the new method for bonding PDMS to a chip with electrodes, and to test its strength in the presence of piranha solution. This would provide an advantage, as the surface of the nanowires could be activated with piranha solution instead of oxygen plasma treatment before their functionalization. This would allow the device to be reused even after a long time, when the plasma effect is no longer present on the nanowire surface, and these cannot be treated again because they are already covered by the PDMS platform.

## Chapter 9

# Detection of Prostate Specific Antigen (PSA)

### 9.1 Protocollo di rilevamento del PSA

The device has been evaluated for its ability to detect the Prostate-Specific Antigen (PSA). In order to test the device's ability to detect these molecules, even at low concentrations, a protocol has been developed, inspired by [57].

It should be noted that prior to bonding to the microfluidic platform, the nanowires must be activated with an oxygen plasma treatment of 10 min duration with a power of 500 W. The machine employed is the *Tepla300*. It generates O<sub>2</sub> plasma within a quartz primary vacuum chamber at a frequency of 2.45 GHz.

Following the bonding of the PDMS component, leakage tests are conducted with deionised (DI) water. The results confirm that the microfluidic platform is securely attached to the chip with no leakage. Subsequently, the PSA-specific antibody is introduced into the channels via micropipettes. The instrument is then inserted directly into the inlet of each of the two channels on the device. A syringe is inserted into a tube connected to the opposite end, and pressure is applied to ensure that the fluid is evenly distributed throughout the channel, thus ensuring interaction with all the nanowires. The aforementioned process is then repeated for both channels within the device.

Finally, the chip is covered with *Parafilm* to prevent evaporation and maintain a stable environment during the incubation period, which takes place overnight at

room temperature. This step allows the antibody to immobilise on the surface of the nanowires, as described in Chapter 2.

At the end of the incubation period, the device is washed to remove any unbound antibody. The washing process consists of a sequential rinsing with phosphate buffered saline (PBS), followed by a rinse with DI water, repeated three times. For the washing step, two tubes are connected to the inlet and outlet of each channel and the washing fluids are injected using a syringe with a capacity of 1 mL. The washing procedure takes about 10 min in total, as each injection has to be carried out carefully to avoid the pressure of the liquid damaging the nanowires or the antibody binding.

As pointed out by [57], the use of microfluidics makes it possible not only to reduce the duration of washing time, but also to limit the waste of solutions.

It is essential to ensure that the interior of the channels is adequately dried, as residual DI water could potentially introduce errors in the measurements. The presence of this layer could create a voltage gap compared to the characteristic obtained prior to incubation. In order to facilitate the drying process, an empty syringe is connected to the tubes inserted into the inlet and outlet of each channel. It is crucial to ensure that the injection of air into the channel is conducted with the utmost care and precision, in order to prevent any potential damage to the system.

Once the device is completely dry, the I-V characteristics of nanowires can be measured using the same procedure and measuring apparatus described in Chapter 6. The electrical characteristics of nanowires are recorded, including the measurement of the voltage gap between the two minima of the hysteresis curve, which is the critical parameter for this biosensing application. This data is used as a reference for subsequent measurements taken after antigen incubation (antigen uptake), allowing the voltage gap to be compared to assess PSA antigen binding.

After completing the initial measurement of the nanowires with antibody, the antigen (PSA peptide - concentration: 1 mg/mL) is incubated following a similar procedure to that used for the antibody.

Two different incubation protocols have been tested:

- incubation overnight at room temperature
- incubation overnight in a refrigerator at 4 °C

The second method has proven to be more effective.

Upon completion, the device is rinsed once more with PBS and DI water, with the objective of removing any residual unbound antigen. Following the drying step, the characteristics of individual nanowires are reassessed. It is fundamental that the position of each biosensor be indicated in order to facilitate comparison between the measurements taken following the incubation of the antibody and those taken after antigen uptake. It should be noted that each nanowire may exhibit variations in physical structure, electrical properties and surface functionalisation. Furthermore, the inherent variability of nanowires, which can be influenced by factors such as process variations or material characteristics, necessitates the avoidance of generic comparisons between curves belonging to distinct biosensors.

The expected outcome of the measurement procedure is a shift in the curve, resulting in a reduction in the measured voltage gap following the incubation of the antibody alone. Indeed, as detailed in Chapter 2, in case of antigen binding to the biosensor, a change in its electrical response is expected.

The outcomes of the study and the comparison between the two antigen incubation protocols are presented in the Sec. 9.2.

## Summary of Main Steps

1. The surface of the nanowires is activated through oxygen plasma treatment for a duration of 10 min at a power of W. This is followed by bonding with the microfluidic platform.
2. The antibody solution is then injected using micropipettes, with uniform distribution in the channel achieved through the application of syringe-induced pressure.
3. The samples are sealed with *Parafilm* and incubated overnight at room temperature.
4. The channels are washed with PBS and DI water in several steps (approximately three washes with PBS and three rinses with DI water), followed by drying.
5. The I-V characteristics of nanowires to be tested are measured in order to establish the reference values for the voltage gap.
6. The antigen solution is injected using micropipettes, ensuring uniform distribution by applying pressure induced by a syringe.
7. The samples are sealed with *Parafilm* and incubated overnight in a refrigerator at 4 °C.

8. The channels are rinsed with PBS and DI water and then dried in several steps.
9. The I-V characteristics are measured for the same nanowires that were tested in step 5.
10. A comparison of voltage gaps is employed to ascertain the extent of antigen binding.

## **9.2 Analysis of Experimental Data**

Two distinct chips were subjected to examination in accordance with the methodology delineated in Sec. 9.1. For each chip, a total of three to six nanowires were subjected to testing. It is important to note that a number of the nanowires were unsuitable for testing due to accidental damage incurred during the fabrication process. These occurrences are common in the production of such delicate nanostructures and are often the result of unavoidable factors inherent to the fabrication techniques. Nevertheless, this does not constitute a significant issue, as the primary goal is to assess the overall efficacy of the manufactured technology and the success of the designed fabrication process. Testing a representative subset of nanowires is sufficient to evaluate the success of the device and the fabrication method as a whole, making it unnecessary to test every individual nanowire.

For each nanowire under test, two to five repeated measurements were conducted. The mean value and standard deviation were calculated for each set of data.

The graphs in Fig. 9.1 and Fig. 9.2 illustrate the data that was processed subsequent to the testing of the first chip, in which the overnight incubation of the antigen at room temperature was evaluated.

It is observed that some nanowires (NW3, NW4, NW5) demonstrate the expected behaviour, exhibiting a reduction in the voltage gap derived from the I-V characteristic. In one specific instance (NW2), the value of the voltage gap remains largely unchanged. This suggests that antigen uptake has not occurred. Finally, in the cases represented by the nanowires NW1 and NW6, an increase in the voltage gap is observed. It is indicative of non-specific absorption. In this case, half of the biosensors tested functioned correctly, demonstrating the effectiveness of the technology used and the processes implemented. The second device yielded even more favourable results, which will be discussed below.

The graph in Fig. 9.1 presents the mean value of the voltage gap measurements for each nanowire, along with the corresponding standard deviation. The plot in

Fig. 9.2 shown the individual repeated measurements taken for each nanowire. It should be noted that the measurement apparatus employed is the same as that described in Chapter 6.

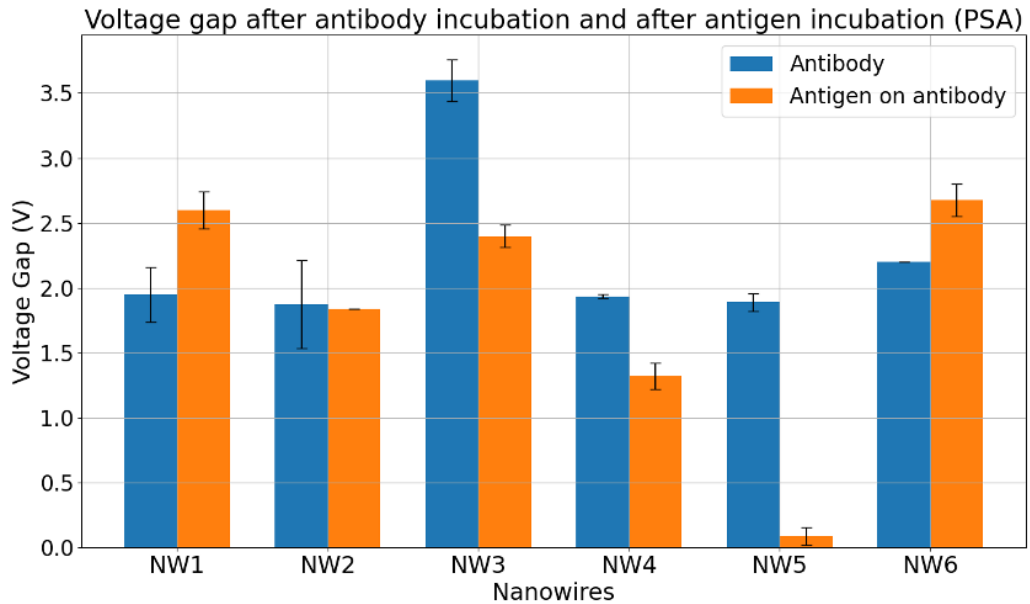


**Figure 9.1:** Voltage gap after antibody incubation and after antigen incubation for six nanowires in the first device (mean value and standard deviation)

The graphs in Fig. 9.3 and Fig. 9.4 illustrate the data obtained from the second chip, which was subjected to an overnight incubation of the antigen at a temperature of 4°C. The graph in Fig. 9.3 shows the mean value of the voltage gap measurements taken for each nanowire, along with the corresponding standard deviation. The graph in Fig. 9.4 depicts the individual, repeated measurements taken for each nanowire.

In this scenario, all three nanowires tested, which belong to the same microfluidic channel, yielded the desired outcome. In all cases tested, the biosensors were able to detect the presence of the PSA molecule, thereby demonstrating the effectiveness of the technology developed for this purpose.

Moreover, it can be concluded that the incubation of the antigen at 4°C is more effective than incubation at room temperature. It could be proposed that the low temperature facilitates the uptake of the antigen.

The utilisation of microfluidics facilitated the deposition of sample solutions in a more rapid and efficacious manner, while concurrently maintaining the optimal

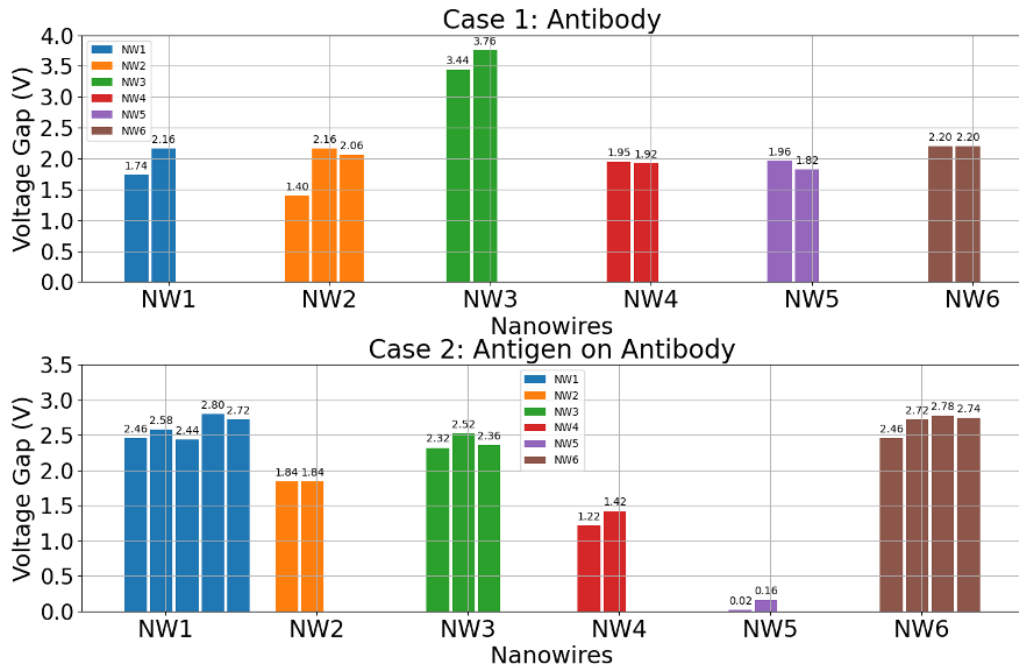


**Figure 9.2:** Repeated measurements of the voltage gap for six nanowires in the first device

humidity conditions throughout the incubation phase. Moreover, the integration of gold electrodes did not affect the memristive behaviour, thanks to the low resistance introduced. Indeed, in all nine cases tested, both devices exhibited a hysteresis curve and a voltage gap.

Future work could focus on further optimizing the incubation process, as well as investigating the effects of varying antigen concentrations to improve detection sensitivity.

The following figures (Fig. 9.5-Fig. 9.13) illustrate the curves obtained for the nine nanowires that were tested. For each nanowire, one of the I-V characteristics obtained after incubating the antibody alone is presented, with a comparison to one of the I-V characteristics obtained after incubating the antigen. Plots in Fig. 9.5-Fig. 9.10 are referred to the first device under test.

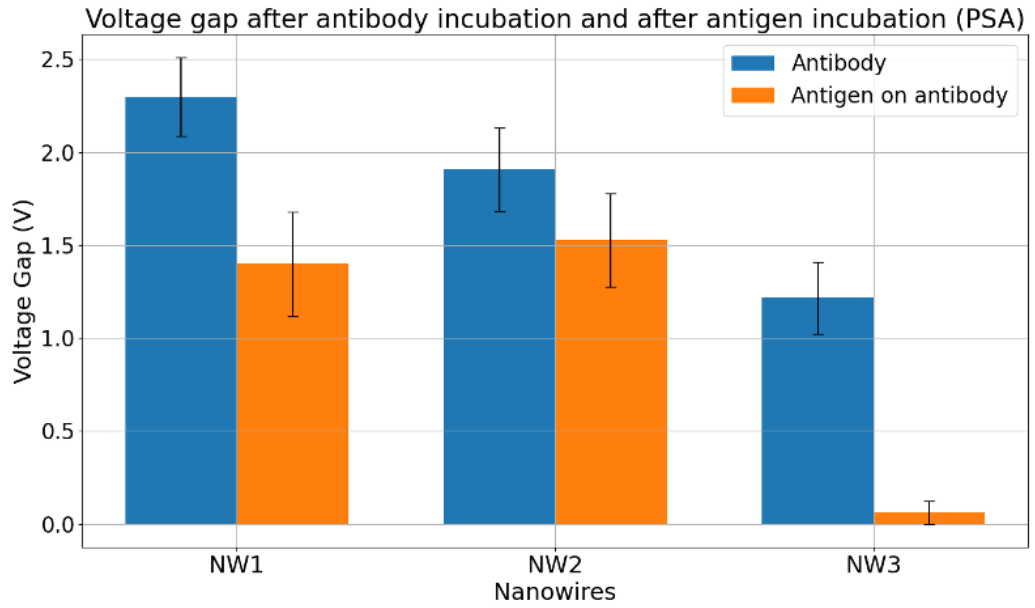


**Figure 9.3:** Voltage gap after antibody incubation and after antigen incubation for three nanowires in the second device (mean value and standard deviation)

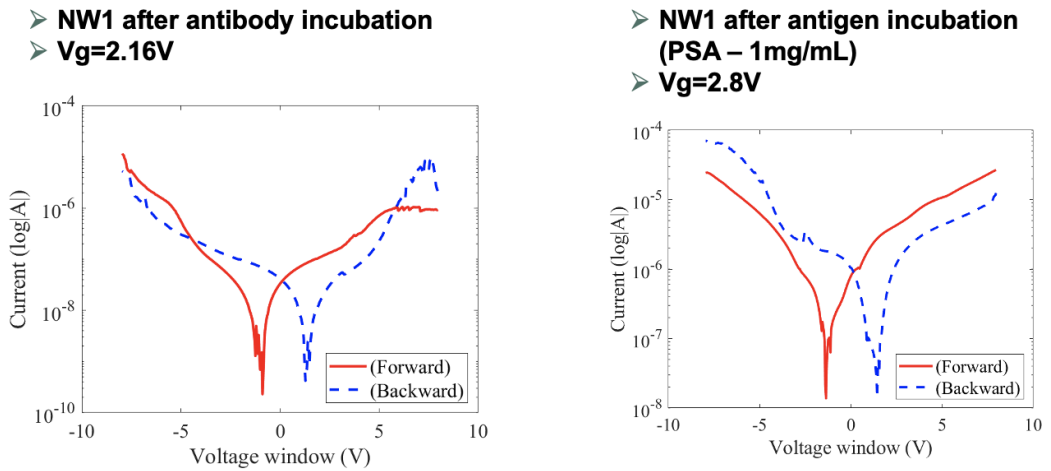


**Figure 9.5:** I-V characteristic of NW1 (first device) before and after antigen incubation

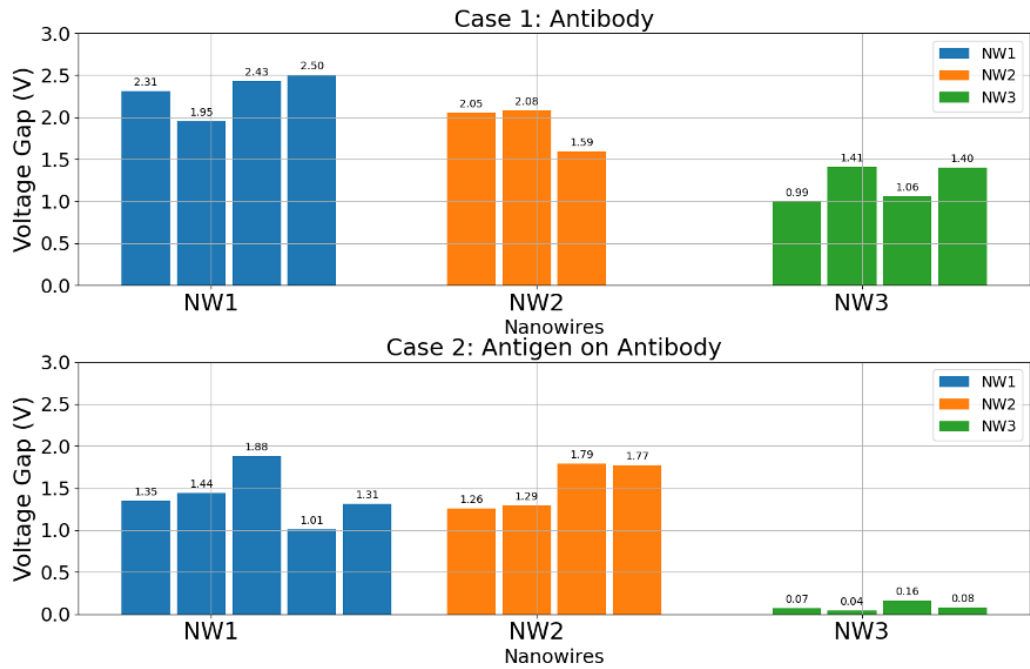
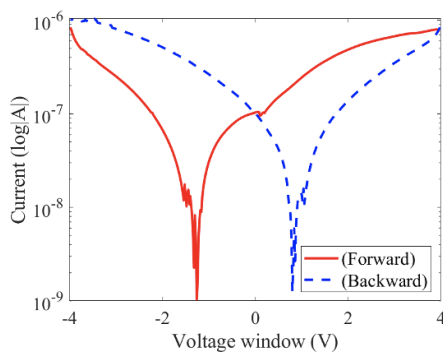


**Figure 9.4:** Repeated measurements of the voltage gap for three nanowires in the second device

➤ **NW2 after antibody incubation**  
 ➤ **V<sub>g</sub>=2.06V**



➤ **NW2 after antigen incubation (PSA – 1mg/mL)**  
 ➤ **V<sub>g</sub>=1.84V**

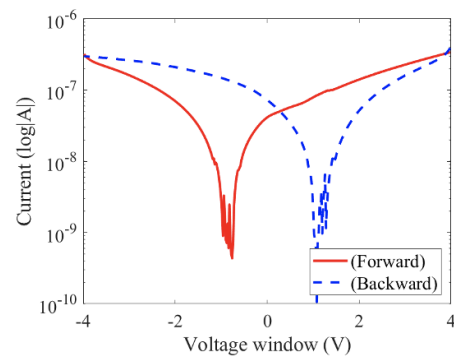
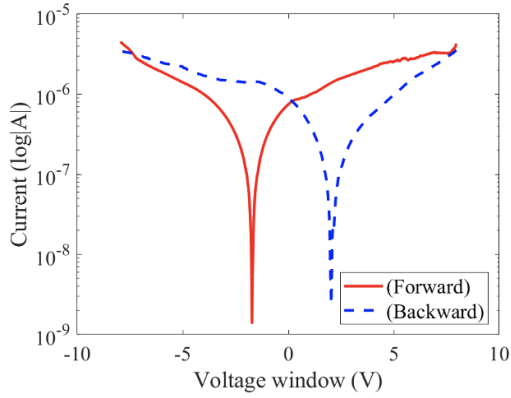


**Figure 9.6:** I-V characteristic of NW2 (first device) before and after antigen incubation

- NW3 after antibody incubation
- $V_g=3.76V$



- NW3 after antigen incubation (PSA – 1mg/mL)
- $V_g=2.36V$

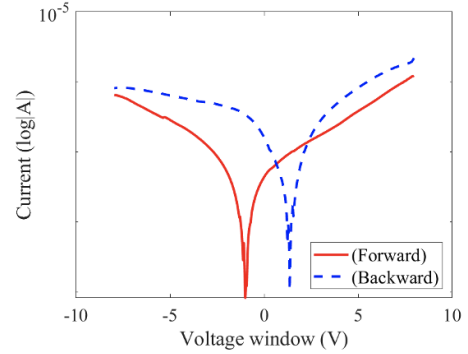
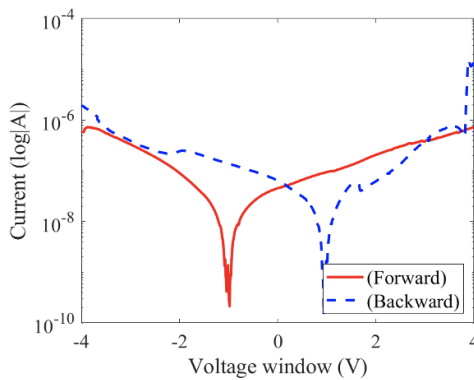


Figure 9.7: I-V characteristic of NW3 (first device) before and after antigen incubation

- NW4 after antibody incubation
- $V_g=1.92V$



- NW4 after antigen incubation (PSA – 1mg/mL)
- $V_g=1.42V$

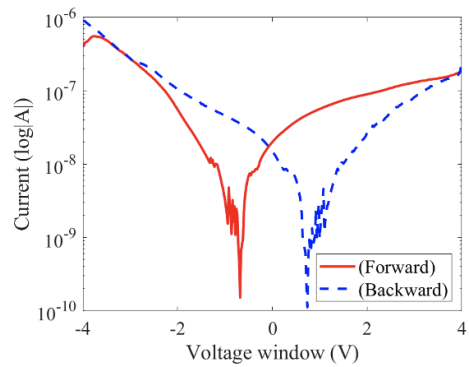
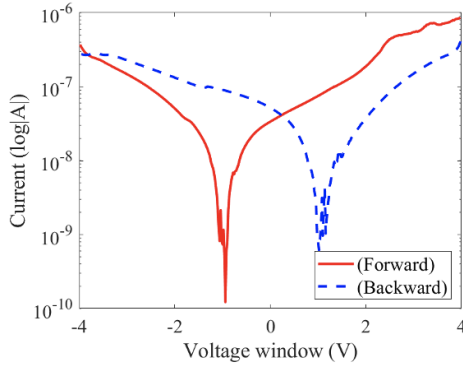
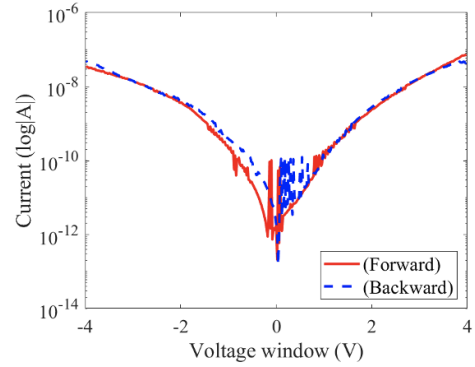


Figure 9.8: I-V characteristic of NW4 (first device) before and after antigen incubation

- **NW5 after antibody incubation**
- **$V_g=1.96V$**

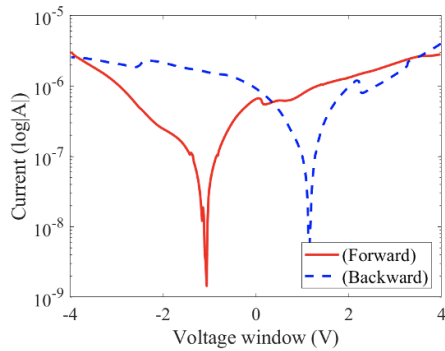


- **NW5 after antigen incubation (PSA – 1mg/mL)**
- **$V_g=0.02V$**



**Figure 9.9:** I-V characteristic of NW5 (first device) before and after antigen incubation

- **NW6 after antibody incubation**
- **$V_g=2.2V$**



- **NW6 after antigen incubation (PSA – 1mg/mL)**
- **$V_g=2.72V$**

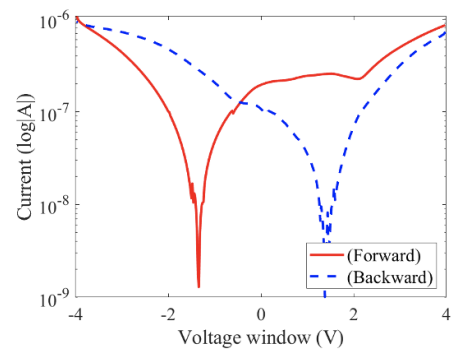
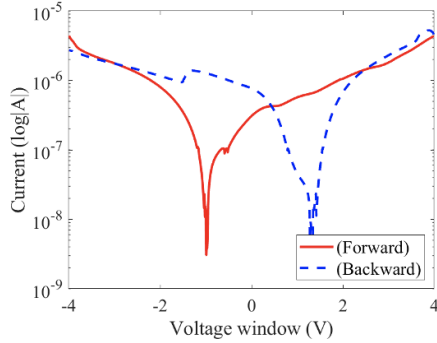


**Figure 9.10:** I-V characteristic of NW6 (first device) before and after antigen incubation

Some of the curves obtained for the I-V characteristics of the three nanowires under test are shown for the second device tested. They are shown in Fig. 9.11- Fig. 9.13.

- NW1 after antibody incubation
- $V_g=2.31V$



- NW1 after antigen incubation (PSA – 1mg/mL)
- $V_g=1.35V$

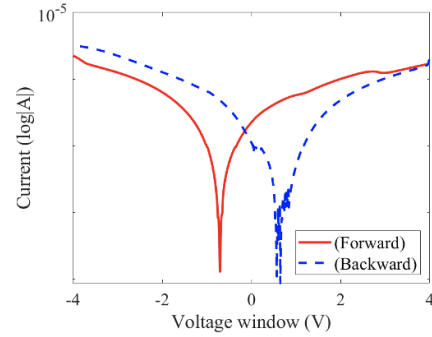
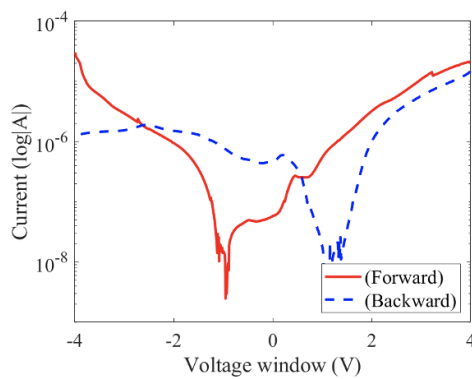


Figure 9.11: I-V characteristic of NW1 (second device) before and after antigen incubation

- NW2 after antibody incubation
- $V_g=2.05V$



- NW2 after antigen incubation (PSA – 1mg/mL)
- $V_g=1.26V$

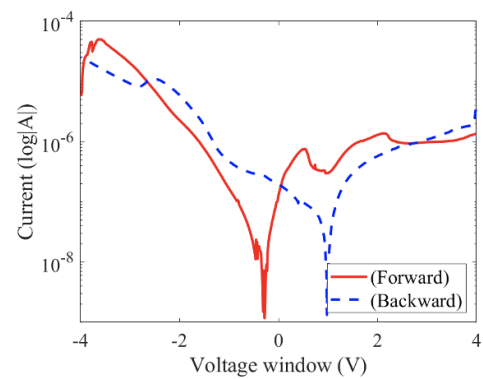
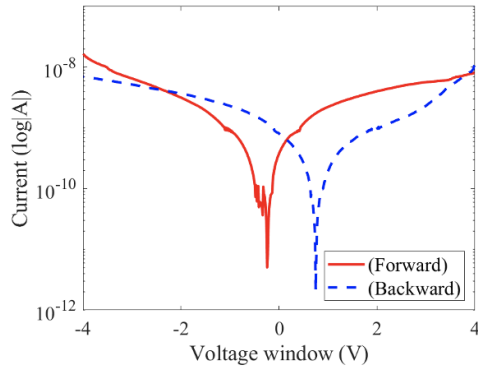
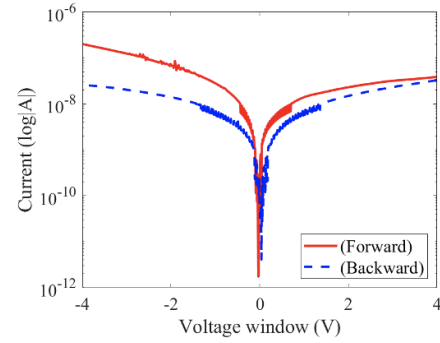


Figure 9.12: I-V characteristic of NW2 (second device) before and after antigen incubation

- NW3 after antibody incubation
- $V_g=0.99V$



- NW3 after antigen incubation (PSA – 1mg/mL)
- $V_g=0.07V$



**Figure 9.13:** I-V characteristic of NW3 (second device) before and after antigen incubation

## Chapter 10

# Conclusions and Future Perspectives

The research work presented in this Thesis has significantly contributed to the advancement of biosensing technologies, focusing on the development of an innovative platform that combines silicon nanowires with memristive properties, metallic electrodes, and a microfluidic component. This integrated solution was specifically designed and optimized for the detection of biomarkers such as Prostate-Specific Antigen (PSA), a key indicator for early diagnosis of prostate cancer. However, the platform's potential extends far beyond this specific application, paving the way for a wide range of biomedical applications.

One of the main achievements of this work was demonstrating that memristive nanowires, combined with metallic electrodes designed to optimize electrical performance and a microfluidic platform that effectively manages the sample, can accurately and reliably detect biomarkers without the need for chemical labeling (label-free). This approach exploits the change in the electrical properties of the nanowires induced by antigenic interaction, which translates into a measurable alteration of the current-voltage (I-V) curve. Specifically, PSA detection occurs through a variation in the memristive behavior of the device, evidenced by a shift of the hysteresis observed in the I-V graph. This represents a significant advancement over traditional biosensing techniques, as the device not only detects the presence of the biomarker but also integrates data processing directly into the system's memory, effectively realizing the concept of "in-memory sensing."

The integration of the microfluidic platform represented a further advancement

over traditional solutions based on drop-casting techniques. Microfluidics allows for precise and controlled manipulation of fluids, minimizing reagent waste and improving the reproducibility of measurements. This aspect is crucial for point-of-care (PoC) applications, where efficiency and accuracy in handling small sample volumes are critical. Thanks to the design of specific microchannels, the system can evenly distribute the biological sample over the active sensor area, ensuring that biochemical reactions occur under optimal humidity conditions. This could reduce the risk of measurement errors, which is essential for a device intended for clinical use.

From a fabrication standpoint, the developed platform required the use of advanced technologies, such as photolithography, the lift-off technique for electrode deposition, and SU8-moulding for the PDMS structure. Advanced bonding techniques were also necessary for integrating the microfluidic platform with the chip containing the nanowires and electrodes. In particular, the use of oxygen plasma ensured a stable and leak-free integration between the PDMS platform and the silicon chip, providing the device with enough robustness to withstand repeated operations. A second bonding method, based on the combined action of oxygen plasma and silanization with GPTMS and APTMS, was also tested, showing promise. Further investigation will be necessary, including bonding tests between PDMS and the chip, in addition to PDMS and glass, as already performed.

Another strength of this work was the in-depth study of the challenges and issues encountered during the fabrication and integration of the platform. All fabrication processes used were the result of many trials and studies, aiming to optimize the process parameters for the device's success. For each phase, it can be stated that we now have the recipe with the parameters necessary to fabricate a functional, leak-free device capable of detecting target molecules.

The experimental results obtained during the development of this platform demonstrated the device's ability to detect PSA at clinically relevant concentrations, confirming that the proposed solution is promising for monitoring this biomarker. Additionally, the modular design of the device suggests that it can be easily adapted for the detection of other biomarkers, thus expanding its potential applications in diagnostics. In the future, new tests could be conducted, varying the concentration of molecules and testing new samples.

Despite the positive results, the work carried out in this Thesis paves the way to further developments and optimizations. In particular, it can be improved in terms of the device's sensitivity and specificity, especially in clinical settings where maximum accuracy is required to avoid false positives or negatives. A potential future development concerns the implementation of more advanced functionalization

strategies for the nanowires, with the aim of improving affinity and selectivity for specific biomarkers.

Another important area of research could be the integration of a multiplexing system that allows for the simultaneous detection of multiple biomarkers, thus increasing the diagnostic efficacy of the device and expanding its use in different biomedical applications. This goal could be achieved, for example, through the integration of valves. Pneumatic valves or rotary valves show particular promise [66].

Finally, it would be beneficial to move toward integrating the chip into a printed circuit board (PCB) [67].

The platform developed in this thesis not only represents a promising step forward in the field of biosensing technologies but also opens the door to innovative applications that could significantly impact diagnostics and point-of-care solutions in the future.

# Bibliography

- [1] EPFL Bio/CMOS Interfaces Laboratory. *In-Memory Sensing: Computing done in the sensors, not close to the sensor*. <https://www.epfl.ch/labs/bci/in-memory-sensing-computing-done-in-the-sensors-not-close-to-the-sensor/>. Accessed: 2024-10-15 (cit. on p. 1).
- [2] Daniele Ielmini and H.-S. Philip Wong. «In-memory computing with resistive switching devices». In: *Nature Electronics* 1 (2018), pp. 333–343 (cit. on p. 2).
- [3] EPFL Bio/CMOS Interfaces Laboratory. *BCI Ongoing Research*. <https://www.epfl.ch/labs/bci/bci-ongoing-research/>. Accessed: 2024-10-15 (cit. on p. 2).
- [4] ARAMIS. *Onco-PoK2 a MEM-TDM-nanosensor for imatinib*. <https://www.aramis.admin.ch/Texte/?ProjectID=53593>. Accessed: 2024-10-15 (cit. on p. 2).
- [5] L. O. Chua. «Memristor - the missing circuit element». In: *IEEE Transactions on Circuit Theory* CT-18.5 (1971), pp. 507–519 (cit. on pp. 4, 5).
- [6] D. B. Strukov, G. S. Snider, D. R. Stewart, and R. S. Williams. «The missing memristor found». In: *Nature* 453 (2008), pp. 80–83 (cit. on pp. 4, 7).
- [7] L. O. Chua and S. M. Kang. «Memristive devices and systems». In: *Proceedings of the IEEE* 64.2 (1976), pp. 209–223 (cit. on pp. 5–7).
- [8] *Design and development of memristor-based RRAM - Scientific Figure on ResearchGate*. [https://www.researchgate.net/figure/Hysteresis-curve-of-memristor-with-the-sinusoidal-input-voltage-4\\_fig2\\_330877788](https://www.researchgate.net/figure/Hysteresis-curve-of-memristor-with-the-sinusoidal-input-voltage-4_fig2_330877788). Accessed: 17 Oct 2024 (cit. on p. 6).
- [9] Bernard Widrow. «An Adaptive "Adaline" Neuron Using Chemical "Memistors"». In: *Stanford Electronics Laboratories Technical Report* 1553-2 (1960) (cit. on p. 6).
- [10] R. S. Williams. «How we found the missing memristor». In: *IEEE Spectrum* 45.12 (2008), pp. 28–35 (cit. on p. 7).

- [11] S. H. Jo, T. Chang, I. Ebong, B. B. Bhadviya, P. Mazumder, and W. Lu. «Nanoscale memristor device as synapse in neuromorphic systems». In: *Nano Letters* 10.4 (2010), pp. 1297–1301 (cit. on p. 7).
- [12] Qiangfei Xia et al. «Memristor-CMOS Hybrid Integrated Circuits for Reconfigurable Logic». In: *Nano Letters* 9.10 (2009), pp. 3640–3645 (cit. on p. 7).
- [13] R. Homsy, N. Al-Azzam, B. Mohammad, and A. Alazzam. «Memristive Biosensors for Cancer Biomarkers Detection: A Review». In: *IEEE Access* 11 (2023), pp. 19347–19363 (cit. on p. 8).
- [14] D. Strukov, G. S. Snider, D. Stewart, and R. S. Williams. «The missing memristor found». In: *Nature* 453 (2008), pp. 80–83 (cit. on p. 8).
- [15] I. Tzouvadaki, S. Carrara, and G. De Micheli. «Modeling Memristive Biosensors». In: *IEEE Biomedical Circuits and Systems Conference*. 2015 (cit. on p. 8).
- [16] D. Strukov, G. S. Snider, D. Stewart, and R. S. Williams. «The missing memristor found». In: *Nature* 453 (2008), pp. 80–83 (cit. on p. 8).
- [17] K. Bhardwaj, A. Golparvar, J. Chen, G. L. Barbruni, and S. Carrara. «New Insights Into the I/V Hysteretic Characteristics of Memristive Biosensors». In: *IEEE Sensors Letters* 7.9 (2023), p. 1500904 (cit. on p. 8).
- [18] I. Tzouvadaki, C. Parrozzani, A. Gallotta, G. De Micheli, and S. Carrara. «Memristive Biosensors for PSA-IgM Detection». In: *BioNanoScience* 5.4 (Dec. 2015), pp. 189–195 (cit. on p. 8).
- [19] I. Tzouvadaki, F. Puppo, S. Carrara, and G. De Micheli. «Multi-Panel, On-Single-Chip Memristive Biosensing». In: *IEEE Sensors Journal* 19.14 (2019), pp. 5769–5778 (cit. on p. 8).
- [20] I. Tzouvadaki, N. Madaboosi, R. R. G. Soares, V. Chu, J. P. Conde, G. De Micheli, and S. Carrara. «Bio-Functionalization Study of Memristive-Biosensors for Early Detection of Prostate Cancer». In: *2015 11th Conference on Ph.D. Research in Microelectronics and Electronics (PRIME)*. Glasgow, United Kingdom: IEEE, 2015, pp. 17–20 (cit. on p. 9).
- [21] Abuduwaili Tuoheti, Simone Aiassa, Francesca Criscuolo, Francesca Stradolini, Ioulia Tzouvadaki, Sandro Carrara, and Danilo Demarchi. «New Approach for Making Standard the Development of Biosensing Devices by a Modular Multi-Purpose Design». In: *IEEE Transactions on NanoBioscience* 19.3 (July 2020), pp. 339–346 (cit. on p. 10).
- [22] Ioulia Tzouvadaki, Nima Aliakbarinodehi, Giovanni De Micheli, and Sandro Carrara. «Memristive Aptasensors for Theranostics». In: (n.d.) (cit. on p. 11).

- [23] Junrui Chen, Kapil Bhardwaj, and Sandro Carrara. «Modelling Non-Filamentary Memristive Behavior of Quasi-1D Silicon Nanowire». In: (n.d.) (cit. on pp. 11, 12).
- [24] Ioulia Tzouvadaki, Francesca Puppo, Marie-Agnes Doucey, Giovanni De Micheli, and Sandro Carrara. «Computational Study on the Electrical Behavior of Silicon Nanowire Memristive Biosensors». In: *IEEE Sensors Journal* 15.11 (Nov. 2015), pp. 6208–6217 (cit. on pp. 12, 13).
- [25] Janina Bahnemann and Alexander Grünberger, eds. *Microfluidics in Biotechnology*. Vol. 179. Advances in Biochemical Engineering/Biotechnology. Cham: Springer International Publishing, 2022 (cit. on pp. 14, 18, 19).
- [26] Xiangchun Xuan and Dongqing Li. «Analysis of electrokinetic flow in microfluidic networks». In: *Journal of Micromechanics and Microengineering* 14.2 (2004), p. 290 (cit. on p. 15).
- [27] Danilo Demarchi. *Introduction to microfluidics*. Slides PDF. Introduction to MEMS & BioMEMS, Politecnico di Torino. 2023 (cit. on pp. 15, 18).
- [28] Todd M. Squires and Stephen R. Quake. «Microfluidics: Fluid physics at the nanoliter scale». In: *Reviews of Modern Physics* 77.3 (2005), pp. 977–1026. DOI: 10.1103/RevModPhys.77.977 (cit. on pp. 15, 16).
- [29] Todd A Duncombe, Augusto M Tentori, and Amy E Herr. «Microfluidics: reframing biological enquiry». In: *Nature Reviews Molecular Cell Biology* 16 (2015), pp. 554–567 (cit. on p. 16).
- [30] Rintu Banerjee, S.P. Jeevan Kumar, Ninad Mehendale, Surajbhan Sevda, and Vijay Kumar Garlapati. «Intervention of microfluidics in biofuel and bioenergy sectors: Technological considerations and future prospects». In: *Renewable and Sustainable Energy Reviews* 101 (2019), pp. 548–558 (cit. on p. 16).
- [31] Vincent Rocher. *Flow Rate, Pressure and Resistance in Microfluidics*. <https://blog.darwin-microfluidics.com/the-theory-behind-flow-rate-pressure-and-resistance-in-microfluidics/>. Accessed: 2024-09-10. 2023 (cit. on pp. 17, 55).
- [32] Masindi Sekhwama, Kelvin Mpofu, Sivarasu Sudesh, and Patience Mthunzi-Kufa. «Integration of Microfluidic Chips with Biosensors». In: *Discover Applied Sciences* 6.9 (2024), p. 458 (cit. on p. 18).
- [33] Pierre Bodénès, Hsin-Yi Wang, Ta-Hui Lee, Hsiao-Yin Chen, and Chien-Yuan Wang. «Microfluidic techniques for enhancing biofuel and biorefinery industry based on microalgae». In: *Biotechnology for Biofuels* 12.1 (2019), p. 33 (cit. on p. 18).

- [34] Jue Wang et al. «Continuous fabrication of microcapsules with controllable metal covered nanoparticle arrays using droplet microfluidics for localized surface plasmon resonance». In: *Lab on a Chip* 17.11 (2017), pp. 1970–1979 (cit. on p. 18).
- [35] Tariq Jamshaid et al. «Magnetic particles: from preparation to lab-on-a-chip, biosensors, microsystems and microfluidics applications». In: *TrAC Trends in Analytical Chemistry* 79 (2016), pp. 344–362 (cit. on p. 18).
- [36] Janina Bahnemann, Frank Stahl, and Thomas Scheper. «Spezielle labortechnische Reaktoren: lab-on-a-chip». In: *Springer Spektrum*. Berlin: Springer Spektrum, 2020, pp. 1391–1418 (cit. on p. 18).
- [37] Pratechee Padma Behera, Natish Kumar, Monika Kumari, Sumit Kumar, Pranab Kumar Mondal, and Ravi Kumar Arun. «Integrated microfluidic devices for point-of-care detection of bio-analytes and disease». In: *Sensors & Diagnostics* 2 (2023), pp. 1437–1459 (cit. on p. 18).
- [38] Michael C. Breadmore. «Electrokinetic and Hydrodynamic Injection: Making The Right Choice for Capillary Electrophoresis». In: *Bioanalysis* 1.5 (2009), pp. 889–894 (cit. on p. 19).
- [39] Shih-Yuan Teh, Rong Lin, Lung-Hsin Hung, and Abraham P. Lee. «Droplet microfluidics». In: *Lab on a Chip* 8 (2008), pp. 198–220 (cit. on p. 19).
- [40] Amir Abbas Kojabad, Mohammad Farzanehpour, Hossein E G Galeh, Reza Dorostkar, Abbas Jafarpour, Mohammad Bolandian, and Mohammad Mehdi Nodooshan. «Droplet digital PCR of viral DNA/RNA, current progress, challenges, and future perspectives». In: *Journal of Medical Virology* 93.7 (2021), pp. 4182–4197 (cit. on p. 19).
- [41] Wei Zhou et al. «Microfluidics applications for high-throughput single cell sequencing». In: *Journal of Nanobiotechnology* 19 (2021), pp. 1–21 (cit. on p. 19).
- [42] Shanshan Guo, Chun Zhang, and Anh Le. «The limitless applications of single-cell metabolomics». In: *Current Opinion in Biotechnology* 71 (2021), pp. 115–122 (cit. on p. 19).
- [43] Shikai Lin et al. «Microfluidic single-cell transcriptomics: moving towards multimodal and spatiotemporal omics». In: *Lab on a Chip* 21 (2021), pp. 3829–3849 (cit. on p. 19).
- [44] Francesca Puppo, Akshat Dave, Marie-Agnes Doucey, Davide Sacchetto, Camilla Baj-Rossi, Yusuf Leblebici, Giovanni De Micheli, and Sandro Carrara. «Memristive Biosensors Under Varying Humidity Conditions». In: *IEEE Transactions on NanoBioscience* 13.1 (Mar. 2014), pp. 19–30 (cit. on p. 19).

- [45] Francesca Frascella. *Photolithography*. Slides PDF. FMTA, Politecnico di Torino. 2022 (cit. on p. 24).
- [46] D.R. Hines, N.P. Siwak, L.A. Mosher, and R. Ghodssi. «MEMS Lithography and Micromachining Techniques». In: *MEMS Materials and Processes Handbook*. Ed. by Reza Ghodssi and Pinyen Lin. Vol. 1. MEMS Reference Shelf. Springer, Boston, MA, 2011, pp. 217–265 (cit. on p. 25).
- [47] Chegg. *Identify three methods for mask alignment and exposure shown. Describe their resolutions, pros, and cons*. <https://www.chegg.com/homework-help/questions-and-answers/7-identify-three-methods-mask-alignment-exposure-shown-describe-resolutions-pros-cons-add-q61153744>. Accessed: 2024-10-15 (cit. on p. 27).
- [48] Neil Convery and Nikolaj Gadegaard. «30 Years of Microfluidics». In: *Micro and Nano Engineering 2* (2019), pp. 76–91 (cit. on pp. 27, 57, 60, 61).
- [49] Ioulia Tzouvadaki, Alessandro Vallero, Francesca Puppo, Giovanni De Micheli, and Sandro Carrara. «Resistance Impact by Long Connections on Electrical Behavior of Integrated Memristive Biosensors». In: *2016 IEEE International Symposium on Circuits and Systems (ISCAS)*. Montréal, QC, Canada: IEEE, 2016, pp. 385–388 (cit. on pp. 38, 42).
- [50] Center of MicroNanoTechnology (CMi). *Mask Fabrication*. <https://www.epfl.ch/research/facilities/cmi/process/photolithography/mask-fabrication/>. Accessed: 2024-10-15 (cit. on p. 44).
- [51] Center of MicroNanoTechnology (CMi). *AZ NLOF 2020*. <https://www.epfl.ch/research/facilities/cmi/process/photolithography/photoresist-selection/az-nlof-2020/>. Accessed: 2024-10-15 (cit. on p. 45).
- [52] Sumaira Nishat, Ali Turab Jafry, Andres W. Martinez, and Fazli Rabbi Awan. «Paper-based microfluidics: Simplified fabrication and assay methods». In: *Sensors and Actuators B: Chemical* 336 (2021), p. 129681 (cit. on p. 57).
- [53] Vito Saggiomo and Aldrik H. Velders. «Simple 3D Printed Scaffold-Removal Method for the Fabrication of Intricate Microfluidic Devices». In: *Advanced Science* 2.9 (2015), p. 1500125 (cit. on p. 57).
- [54] Frederic Ceysens and Robert Puers. «SU-8 Photoresist». In: *Encyclopedia of Nanotechnology*. Ed. by Bharat Bhushan. Springer, Dordrecht, 2016 (cit. on p. 58).
- [55] Seok Chung and Seungbin Park. «Effects of temperature on mechanical properties of SU-8 photoresist material». In: *Journal of Mechanical Science and Technology* 27.9 (2013), pp. 2701–2707 (cit. on p. 58).

- [56] Elveflow. *The Poly-Di-Methyl-Siloxane (PDMS) and Microfluidics*. <https://www.elveflow.com/microfluidic-reviews/general-microfluidics/the-poly-di-methyl-siloxane-pdms-and-microfluidics>. Accessed: 2024-10-13 (cit. on pp. 59, 60).
- [57] Alessandro Vallero, Ioulia Tzouvadaki, Francesca Puppo, Marie-Agnes Doucey, Jean-Francois Delaloye, Giovanni De Micheli, and Sandro Carrara. «Memristive biosensors integration with microfluidic platform». In: *IEEE Transactions on Circuits and Systems I: Regular Papers* 63.12 (Dec. 2016), pp. 2120–2127 (cit. on pp. 65, 84, 85).
- [58] Matteo Agostini, Gina Greco, and Marco Cecchini. «Polydimethylsiloxane (PDMS) Irreversible Bonding to Untreated Plastics and Metals for Microfluidics Applications». In: *APL Materials* (2024) (cit. on p. 75).
- [59] PIE Scientific. *Photoresist Ashing or Stripping Using Oxygen Plasma*. [https://piescientific.com/resource\\_pages/resource\\_photoresist\\_ashing/](https://piescientific.com/resource_pages/resource_photoresist_ashing/). Accessed: 2024-10-15 (cit. on p. 75).
- [60] Alenka Vesel and Miran Mozetič. «Surface modification and ageing of PMMA polymer by oxygen plasma treatment». In: *Vacuum* 86.6 (2012), pp. 634–637 (cit. on p. 76).
- [61] R. Morent, N. De Geyter, C. Leys, L. Gengembre, and E. Payen. «Study of the ageing behaviour of polymer films treated with a dielectric barrier discharge in air, helium and argon at medium pressure». In: *Surface and Coatings Technology* 201.18 (2007), pp. 7847–7854 (cit. on p. 76).
- [62] Adrian Mata, Alan J. Fleischman, and Shuvo Roy. «Characterization of Polydimethylsiloxane (PDMS) Properties for Biomedical Micro/Nanosystems». In: *Biomedical Microdevices* 7 (2005), pp. 281–293 (cit. on p. 76).
- [63] Samuel K. Sia and George M. Whitesides. «Microfluidic devices fabricated in poly(dimethylsiloxane) for biological studies». In: *Electrophoresis* 24.21 (2003), pp. 3563–3576 (cit. on p. 76).
- [64] Alexandra Borók, Kristóf Laboda, and Attila Bonyár. «PDMS Bonding Technologies for Microfluidic Applications: A Review». In: *Biosensors* 11.8 (2021), p. 292 (cit. on pp. 76, 77).
- [65] Carlos Luis Gonzalez-Gallardo. «Improving Plasma Bonding of PDMS to Gold-Patterned Glass for Electrochemical Microfluidic Applications». In: *Microfluidics and Nanofluidics* (2021) (cit. on pp. 77, 78).
- [66] Anthony K. Au, Hoyin Lai, Ben R. Utela, and Albert Folch. «Microvalves and Micropumps for BioMEMS». In: *Micromachines* 2.2 (May 2011), pp. 179–220. DOI: 10.3390/mi2020179. URL: <https://doi.org/10.3390/mi2020179> (cit. on p. 98).

- [67] Ioulia Tzouvadaki, Abuduwaili Tuoheti, Severine Lorrain, Manfredo Quadroni, Marie-Agnes Doucey, Giovanni De Micheli, Danilo Demarchi, and Sandro Carrara. «Multi-Panel, On-Single-Chip Memristive Biosensing». In: *IEEE Sensors Journal* 19.14 (July 2019), pp. 5769–5774 (cit. on p. 98).